The Pennsylvania State University

The Graduate School

MECHANICAL BEHAVIOR OF SAND SUBJECTED TO IMPACT LOADING

A Dissertation in

Civil Engineering

by

Sudheer Sudhakaran Prabhu

Submitted in Partial Fulfillment
of the Requirements
for the Degree of

Doctor of Philosophy

August 2021

The dissertation of Sudheer Sudhakaran Prabhu was reviewed and approved* by the following:

Tong Qiu
Associate Professor of Civil and Environmental Engineering
Dissertation Advisor
Chair of Committee

Ming Xiao
Associate Professor of Civil and Environmental Engineering

Shimin Liu
Associate Professor of Energy and Mineral Engineering

Todd Palmer
Professor of Engineering Science and Mechanics

Patrick J. Fox
Professor of Civil and Environmental Engineering
Head of the Department of Civil and Environmental Engineering

ABSTRACT

Sand is generally subjected to quasi-static loading in the field. However, for applications involving projectile impacts and surface or mine blasts, sand is subjected to high strain-rate loading. To predict the response of underground structures under these loading conditions, there is a need to accurately understand the high strain-rate response of sand overlaying these structures. Researchers noted that the split Hopkinson pressure bar (SHPB) tests provide reliable data on the high strain-rate response of sand and have been extensively used. SHPB studies on sand showed that the stress-strain response of sand is dependent on the water content of the specimen and the particle breakage of sand grains.

Several numerical models have been developed through the years to capture the high strain-rate sand response accurately. However, these models were developed mainly for dry sands, completely saturated sands, and sand with high water contents. These numerical models are unable to capture the softening and subsequent stiffening stress-strain behavior observed in sands at low water contents and low stresses. In this study, SHPB tests of sands are numerically simulated and the equations of state (EOS) at different water contents are calibrated using back calculation. The back-calculated EOSs are used to calibrate a three-phase model capable of capturing the sand response at varying water contents. The response predicted by the three-phase model is validated by comparing the numerical and experimental stress-strain responses. A parametric study was carried out to understand the effect of interface friction and aspect ratio on the validity of the SHPB results by considering different aspect ratios and interface frictions for the specimens. The results

showed that specimens with higher aspect ratio take longer time to achieve stress equilibrium while specimens with interface friction never attain perfect stress equilibrium.

Another important factor that affects the high strain-rate stress-strain response of sand is the particle breakage of sand grains. Due to the difficulty of continuum-scale models in capturing particle breakage in sands, discrete element method (DEM) is used to model high strain-rate loading of sand specimens. The study tries to understand the effectiveness of particle upscaling-downscaling procedure adopted in DEM in modeling high strain-rate problems. In this study, several SHPB tests reported in literature are modeled in DEM with particle breakage introduced in these simulations. The results showed that with well-calibrated parameters for contact behavior and particle crushing, specimens with upscaled particle size distribution (PSD) provide similar dynamic stress-strain response and PSD evolution as those reported in literature. This study shows the importance of particle breakage in the stress-strain response under high stresses as the specimens without particle breakage yield a much stiffer response compared to the specimens with particle breakage. The developed DEM model will be a useful tool to model the complete SHPB test setup as the incident, reflected and transmitted stress waves can be accurately replicated.

TABLE OF CONTENTS

LIST OF FIGURES

LIST OF TABLES

ACKNOWLEDGEMENT

I would like to express my sincere gratitude to my advisor, Dr. Tong Qiu, who has been a tremendous mentor for me during my graduate studies at Penn State. I would like to thank Dr. Qiu for his enormous support, guidance, patience and exposure provided without which, my research would have been impossible. The hours spent during our meetings have significantly helped me improve my technical abilities and critical thinking and helped me develop as a researcher. I would also like to thank Dr. Ming Xiao for reviewing the manuscript and providing valuable suggestions. Moreover, I would like to thank Dr. Xiao for mentoring and guiding the research team during the PennDOT project, inspite of the subfreezing temperatures in the field. I would also like to offer my genuine appreciation to my committee members, Dr. Shimin Liu and Dr. Todd Palmer for reviewing the manuscript and providing valuable perspective on my work. I would like to thank Dr. Bo Song of Purdue University for providing the data from his laboratory tests.

I would also like to thank Mission Critical Solutions, LLC, Ben Franklin Technology Partners, The Pennsylvania Department of Transporation, the Center for Integrated Asset Management for Multi-modal Transportation Infrastructure Systems (CIAMTIS): Region 3 University Transportation Center and the Deparmtent of Civil and Environmental Engineering at Penn State for providing partial financial support to my study.

This dissertation would never have been completed without the support and devotion of my family and friends. I am ever grateful to my mother, who always inspired and supported me to follow my dreams, and my father, who was my best friend and would have

been the happiest person to see me graduate. I am forever grateful to my office mate, Jintai Wang, who continues to mentor me even after his graduation and always has been an infinite source of inspiration and encouragement. I am forever thankful to Dr. Cibin Raj, Dr. Femeena P.V and Dr. Lekshmi Suku for guiding me with their life experiences during my graduate studies. I would also like to thank the NFL, NBA, CFB, and EPL broadcasts for being there on the weekends and late nights while I was working on the simulations. I would also like to thank Dan Fura for extensively helping me with the laboratory and field testing. I would also like to thank my collegues Amir Ahmedipur, Kun Zeng, Min Liu, Bahman Sheik, Yanan Li and Pei Te for their friendship. Finally, I would like to thank my fiancé, Ms. Divyasree Pai, for her patience, smile, and support during the final stages of my graduate studies. Her love, care and affection provided confidence to believe in myself during the difficult years of this work.

Sudheer
01/2021

CHAPTER 1

INTRODUCTION

1.1 Motivation

Sand in the field is subjected to a wide range of strain rates based on the application and these strain rate regimes are depicted in Fig. 1.1. For all general construction purposes, sand is subjected to low or quasi-static strain rates. Basic mechanical characteristics of sand, including strength and stiffness, are obtained from conventional tests like triaxial tests, direct shear tests and oedometer tests performed under quasi-static conditions. However, Omidvar et al. (2012) noted that sand provides a stiffer response to high strain-rate loading compared to quasi-static loading and conventional tests in the laboratory are unable to capture the high strain-rate sand response. Different methodologies are used to study sand behavior at high strain rates. Some of these tests include the split Hopkinson pressure bar (SHPB) test, flyer plate test, high strain rate oedometer tests etc.

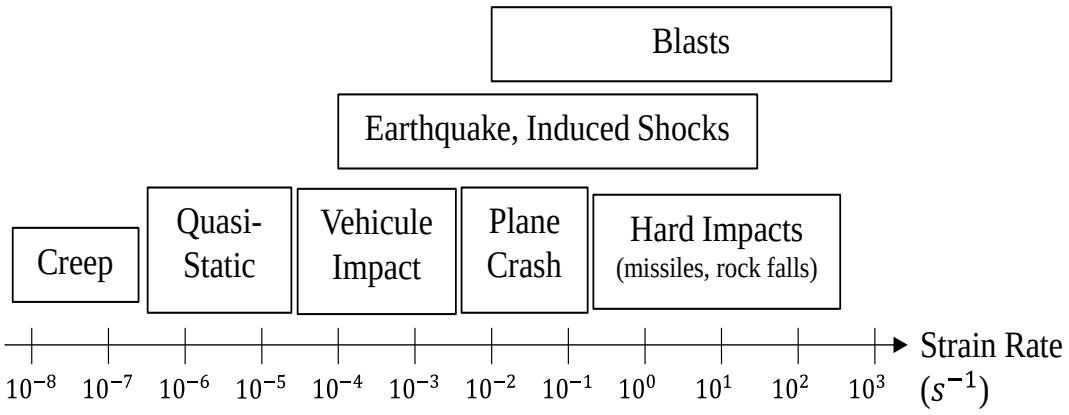

Fig. 1.1. Range of strain rates experienced by soil in the field

During impact loading and most other high strain-rate loadings, sand is subjected to strain rates in the range of 100-5000/s. Studies have shown that for the strain rates in this range, SHPB tests are generally reliable and provide accurate stress-strain responses of sand (Nemat-Nassar 2000). The SHPB test was recently introduced in the field of geomechanics to understand the stress-strain response of sand and since, has been extensively used to study sand behavior at high strain rates. In one of the initial studies, Felice (1985) carried out SHPB tests to study the effect of water content and dry density on the stress-strain response of sand. Subsequently, several researchers have carried out SHPB tests on sand to understand different aspects including the effect of dry density, stress equilibrium in the sand specimen, effect of strain rate etc. on the stress-strain response of sands (Ross et al. 1986; Felice et al. 1987; Charlie et al. 1990; Semblat et al. 1999; Song et al. 2009; Luo et al. 2011; Huang et al. 2013; Wang et al. 2017).

Recent studies on sand using the SHPB tests showed that its stress-strain response, at high strain rates, is a function of water content (Song et al. 2009; Luo et al. 2014; Wang et al. 2017). An increase in water content of the sand from the dry condition first leads to a

softer stress-strain response, especially at low stresses. The softening of stress-strain response is observed only till a transition water content, beyond which the stress-strain response stiffens with a further increase in water content. There are several constitutive models developed by researchers to accurately capture the field response of sand subjected to high strain rates. However, none of these models were able to capture the softening-stiffening behavior observed in sands at low water contents and under low stresses. Therefore, for accurately capturing the field response, there is a need to develop a constitutive model capable of capturing the softening-stiffening behavior of sand at low stresses, utilizing the SHPB test data reported in literature.

Another important parameter defining the high strain-rate sand behavior, especially at high stresses, is the particle breakage. The evolution of particle size distribution (PSD) during quasi-static experiments has been extensively studied and well documented by researchers, highlighting the importance of particle breakage in quasi-static stress-strain response of sand (Minh and Cheng 2013; Yu 2017). However, the short loading duration in the high strain-rate SHPB experiments makes it difficult to capture the evolution of particle size distribution in these experiments. The discrete element method (DEM) is an effective tool and has been used extensively to understand particle breakage in sand under quasi-static loading (Lobo-Guerrero and Vallejo 2005; deBono and McDowell. 2013; Hanley et al. 2015). However, due to the complexity of the problem and computational cost, only limited attempts have been made to capture particle breakage in high strain-rate problems using DEM. One of the effective methodologies to reduce the computational cost in DEM is using an upscaling procedure. During upscaling, the PSD is shifted to the right thus effectively increasing the particle sizes and hence reducing the number of particles in

the simulation. The methodology has been extensively used for modeling sand in quasi-static experiments (Ciantia et al. 2015, 2019; Roessler and Katterfeld 2018). However, its effectiveness in high strain-rate problems has not been attempted and therefore, is not well understood.

This study is motivated by two reasons: the lack of constitutive models available to capture the high strain-rate sand behavior as a function of water content, especially at low stresses and the lack of numerical models capable of accurately capturing the particle breakage in sands at high strain rates. A more detailed review of the SHPB tests and numerical methodologies is presented in the subsequent sections.

1.2 Split Hopkinson Pressure Bar

The SHPB test was first developed by Kolsky (1949) and has been extensively used to study the high strain-rate response of different materials including metals, alloys etc. An SHPB test setup consists of an incident bar (IB), a transmission bar (TB) and a striker bar. The IB and TB metal bars should be homogeneous, isotropic and linearly elastic. The specimen is located between the IB and TB. The striker bar is made to impact the incident bar at a high velocity, generating a compressive stress wave in the IB. The magnitude and time duration of the incident stress depend on the velocity and length of the striker bar. The magnitude of stress generated should be well within the elastic limit of the material used for the IB and TB. For specimens with low unconfined compressive strengths (e.g., rubber, sand), a confining tube is used to confine the specimen. For obtaining a one-dimensional wave propagation in the specimen, generally, a steel tube is used for confinement. In most

of the studies, lubrication is applied at the specimen-confining tube interface, IB-specimen interface and TB-specimen interface to reduce the effect of friction on the stress-strain response. Fig. 1.2 shows the schematic diagram of the SHPB test setup along with the strain gauges attached.

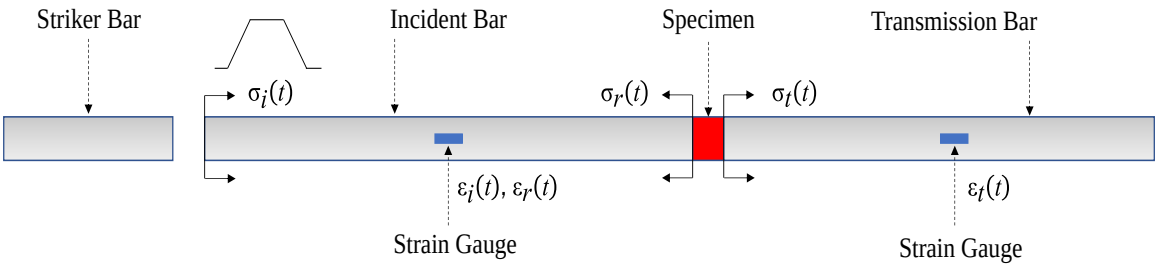

Fig. 1.2. Schematic diagram of the SHPB test setup

During an SHPB test, the incident stress generated by the striker bar travels through the IB and reaches the IB-specimen interface, where a portion of the incident stress is transmitted into the specimen while a portion is transmitted back into the IB. The stress wave transmitted into the specimen travels through the specimen and reaches the TB-specimen interface where a portion of the stress wave is transmitted into the TB and a portion is reflected into the specimen. Strain gauges are attached on the IB and TB to measure the incident strain ($\varepsilon_i(t)$), reflected strain ($\varepsilon_r(t)$) and transmitted strain ($\varepsilon_t(t)$) as functions of time t. Assuming the specimen to deform under stress-equilibrium condition, standard SHPB equations can be used to derive the stress-strain response of the specimen (Gama 2004; Gama et al. 2004) as

$$\varepsilon\,(t) = -2\frac{c_o}{L_s}\int_0^t \varepsilon_r(t)\;dt \tag{1.1}$$

$$\sigma_t\,(t) = \frac{A_o}{A_s}E_o\;\varepsilon_t(t) = E_o\;\varepsilon_t(t) \tag{1.2}$$

$$\dot{\varepsilon}\,(t) = -2\frac{c_o\;\varepsilon_r(t)}{L_s} \tag{1.3}$$

where $\varepsilon\,(t)$ is the strain in the specimen, $\sigma_t\,(t)$ is the stress in the specimen, $\dot{\varepsilon}\,(t)$ is the strain rate experienced by the specimen, c_o is the wave velocity in the bars, and L_s is the length of the specimen.

1.3 Effect of Water Content on the High Strain-Rate Sand Response

One of the earliest attempts to study the effect of water content on the stress-strain response of sand at high strain rates using SHPB was carried out by Felice et al. (1985). The study showed that for completely saturated sands and sands with high water contents, the incompressibility of water dominated the high strain-rate stress-strain response. However, SHPB tests by Song et al. (2009) showed that for sands at low stresses (<10MPa), the stress-strain response varies as a function of water content. The addition of water to dry sand softens the stress-strain response at high strain rates. Omidvar et al. (2012) attributed this softening to the reduction in friction between sand particles due to the lubrication from water. The softening is observed till a transition water content, beyond which an increase in water content stiffens the stress-strain response due to the incompressibility of water. Fig. 1.3 shows a schematic representation of the softening-stiffening behavior of sand at varied water contents. The SHPB tests by Luo et al. (2014)

and Wang et al. (2017) also noted similar softening-stiffening behavior in the stress-strain responses at low water content and stresses.

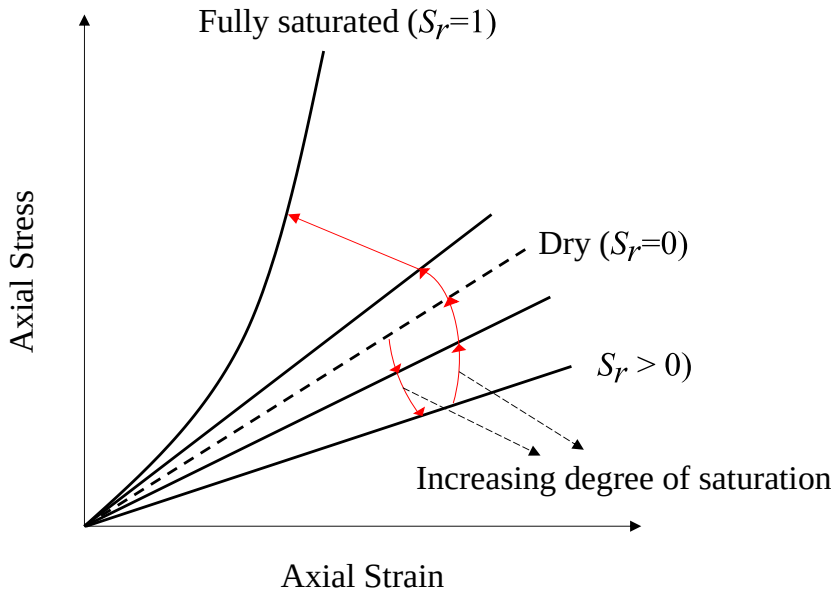

Fig. 1.3. Softening – stiffening behavior of sand under high strain rates and varied water contents

1.4 Constitutive Models for High Strain-Rate Sand Response

Explosions and surface blasting can often cause damage to the underground structures. As it is difficult to carry out large scale experiments involving blast loadings, projectile impact and other impact loadings in the field, researchers generally rely on numerical simulations to understand the effect of these loadings on the underground structures. The finite element method (FEM) has been effectively used to model field simulations involving high strain-rate loadings. Researchers have noted that the accuracy of FEM

simulations is dependent on the constitutive models used and the calibrated model parameters. For problems involving geomaterials loaded at quasi-static strain rates, simple constitutive models (e.g., Mohr-Coulomb, Drucker-Prager, and Hardening soil) can accurately capture the soil behavior (Yang and Yu 2006; Huang et al. 2009; Suku et al. 2016). However, studies showed that high strain-rate field problems involving explosions and projectile impacts could not be captured by these models and there is a need for more advanced models (Busch and Tarefder 2017; Busch et al. 2017).

Researchers noted that the high strain-rate sand response is governed by the pressure-volume relationship of sand, which is popularly known as the equation of state (EOS). The accuracy of the simulation results is dependent on the accuracy of the EOS calculated. In one of the initial approaches, the EOS model proposed by Tillotson (1962) was used by researchers to model crater formation in sand (Bjorkman and Holsapple 1983). Another commonly used model is the Mie-Gruneison EOS which was developed for solids assuming that the pressure is a linear function of energy. Wang et al. (2004a, 2004b) developed a three-phase model based on the Kandaurs model, assuming soil to be constituting of building blocks with water and air in between these solids. The load applied on the soil is divided into two parts, one for compressing the different soil phases and the others to move the solid. However, none of these models were suitable to capture the softening-stiffening behavior in sand as a function of water content at low stresses. Most models in literature are calibrated for sands with very large water contents, where the incompressibility of water dominated the sand response. Therefore, there is a need to calibrate and validate a model capable of capturing the softening-stiffening behavior in sand with water content, especially at low stresses.

1.5 Stress Equilibrium in SHPB Tests

Initially, when the incident stress wave reaches the IB-specimen interface in a SHPB test, there is a stress gradient between the IB-specimen and TB-specimen interfaces. With time, the stress gradient gradually reduces as the stress wave reverberates in the specimen. When the stress gradient ultimately reaches zero, the specimen is said to deform under stress equilibrium condition, i.e., the stresses at the IB-specimen and TB-specimen interfaces are equal. The classic SHPB equations (Eqs. 1.1-1.3) assumes stress-equilibrium condition.

For a specimen to attain stress equilibrium, the stress wave should reverberate 3-4 times in the specimen (Davis and Hunter 1963; Ravichandran and Subhash 1993, Chen et al. 1999). For specimens with large impedance (e.g., metals and alloys), the stress equilibrium condition is achieved at a faster rate compared to low-impedance specimens (sands, rubber etc.). Considering the achievement of stress equilibrium in soft specimens, Gray (2000) showed that the optimum specimen aspect ratio (L_s/D) for the specimen is in the range of 0.25-0.5. Most SHPB studies on sand specimens used a two-wave approach to determine the stress equilibrium in the specimen (Song et al. 2009; Wang et al. 2017). In the two - wave approach, the incident, reflected and transmitted stresses are compared and the specimen deforms in stress equilibrium if the condition shown in Eq. 1.4 is achieved.

$$\sigma_i + \sigma_r = \sigma_t \tag{1.4}$$

where σ_i, σ_r and σ_t are the incident, reflected and transmitted stresses, respectively. However, Song and Chen (2004) showed that this methodology cannot be used for soft

specimens and therefore, an ideal methodology is to compare the forces at the IB-specimen and the TB-specimen interfaces.

Gray (2000) noted that a shaped incident pulse, i.e., a pulse with larger ramp up time compared to a rectangular pulse, needs to be used for soft specimens. A shaped pulse helps the soft specimen attain stress equilibrium before significant strains occur in the specimen. The SHPB tests reported on sand specimens in the literature showed that with shaped incident pulses, the stress equilibrium is attained only under high stresses (>10-20 MPa) (Luo et al. 2014; Wang et al. 2017). Therefore, the stress-strain response beyond this stress is deemed valid. However, soft specimens do not attain stress equilibrium under low stresses, seriously questioning the validity of the stress-strain response of sand specimens under low stresses. Therefore, there is a need to study the validity of stress-strain responses of sands from SHPB tests in the literature, especially at low stresses.

1.6 Particle Breakage in Sand during Impact Loading

Particle breakage has been observed to play an important role in sand behavior, especially, at high stresses (>10MPa). Xiao et al. (2019) noted that the energy required to achieve same particle breakage extent is lower under quasi static loading compared to dynamic loading. Xiao et al. (2019) also noted that the breakage energy in sand is minimal (< 5% of total energy) compared to the energy dissipation from the particle redistribution (>60% of total energy). However, the particle breakage in sand can signigicantly affect the stress-strain response of sand. The importance of particle breakage on the stress-strain response of sand, at quasi-static strain rates, has been well documented in the literature.

One-dimensional compression test on sand by Nakata et al. (2001) and McDowell (2002) reported that sand starts to yield at stresses higher than 10 MPa. The yielding of sand is attributed to the initiation of particle breakage. McDowell (2002) reported the PSD evolution during the one-dimensional compression test and noted that the yield point of a sand specimen is a function of sand particle size.

SHPB studies have reported considerable particle breakage during the tests; however, the evolution of PSD during the tests has rarely been reported. The only studies that reported the experimental PSD evolution in an SHPB test were Huang et al. (2013, 2014) where the specimens were X-rayed during the experiments. Huang et al. (2014) noted that for the same sand sample considered, the PSD evolution is dependent on the strain rate applied. The difficulty in obtaining the PSD evolution from the experiments and lack of numerical models capable of capturing particle breakage in high strain rate make it necessary to develop, calibrate and validate a numerical model capable of capturing high strain-rate sand response, incorporating particle breakage.

1.7 DEM Modeling of Sand to Study Micromechanical Behavior

Continuum constitutive models have been extensively used by researchers to capture the high strain-rate response of sand; however, these models do not explicitly take the particle breakage into account. DEM is an effective tool capable of capturing the micromechanical behavior of sand. DEM was first introduced by Cundall and Strack (1979) and works on the principle of Newton's second law of motion. Individual sand grains are modeled typically as spheres and the interaction between grains is captured using

different contact constitutive laws defining the force transferred between the spheres. DEM works on the principal of explicit time integration where the kinematics of a sphere, including its position, velocity, acceleration etc., at any given time step is obtained from their corresponding values from the previous time step.

DEM has been extensively used to model different tests in the field of geomechanics and geotechnical engineering. Studies noted that DEM could replicate the actual sand behavior reported in the laboratory tests (Salot et al. 2009; Kozicki et al. 2014). Researchers noted that with well calibrated parameters, DEM can replicate the particle breakage in one dimensional compression tests and triaxial tests (deBono and McDowell 2014; Hanley et al. 2015). However, one of the disadvantages of DEM is that the method works on the principal of contact tracing, i.e., after each time step, the contacts on each individual particle need to be detected, updated and stored, making the simulations computationally expensive.

An effective methodology adopted to minimize the computational cost in DEM is by adopting an upscaling procedure. During upscaling, the PSD is shifted to the right, i.e., particle size of sand in the DEM simulation is increased, effectively reducing the number of particles in the simulation. Using upscaled particles, Roessler and Katterfeld (2018) simulated the angle of repose tests on sand and Katzenbach and Schmitt (2004) studied the efficiency of pile drilling machinery. Bono and McDowell (2014) used uniform particles to replace sand in a triaxial test to understand the effect of particle crushing in sand and Kermani et al. (2015) used uniform particles with size D_{50} to represent sand in a flow test. The above studies showed that with appropriately calibrated parameters of DEM particles, the specimens with upscaled PSD can accurately replicate the sand behavior shown in the

experiments. However, the effectiveness of particle upscaling has only been discussed for sands tested in quasi-static strain rates and no attempts have been reported in the literature to understand its effectiveness on high strain-rate problems.

1.8 Modeling Particle Breakage

Particle breakage is typically modeled in DEM using two methodologies. In the first methodology, individual sand grains are replaced by agglomerates as shown in Fig. 1.4. Agglomerates constitute of smaller spheres bonded together with each agglomerate representing a sand grain. Typically, an agglomerate consists of 57-212 spheres with the spheres connected to each other using bonds. Strengths of these individual bonds are calibrated such that the agglomerate can accurately replicate the single grain crushing strength of sand particles. Researchers (Kwok and Bolton 2013; Huang et al. 2013) used this methodology to simulate one-dimensional oedometer tests and triaxial tests. The bonds are free to break if the force on the bond exceeds the bond strength, representing particle breakage. The methodology accurately replicates the stress-strain response and the PSD evolution during experiments. However, this methodology can only be implemented in sand specimens with small dimensions and few grains, and is impractical for large specimens due to the exponential increase in computational cost.

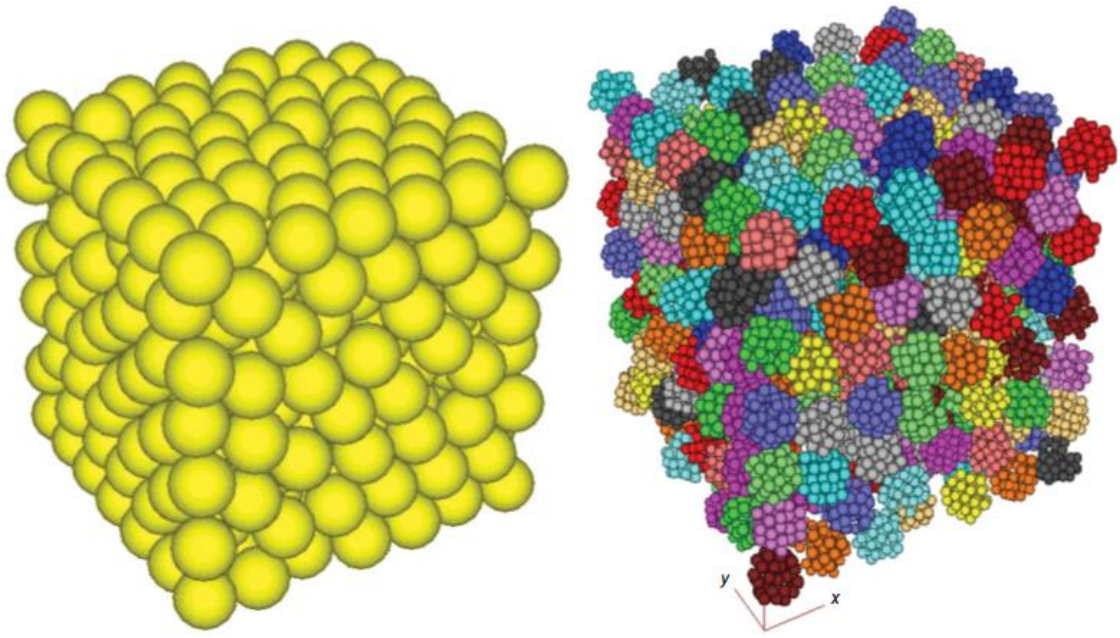

Fig. 1.4. Sand specimen in DEM: (a) individual particles modelled as spheres; (b) sand grains replaced by agglomerates (Kwok and Bolton 2013)

In another methodology, individual sand particles are modeled as spheres. During loading, a force/stress criterion is checked to determine particle breakage in the specimen. If the force/stress acting on any particle exceeds its strength, the parent particle is replaced by smaller spheres known as daughter particles. Two different systems are used to replace the parent particle with daughter particles. In the first system, daughter particles are placed with significant overlap while in the second system, daughter particles are introduced without any overlap. The first system leads to conservation of mass in the system; however, during each particle breakage, the system generates large unbalanced forces due to the overlap of daughter particles, and needs to be equilibrated after each particle breakage

sequence (Fig. 1.5). For modeling particle breakage in SHPB tests, the simulation needs to be continuous and cannot pause to be equilibrated to dissipate forces.

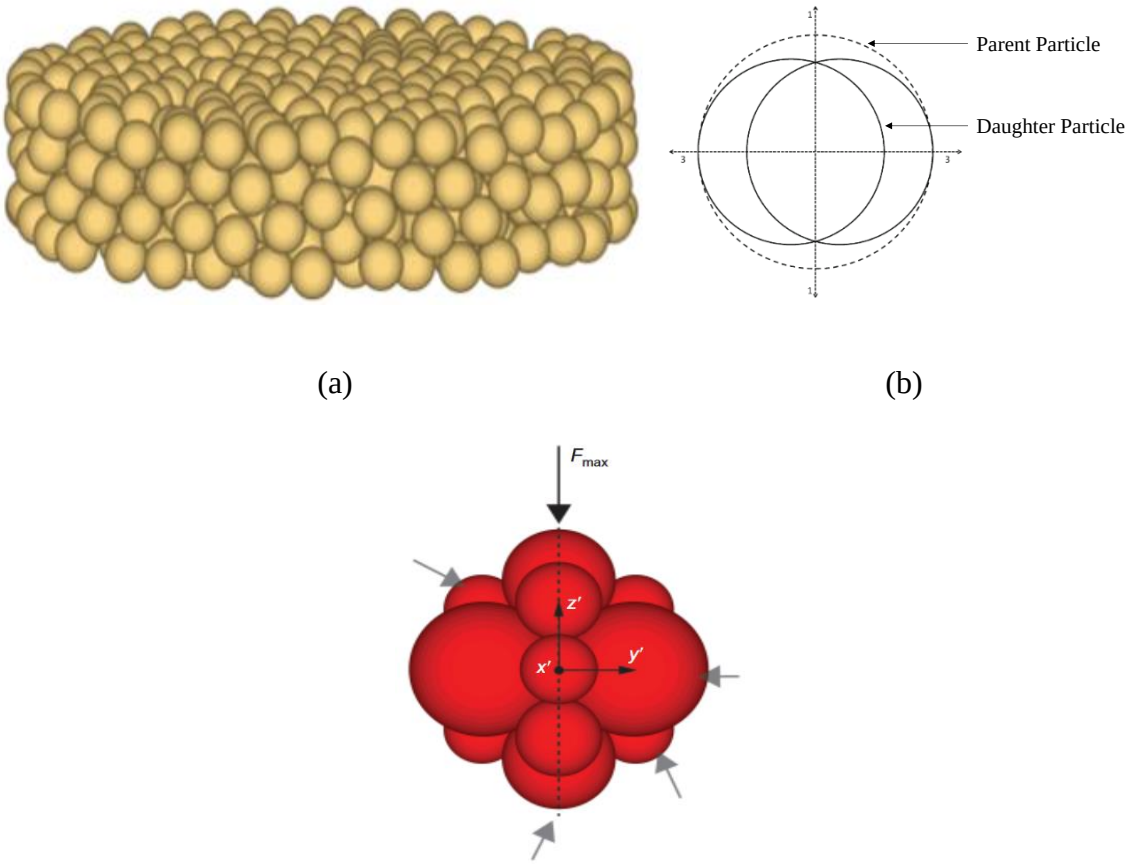

(a) (b)

(c)

Fig. 1.5. One- dimensional compression test in DEM (a) one-dimensional oedometer test specimen (deBono and McDowell 2013); (b) daughter particle configuration with overlapping (deBono and McDowell 2013); (c) daughter particle configuration without overlap (Ciantia et al. 2015)

Several studies have used the second system with non-overlapping daughter particles to incorporated particle breakage in DEM despite the mass is not conserved in particle breakage. Guerrero and Vallejo (2005) used a force criterion in their 2D simulations of direct shear test and pile driving and replaced the broken parent particles with a set of 8 non-overlapping daughter particles. Ciantia et al. (2015, 2019) modeled one-dimensional compression test (Fig. 1.5) in DEM and introduced particle breakage using the force criterion. Each parent particle satisfying the force criterion was replaced in the simulation by 14 non-overlapping daughter particles (Fig. 1.5c), retaining 53% of mass of the parent particle. With the aforementioned methodology, Ciantia et al. (2015; 2019) showed that the stress-strain response of sand in one-dimensional compression tests could be accurately replicated. The study also showed that increasing the number of daughter particles beyond 14 did not significantly affect the mechanical behavior of sand. Ciantia et al. (2015) noted that the mass lost during each particle breakage did not significantly contribute in the force transfer mechanisms and therefore can be safely ignored in the simulation. However, the model by Ciantia et al. (2015) used large comminution limits (i.e., the smallest particle that can be broken) to match the simulated stress-strain response with the laboratory test results. Guerrero and Vallejo (2005a, 2005b) noted that strength of the particle increases with an increase in confinement. Therefore, models calibrated using single grain crusing tests might not be able to replicate the actual sand behavior. Under large stresses, the surrounding smaller particles provide significant confinement to the larger particles thus significantly reducing the probability of breakage of large sand particles. However, the model by Ciantia et al. (2015, 2019) did not take into account the effect of particle confinement on the particle strength in the simulation. All of these models were calibrated

for problems where sand is loaded under quasi-static loading and there are no particle breakage models available in literature that aredeveloped for high strain-rate loading.

1.9 Dissertation Scope and Objective

The objectives of this research are todevelop a continuum-scale model capable of capturing the EOS and stress-strain response of sand at high strain rates and varying water contents using the FEM, and develop a discrete-scale model to capture particle breakage in sand at high strain rates using the DEM. To achieve these objectives, FEM and DEM models have been developed, calibrated, and validated to model well-documented SHPB tests reported in literature. The motivation of conducting this study and a brief review of current literature were presented in Chapter 1.

Chapter 2 presents the simulations of SHPB tests in finite element code LS-DYNA. Using the simulations, a three-phase model for sand is calibrated to capture the EOS of sand at any given water content. The calibrated three-phase model is capable of predicting the EOS of sand and capturing the softening-stiffening behavior of sand as the water content changes. This chapter is based on a paper published in the *Journal of Engineering Mechanics*, ASCE, 2020.

Chapter 3 presents the simulation of SHPB tests using a combined FEM-DEM approach where the IB, TB, and confining tube in SHPB test setup are modeled using FEM and the sand is modeled using DEM. Using these simulations, the effectiveness of particle upscaling in high strain-rate problems is discussed. This chapter is based on a paper

published in the Eighth International Conference on Case Histories in Geotechnical Engineering, ASCE, 2019.

Chapter 4 presents the simulations of SHPB tests in DEM using Particle Flow Code 3D. In a novel methodology, the IB, TB, and confining tube in SHPB test setup are modeled using DEM. The chapter mainly discusses the effect of stress inequilibrium on the stress-strain response of sand in SHPB tests. For simplicity, only low stresses are considered and, hence, sand particle breakage is not modeled. This chapter is based on a manuscript that is currently under review in the *International Journal of Geomechanics*, ASCE.

Chapter 5 presents the DEM simulations of SHPB tests on sand taking the particle breakage into consideration. Initially, the effectiveness of particle upscaling-downscaling procedure is discussed and the model parameters for the particle breakage is calibrated. Using the calibrated model, several SHPB tests are modeled and the simulated results are compared with the reported experimental results. The chapter discusses the ability of the DEM simulations to replicate the SHPB experiments, including the incident, reflected and transmitted stress waves. The chapter also discusses the effect of particle breakage on the high strain-rate sand response and compares the simulated PSD evolution with the reported experimental PSD evolution.

Chapter 6 smmarizes major conclusions from the present study along with recommendations for future work.

References

Bjorkman, M. D., and Holsapple, K. A. (1983). “Plane hypervelocity impact and source similitude dependence on a Tillotson E.O.S.”. *Proceedings of the 3rd APS Topical Conference on Shock Waves in Condensed Media*, North-Holland, Amstedam.

Busch, C. L., and Tarefder. R. A. (2017). “Evaluation of appropriate material models in LS-DYNA for MM-ALE finite element simulations of small-scale explosive air blast tests on clay soils.” *Indian Geotechnical Journal*. 47(2):173–186.

Busch, C. L., Tarefder, R. A., and Aimone-Martin. C. T. (2017). “Deformation induced stability of earthen embankment dams subjected to explosive airblast loading.” *International Journal of Geomechanics.* 17(10):04017090.

Ciantia, M. O., Arroyo, M., Calvetti, F., Gens Solé, A. (2015). “An approach to enhance efficiency of DEM modelling of soils with crushable grains.” *Geotechnique.* 65(2): 91–110.

Ciantia, M. O., Arroyo, M., O’Sullivan, C., Gens, A., and Liu, T. (2019). “Grading evolution and critical state in a discrete numerical model of Fontainebleau sand.” *Geotechnique*. 2019; 69(1):1–15.

Charlie, W. A., Ross, C. A., and Pierce., S. J. (1990). “Split-Hopkinson pressure bar testing of unsaturated sand.” *Geotech. Testing Journal*. 13(4):291–300.

Chen, W., Zhang, B., and Forrestal, M. J. (1999). “A Split Hopkinson Bar Technique for Low-Impedance Materials.” *Experimental Mechanics*, 39, 81-85 (1999).

Cundall, P. A., and Strack, O. D. L. (1979). “A discrete numerical model for granular assemblies.” *Geotechnique.* 29(1):47–65.

Davies, E. D. H., and Hunter, S. C. (1963). “The dynamic compression testing of solids by the method of the split Hopkinson pressure bar.” *Journal of the Mechanics of Physics and Solids*. 11(3): 155–179.

De Bono, J.P., and McDowell, G.R. (2014). “DEM of triaxial tests on crushable sand.” *Granular Matter*. 16(4): 551–562.

DeBono, J. P., McDowell, G. (2016). “Particle breakage criteria in discrete element modelling.” *Geotechnique*. 66: 1014–1027.

Felice, C. W. (1985). “The response of soil to impulse loads using the S.H.P.B technique.” Ph.D. thesis, Dept. of Civil Engineering, Univ. of Utah.

Felice, C. W., Gaffney, E. S. and Brown. J. A. (1987). “Dynamic high stress experiments on soil.” *Geotechnical Testing Journal*. 10(4): 192–202.

Gama, B. A. (2004). “Split Hopkinson pressure bar technique: Experiments,analyses and applications.” Ph.D. dissertation, Dept. of Material Science, Univ. of Delaware.

Gama, B. A., Lopatnikov, S. L. and Gillespie, J. W. (2004). “Hopkinsonbar experimental technique: A critical review.” *Applied Mechanics*. 57(4): 223–250.

Gray, G. T. (2000). “Classic split-Hopkinson pressure bar testing.” In *ASM handbook, mechanical testing and evaluation*, 462–476. MaterialsPark, OH: ASM International.

Hanley, K. J., O’Sullivan, C., and Huang., X. (2015). “Particle-scale mechanics of sand crushing in compression and shearing using DEM.” *Soils and Foundations*. 55(5): 1100–1112.

Huang, B., Bathurst, R. J., and Hatami, K. (2009). “Numerical study of reinforced soil segmental walls using three differ-ent constitutive soil models.” *Journal of Geotech. and Geoenviron. Eng.* 135(10): 1486–1498.

Huang, J., Xu, S. and Hu., S. (2013). “Effects of grain size and gradationon the dynamic responses of quartz sands.” *Int. J. Impact Eng.* 59: 1–10.

Huang, J., Xu, S. and Hu., S. (2014). “Influence of particle breakage on the dynamic compression responses of brittle granular materials.” *Mechanics of Material*. 68(1): 15-28.

Katzenbach, R. and Shmitt, A. (2004). “High-rise buildings in germanysoil–structure interaction of deep foundations.” In: *Proceedings of the 5th international conference on case histories in geotechnical engineering*, New York.

Kermani, E., Qiu, T., and Li, T. (2015). “Simulation of collapse of granular columns using the discrete element method.” *Int J Geomech*. 15(6):04015004.

Kolsky, H. (1949). “An investigation of the mechanical properties of materials at very high rates of loading.” *Proc. Royal Soc. London B* 62(11):676–700

Kozicki, J., Niedostatkiewicz, M., Tejchman, J., and Mühlhaus, H. B. (2013). “Discrete modelling results of a direct shear test for granular materials versus FE results.” *Granul. Matter*. 15(5): 607–627

Kwok, C. Y., and Bolton, M. D. (2013).“DEM simulations of soil creepdue to particle crushing.” *Geotechnique*, 63(16): 1365–1376

Lobo-Guerrero, S., and Vallejo, L. E. (2005). “Discrete element method evaluation of granular crushing under direct shear test conditions.” *Journal of Geotechnical and Geoenviron. Eng.* 131: 1295–1300

Luo, H., Lu, H., Cooper, W. L. and Komanduri. R. (2011). “Effect of mass density on the compressive behavior of dry sand under confinement athigh strain rates.” *Exp. Mech.* 51(9): 1499–1510.

Luo, H., Cooper, W. L. and Lu, H. (2014). “Effects of particle size and moisture on the compressive behavior of dense Eglin sand under confinement at high strain rates.” *Int. J. Impact Eng.* 65: 40–55.

Martin, B. E., Chen, W., Song, B. and Akers, S. A. (2009). “Moisture effects on the high strain-rate behavior of sand.” *Mech Mater.* 41(6): 786-798.

Minh, N. H. and Cheng, Y. P. (2013). “A DEM investigation of the effect of particle-size distribution on one-dimensional compression.” *Geotechnique* 63(1): 44–53.

Nakata, Y., Kato, Y., Hyodo, M., Hyde, A. F. L., and Murata, H. (2001). “One-dimensional compression behaviour of uniformly graded sand related to single particle crushing strength.” *Soils Found*. 412: 39–51.

Ravichandran, G., and Subhash, G. (1993). “Critical appraisal of limiting strain rates for compression testing of ceramics in a split Hopkinson pressure bar.” *Journal of American Ceramic Society*. 77: 263-267.

Roessler, T. and Katterfeld, A. (2018). “Scaling of the angle of repose test and its influence on the calibration of DEM parameters using upscaled particles.” *Powder Technology*. 330: 58–66.

Ross, C. A., Nash, P. T. and Friesenhahn, G. J. (1986). “Pressure waves in soils using a split Hopkinson’s pressure bar.” Report No. ESL-TR-86-29. Panama City, FL: Engineering and Services Laboratory, Air Force Engineering and Service Center, Tyndall Air Force Base.

Salot, C., Gotteland, P., and Villard, P. (2009). “Influence of relative density on granular mate-rials behavior: DEM simulations of triaxial tests.” *Granul. Matter*. 11(4): 221–236.

Semblat, J. F., Luong., M. P. and Gary, G. (1999). “3D-Hopkinson bar: New experiments for dynamic testing on soils.” *Soils Found.* 39(1): 1–10.

Song, B., and Chen. W. (2004). “Dynamic stress equilibration in split hopkinson pressure tests on soft materials.” *Exp. Mech*. 44(3): 300–312.

Song, B., Chen, W. and Luk, V. (2009). “Impact compressive response of dry sand.” *Mech. Mater*. 41(6): 777–785.

Tillotson, J. H. (1962). “Metallic equations of state for hypervelocity impact.” Report GA-3216, General Atomic, San Diego, CA.

Wang, Z., Hao, H. and Lu, Y. (2004). “A three-phase soil model for simulating stress wave propagation due to blast loading.” *Int. J. Numer. Anal.Methods Geomech.* 28(1): 33–56.

Wang, Z., Hao, H. and Lu, Y. (2004). “Numerical investigation of effects of water saturation on blast wave propagation in soil mass.” *J. Eng. Mech.* 130(5): 551–561.

Wang, S., Shen, L., Maggi, F., El-Zein, A. and Nguyen. G. D. (2017). "Uniaxial compressive behavior of partially saturated granular mediaunder high strain rates." *Int. J. Impact Eng.* 102: 156–168.

Xiao, Y., Yuan, Z., Chu, J., Liu, H., Huang, J., Luo, S. N., Wang, S. and Lin. J. (2019). "Particle breakage and energy dissipation of carbonate sandsunder quasi-static and dynamic compression."*Acta Geotech.*14 (6):1741–1755.

Yang, Y. and Yu, H.-S. (2006). "Application of a non-coaxial soil model inshallow foundations." *Geomech. Geoeng.*, 1(2): 139–150.

Yu, F. (2017). "Particle breakage and the drained shear behavior of sands." *Int. J. Geomech*. 17(8): 04017041.

CHAPTER 2

SIMULATION OF SPLIT HOPKINSON PRESSURE BAR TESTS ON SANDS WITH LOW WATER CONTENTS

This chapter is published as: Prabhu, S.S and Qiu, T. (2020). "Simulation Of Split Hopkinson Pressure Bar Tests On Sands With Low Water Contents" *Journal of Engineering Mechanics*, ASCE, 146 (8), 04020082.

Keywords: Equation of State; High Strain Rate; Impact Loading; Numerical Modeling; Sand; Split Hopkinson Pressure Bar; Water Content

Abstract

The stress-strain response of sand at high strain rate is an important topic. However, most of the numerical studies concentrated on sands at high water contents and were not able to capture the softening and subsequent stiffening stress-strain behavior observed at low water contents. In this study, split Hopkinson pressure bar (SHPB) tests of sands were numerically simulated and the equations of state (EOS) at different water contents were calibrated using back calculation. The back-calculated EOSs were used to calibrate a three-phase model capable of capturing the sand response at any water contents. The response

predicted by the three-phase model was validated by comparing the numerical and experimental stress-strain responses. A parametric study was carried out to understand the effect of interface friction and aspect ratio on the validity of the SHPB results by considering different aspect ratios and interface frictions for the specimens. The results showed that specimens with higher aspect ratio take longer time to achieve stress equilibrium while specimens with interface friction never attain perfect stress equilibrium.

2.1 Introduction

The stress-strain response of geomaterials at high strain rate is an important topic that has been studied extensively. Sand is widely used in the field for the protection of underground structures against surface or air blasts, shear waves, etc. Earlier studies on sand at high strain rates were carried out using high strain-rate oedometer tests (Emerson and Hedron, 1971). Recently, Split Hopkinson Pressure Bar (SHPB) tests (e.g., Felice, 1985) and flyer plate tests (e.g., Chapman et al., 2006) have gained popularity. Among these tests, the SHPB is the most widely-used technique because its range of strain rate (10^2~10^4/s) is of interest to many engineering problems. The SHPB was developed by Kolsky (1949) and since then has been used extensively to understand the response of polymers, metals, alloys and other materials at high strain rates (Davis and Hunter, 1963; Follansbee, 1986). The evolution of SHPB technique through the years has been well documented in detail by Gama et al. (2004).

Recently, SHPB tests have gained popularity in the field of geotechnical engineering to understand the high strain-rate response of sands (Felice 1985). Felice et al. (1987)

concluded that the response of dry sand was independent of the strain rates considered, and later similar results were reported by Song et al. (2009). Past research has shown that water content plays a crucial role in the mechanical behavior of sand; however, the effect of water content on the stress-strain response of sand in SHPB tests is seldom studied. In a comprehensive study, Martin et al. (2009) observed that the stress-strain response of Quickrete sand softens with an increase in water content but stiffens after a transitional water content under both pseudo-static conditions and at strain rates ranging from 350 ~ 500/s. Similar response was also observed for silty sand and silty clay by Hendron et al. (1969) and for sand by Wang et al. (2017). Luo et al. (2014) reported that the addition of water acted as a lubricant and reduced the shear stresses in the sand specimen with an increase in water content. Omidvar et al. (2012) postulated that the increase of water in the specimen gives rise to capillary forces which lead to an apparent cohesion.

Numerical modelling is a handy tool to better understand the response of sands at these high strain rates and several studies have been carried out to understand the effect of water content on the response of sand. Researchers have shown that the factor governing the response of sand at high strain rates and pressures was the Equation of State (EOS), which defines the pressure-volume relationship of the sand. Wang and Lu (2003) and Wang et al. (2004) calibrated the parameters of the three-phase model proposed by Henrych (1979) for sand specimens with high water content where the EOS was governed by water. But these parameters could not capture the EOS at low water contents as the particle rearrangement governed the deformation mechanism. Grujicic et al. (2008) used the Mie Gruneisen EOS and Huginiot plot while An et al. (2011) used a user-defined routine in LS-DYNA for EOS in their numerical simulations. Zakrison et al. (2012) and Fiserova (2006) used the model

proposed by Lyakhov and Okhtin (1977) while Laine and Sandvik (2001) used triaxial tests to derive the EOS and yield strength of the model. However, most of the models were neither able to capture the softening response prior to the transitional water content observed by Martin et al. (2009) nor predict the sand response at low pressures (~10 MPa) due to the failure of EOS to accurately capture the sand response.

Another area of interest in the SHPB tests on sands involves the validity of the SHPB test results. Gray (2000) noted that compared to stiff specimens, the low impedance of sand specimens provides numerous challenges. Some of these challenges are related to the friction between specimen and confining tube and failing to meet the condition of dynamic stress equilibrium. For SHPB test results to be valid, these challenges need to be addressed carefully. Chen et al. (2002) showed that the equations of SHPB are only valid if the specimen deforms under the condition of stress equilibrium. The general method to verify the stress equilibrium was the 3-wave method where the strains (or stresses) from incident bar were compared with the strains from transmission bar (transmitted stress) (Follansbee and Franz, 1983; Felice, 1985; Song and Chen, 2004; Luo et al., 2014). In a more direct approach, Chen et al. (2000 and 2002) used a quartz crystal at both ends of the specimen which directly measured the forces on the specimen. Aspect ratio of the specimen plays an important role in the validity of stress equilibrium. Gray (2000) postulated that for a soft specimen, the optimum value of aspect ratio was 0.25-0.5 while Chen et al. (2002) showed that rubber specimens deformed uniformly if the aspect ratio was 0.12 or smaller. Wu and Gorham (1997) and Frew et al. (2002) discussed that increasing the rise time of the wave (shaped pulse) helped the specimen achieve stress equilibrium and enabled the deformation to occur at a constant strain rate.

Another aspect is the effect of friction at the specimen–metal bar interfaces and specimen-confining tube interface. Jankowiak et al. (2011) showed that the maximum error in the stress-strain response due to friction was inversely proportional to the aspect ratio of the specimen. For SHPB tests on metals and polymers, the specimen interfaces are lubricated to reduce friction. However, in case of sand specimens, the interfaces cannot be lubricated as this might alter the saturation of the sample and thus, in most of the studies, the aspect ratio was chosen such that the effect of friction was negligible (Martin et al., 2009). Bazhenov et al. (2000) and Luo et al. (2011) showed that the effect of friction between the inner surface of the confining cylinder and sand had little to no effect on the sand response.

The primary objective of this study is to predict the mechanical response of sand at low water contents using a three-phase model. The current paper is divided into two parts. The first part focuses on calibrating the parameters of the three-phase model which could predict the EOS for any given water content at low pressures. Research/commercial code LS-DYNA (Hallquist 2013) was used to replicate the SHPB test results on Quickrete sand at different water contents reported by Song et al. (2009) and Martin et al. (2009) and to back calculate the EOS. The back calculated EOS was used to calibrate the three-phase model parameters which could then predict the EOS of sands at any water content. The calibrated model parameters were validated by comparing the simulated stress-strain responses of sand at varying water contents with the experimental results of Song et al. (2009) and Martin et al. (2009). In the second part, the validated numerical model was used to investigate the effect of water content on energy dissipation in the specimen. A

parametric study was also conducted to investigate the effect of specimen dimension and interface friction on the stress equilibrium condition.

2.2 SHPB Experiments by Martin et al. (2009) and Song et al. (2009)

Song et al. (2009) carried out SPHB tests on poorly graded dry silica sand and Martin et al. (2009) conducted similar tests using the same SHPB device on the same sand with 0% (i.e., dry), 3%, 5%, 7%, 11% and 20% moisture contents. The sand specimens had the same dimensions with a length of 9.3 mm and a diameter of 19.1 mm, resulting in an aspect ratio of 0.48, which is within the optimal range of aspect ratios taking into consideration of the stress equilibrium, inertia effect, and frictional effect. Detailed physical properties of the sand are reported in Kabir et al. (2010) and Martin (2007). The sand specimens had a porosity of 0.45. For the SHPB device, the incident bar (IB) and transmission bar (TB) have the same diameter of 19.1 mm, and lengths of 4100 mm and 2440 mm, respectively. Strain gauges were attached to the IB and TB and the strains measured were converted into stress-strain response (see Fig. 2.1) using the classic SHPB equations as reported in Gama (2004). It is evident from Fig. 2.1 that the stiffest stress-strain response is provided by dry sand and, with addition of water, the stiffness of the sand specimen decreases initially till a transitional water content of 7% and increases afterwards.

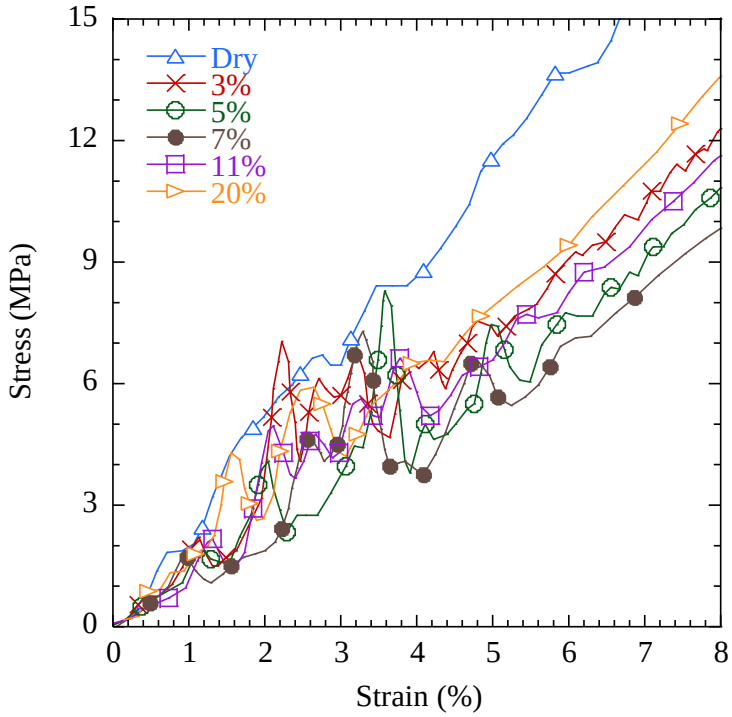

Fig. 2.1. Stress-strain curves of sand at varying moisture contents (data digitized from Song et al., 2009 and Martin et al., 2009)

2.3 Numerical Modelling

2.3.1 Mesh

Numerical simulations of the SHPB tests conducted by Song et al. (2009) and Martin et al. (2009) were carried out using LS-DYNA. Based on the results of a mesh sensitivity analysis, a computationally efficient mesh as shown in Fig. 2.2 was created for the study, where ε_i, ε_r, and ε_t represent the incident, reflected, and transmitted strains, respectively. The Lagrangian mesh consisted of eight-node fully-integrated solid elements. Taking advantage of the symmetry, only a quarter of the system was modelled. A biased mesh was used for the incident and transmission bars with a higher mesh density near the specimen.

The center of the specimen was taken as the origin. The displacement of the nodes of IB, TB, specimen and confining tube for $x = 0$ were restricted in the x direction while the displacement for $y = 0$ was restricted in the y direction. The incident and transmission bars were made of steel. Two types of tubes were used to confine the sand specimen: a polycarbonate tube and a steel tube. Song et al. (2009) noted that during the experiment, the polycarbonate tubes underwent high circumferential strains compared to the steel tubes which provided a near uniaxial strain condition. Hence, according to Vural and Ravichandran (2004), the polycarbonate confinement was considered to be a medium confinement while the steel confinement was considered to be a strong confinement. As the stresses experienced by the steel and polycarbonate tubes were well within the elastic range, both tubes were modelled as linear elastic with steel having an elastic modulus E =200 GPa, Poisson ratio ν=0.33 and density ρ =8100 kg/m^3 while polycarbonate having E =1.4 GPa, ν=0.3 and ρ =1500 kg/m^3. The compression wave velocity in the IB and TB was calculated to be 4969 m/s. Input stress waves from the experiments were applied at the free end of the IB. Automatic surface to surface contact was used for the IB-specimen, TB-specimen and specimen-confining tube interfaces. The effect of interface friction on the stress-strain response of the specimen was minimal (Kabir et al., 2010) and thus the interfaces were considered to be frictionless.

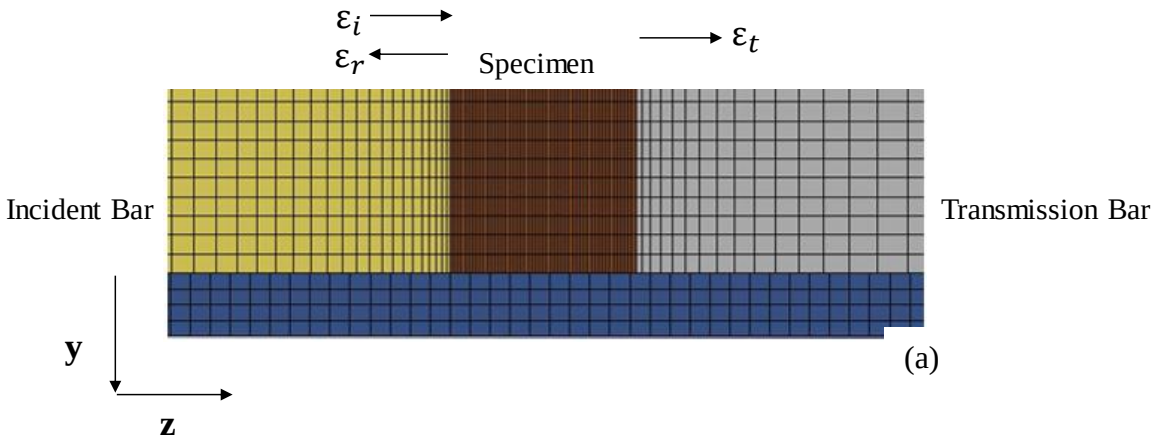

(a)

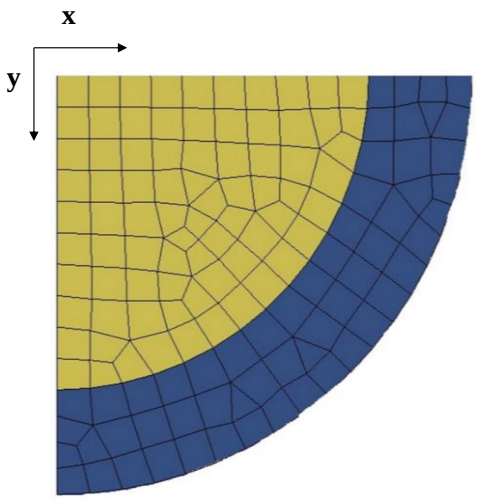

(b)

Fig. 2.2. Mesh for simulating SHPB tests: (a) plan view; (b) cross section view

2.3.2 Constitutive model

The current study utilizes a built-in pseudo tensor model (MAT_16 in LS-DYNA) for modelling the specimen. Studies showed that the pseudo tensor is highly efficient and capable of accurately replicating soil response in the field under high strain rates compared to the more complex geological cap model (Busch and Tarefder 2017; Busch et al. 2017).

Pseudo tensor model is an advanced version of soil and foam model and the user provides the yield surface and the EOS. According to the yield criterion used, the model can be implemented in two different modes in LS-DYNA: Mode I was generally used for geological problems and Mode II was used for modelling concrete (Hallquist 2006). Mode I where the strength of the model was provided by Mohr-Coulomb yield criteria was utilized in the current study. Fiserova (2014) and Zakrison et al. (2012) utilized similar yield criterion in their numerical studies and showed that the yield criterion could replicate the sand response under high strain rates. As the soil considered was uniform loose sand, an effective friction angle of 33^{o} was used to define the yield surface while typical values of 50 MPa and 0.3 were selected for the shear modulus and Poisson's ratio, respectively. For simplicity, a zero cohesion was used; this treatment is justified because 1) the apparent cohesion due to the capillary effect was negligible for the particle size considered (Lu and Likos, 2004), and 2) the frictional component dominated the shear strength due to the high compression stresses in the specimens. The effective friction angle was assumed to be independent of the water content. Hence, the same yield criterion was used for all specimens at varying water contents. It should be noted that the specimens never reached failure during the experiments due to the high confinement provided by the steel and polycarbonate tubes. Hence, the numerical simulations were found to be insensitive to the yield criterion.

2.3.4 Calibration and validation of EOS of dry sand

In LS-DYNA, EOS is implemented using an EOS-compaction relationship which defines the volumetric strain of material as a function of pressure. In this section, the EOS

was calibrated and validated for dry sand using the SHPB experiments carried out by Song et al. (2009). Ideally, the calibration and validation should be conducted using independent test data; however, given the limited quality data available in the literature on similar sand, the test data from Song et al. (2009) were split into a calibration data set and a validation data set. Calibration was carried out in two pressure ranges: at lower pressures (<35 MPa) using experimental results at a strain rate of 480/s and at higher pressures (35-65 MPa) using the experimental results at a strain rate of 900/s, both under polycarbonate confinement. Validation was conducted using the test data under steel confinement.

The points defining the EOS curve for the specimen is obtained using a back-calculation procedure (i.e., the points were varied till there was a reasonable match between the experimental and numerical stress-strain response). The stress input provided for the numerical simulation was the same as that reported by Song et al. (2009). Fig. 2.3 shows the calibrated EOS using the back-calculation method. Henrych (1979) postulated that the initial linear zone in the EOS was due to the compression of air as well as particle rearrangement in the specimen. After a certain deformation of specimen, the load is distributed to the solid particles, resulting in the stiffening response of the EOS. Fig. 2.4 shows a comparison of the corresponding stress-strain curves. It can be observed from Fig. 2.4 that the stress-strain response of sand under polycarbonate confinement for the strain rates of 480/s and 900/s showed similar results till a pressure of 27 MPa thus underlining the claim by Felice (1987) that the stress-strain response of sand was independent of the strain rate under the range of strain rates considered. In addition to the stress-strain response, Fig. 2.5 shows that the specimen experienced an approximately constant strain rate of 480/s from 125 μs to 350 μs for the test at 480/s; similarly, a good agreement

between the simulated and recorded strain rate vs. time was obtained for the test at 900/s and, hence, not presented herein. Figs. 2.4 and 2.5 show that LS-DYNA was able to predict the stress-strain response with reasonable accuracy with the calibrated EOS for dry sand.

For the validation of the EOS, the SHPB tests on dry sand under steel confinement were simulated. EOS of dry sand is dependent on the relative density of sand and denser sands tend to have a stiffer initial EOS compared to the loose sand. In the experiments by Song et al. (2009), the initial density of the sand specimens was same in both steel and polycarbonate confinement; hence, for the validation simulation, the EOS calibrated based on polycarbonate specimens (i.e., Fig. 2.3) was used. A comparison of the simulated and experimentally-obtained stress-strain responses of the sand specimen under steel confinement is also shown in Fig. 2.4. Due to the stiffer confinement, the dry sand in the steel tube exhibited stiffer response in LS-DYNA as shown in Fig. 2.4 which was consistent with the experimental results reported by Song et al. (2009).

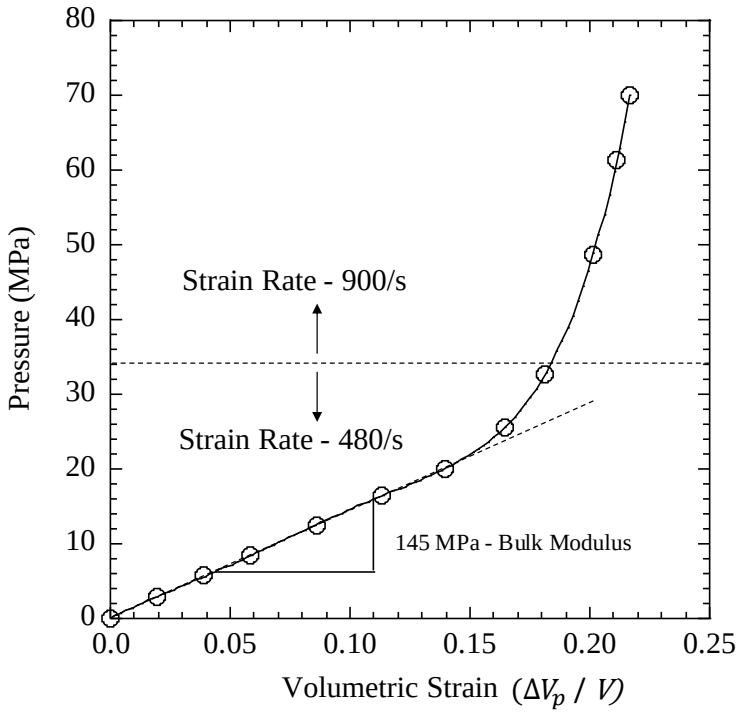

Fig. 2.3. Pressure vs. volumetric strain ($\Delta Vp/Vo$) calibrated from LS-DYNA

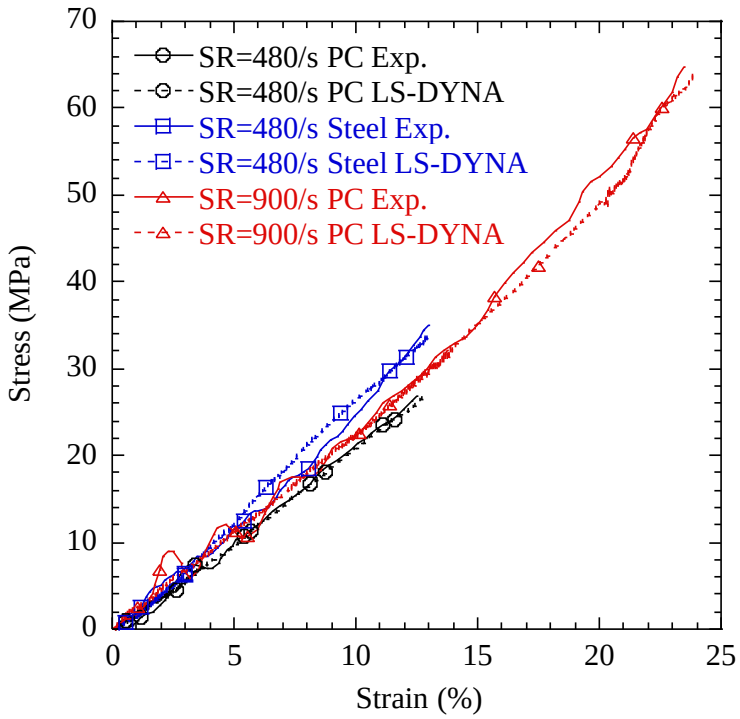

Fig. 2.4. Stress-strain response of dry sand with polycarbonate confinement and steel confinement at different strain rates

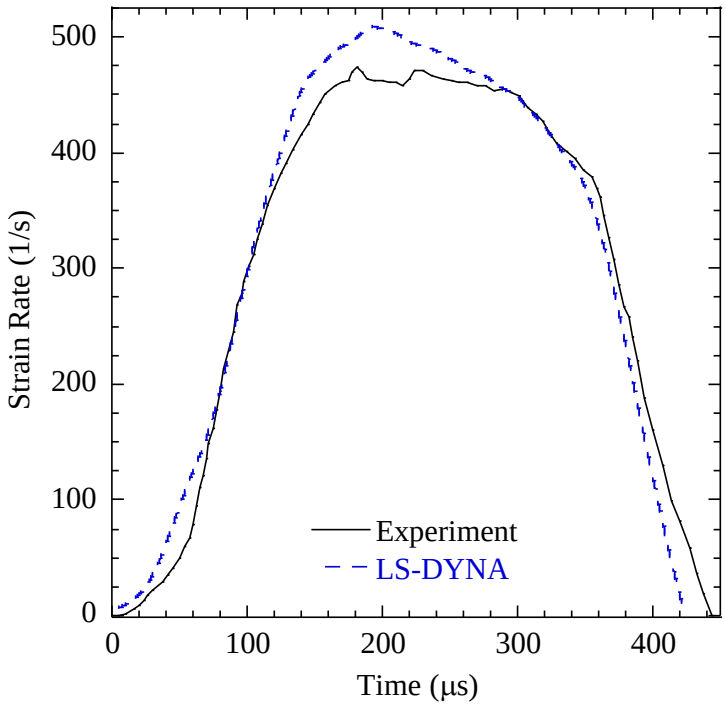

Fig. 2.5. Strain rate vs. time reported by Song et al. (2009) and LS-DYNA for polycarbonate confinement

The initial slope of the EOS in Fig. 2.3 provides the bulk modulus of the specimen K=145 MPa. Assuming a Poisson's ratio ν=0.33, the constrained modulus D of the specimen can be calculated as 235 MPa. From the stress-strain curves in Fig. 2.4, the constrained modulus (slope of the stress-strain curve) for the specimens varied from 200 MPa (strain rate 480/s) to 208 MPa (strain rate 900/s) under the polycarbonate confinement, and 230 MPa under the steel confinement. Given the D value from the steel confinement is close to the theoretical D value from the EOS, the specimen under the steel confinement can be assumed to be undergoing one-dimensional compression. However, in case of the polycarbonate confinement, as the D values were smaller than the theoretical

value, the assumption of one-dimensional deformation is not strictly valid. Consequently, the results of SHPB tests with steel confinement were used in the subsequent sections.

2.3.5 Calibration of EOS at different water contents

In this section, the stress-strain responses of sand at varying water contents in the SHPB tests by Martin et al. (2009) at strain rates of approximately 400/s on specimens under the steel confinement were modeled. Martin et al. (2009) used the same SHPB apparatus as that used by Song et al. (2009). The moisture loss in the specimen during each test was minimal due to the steel confinement provided. Due to the lack of quality data available in the literature, similar approach as that mentioned in the previous section is implemented as the data set presented in Fig. 2.1 is divided into a calibration data set and a validation data set. The calibration data set comprises of test results on sand at 0% (dry), 5%, 7% and 20% water contents while the validation data set comprises of test results at 3% and 11% water contents. Fig. 2.6 shows the EOS of sand at different water contents calibrated using the method discussed in the above section, which exhibits similar softening and stiffening behavior as observed in the stress-strain response of sand. The EOS predicted for 3% and 11% predicted using the three-phase model is discussed in detail in the next section. A comparison of the stress-strain curves predicted in LS-DYNA using the calibrated EOS and experimental results by Martin et al. (2009) is shown in Fig. 2.7. The strain rate experienced by the specimen in LS-DYNA was approximately 400/s which was in agreement with the strain rate reported in the experiments. Veyera (1994) reported that for saturated sands or sand at very high-water contents, the specimen stiffened at very small strains due to the expulsion of air from the voids and the subsequent loading of water (i.e.,

lock-up behavior). However, in the current study the volumetric strains were much smaller than the porosity of the specimen and the air was not completely expelled out of the specimen. The effect of the "incompressibility" of water was thus negligible and the lock-up behavior was not observed. The EOS calibrated for sand specimens was utilized to calibrate a three-phase model that could effectively predict the EOS of sand at any given water content. An important observation made by Martin et al. (2009) in the SHPB experiments was the oscillations observed for the stress-strain response predominant in the strain range of 2-4%. Martin et al. (2009) postulated that this might be due to the friction at the interfaces. However, the numerical simulations could not capture these oscillations even in simulations with interface friction. Although the current study could not capture the oscillations, the slope of the stress-strain response of all the specimens could be replicated with reasonable accuracy by the numerical simulations.

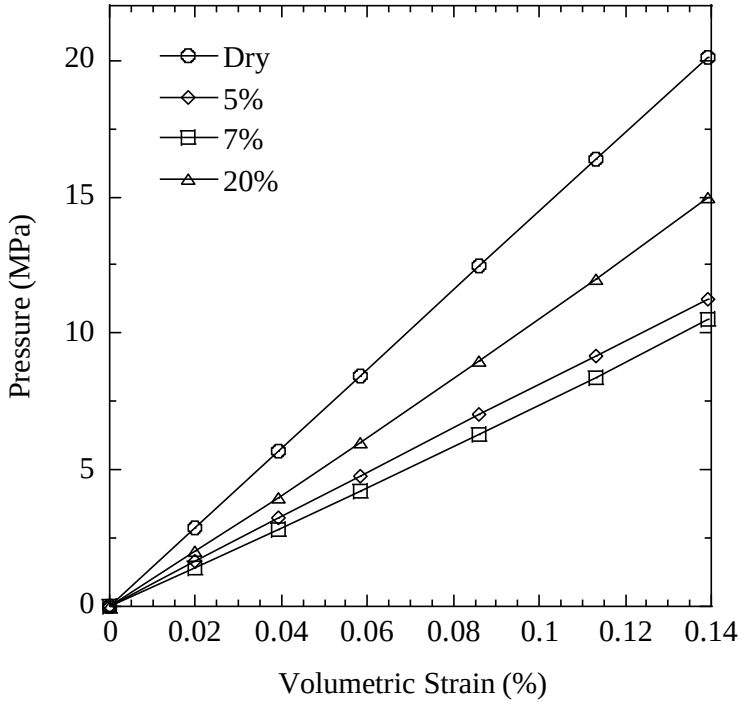

Fig. 2.6. Pressure–volumetric strain (EOS) back-calculated by LS-DYNA for different water contents

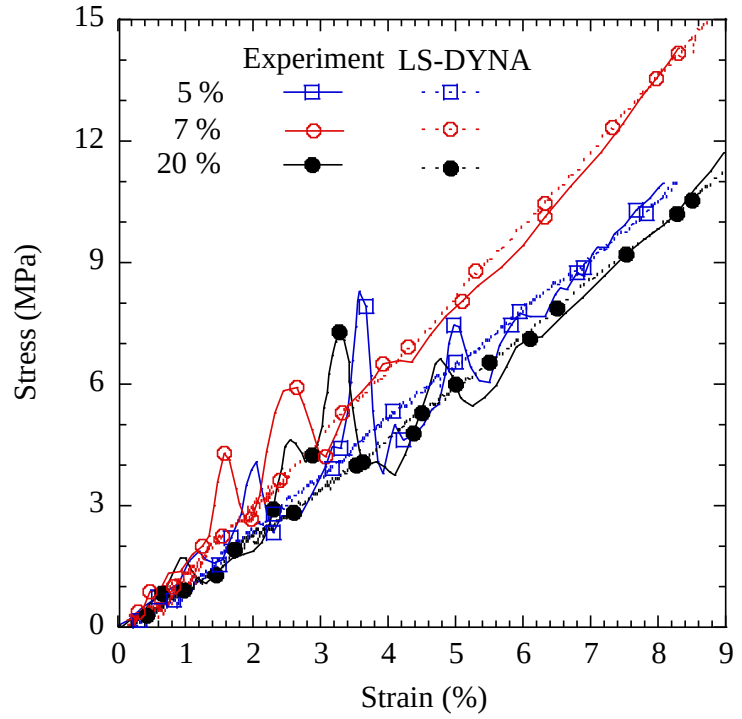

Fig. 2.7. Stress-strain responses of sand at 5%, 7% and 20% water contents

2.3.6 Calibration and validation of Three-Phase model

The Kandaurs model postulated by Henrych (1979) and modified by Wang et al. (2004) is used in the current study to predict the EOS of sand at low water contents and low pressures. In this model, soil was considered to be constituted of three phases: solid grains, water, and air. The soil skeleton was assumed to be a combination of solid blocks with voids between them which are filled with air and water and the solid blocks were assumed to be bonded together using elastobrittle bonds. The deformation of the soil skeleton was accounted for by two simultaneously-acting mechanisms: 1) the compression of individual phases in the soil, and 2) the deformation of elastobrittle bonds and particle rearrangement. The schematic diagram of the conceptual model is shown in Fig. 2.8. For sand at low water contents, the first mechanism accounts for deformation at low pressures while the second mechanism dominates at high pressures; for sands at high water contents, however, the second mechanism dominates at both low and high pressures.

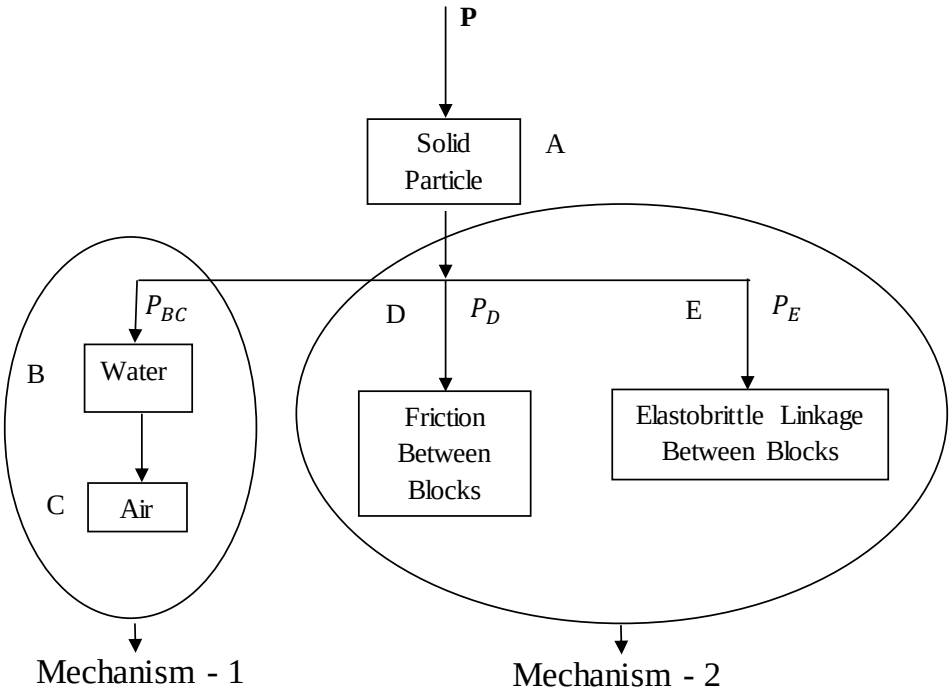

Fig. 2.8. Schematic diagram of three-phase model based on Henrych (1979)

In the model shown, branch A corresponds to the pressure taken due to the compression of solid particles; branch BC corresponds to the pressure taken due to the compression of water and air; branch D corresponds to the pressure contribution by friction between solid particles; and branch E corresponds to the pressure contribution due to the deformation of elastobrittle bonds. Branch BC corresponds to the first mechanism while branches D and E correspond to the second mechanism. When a pressure P is applied on sand, it is divided among these three branches and is given as the sum of pressures in individual branches:

$$P = P_D + P_E + P_{BC} \tag{2.1}$$

where P is the total applied pressure, P_D is the pressure carried by friction, P_E is the pressure carried by elastobrittle bond, and P_{BC} is the pressure carried by volumetric compression of voids (air and water). Accordingly, the volume relationship of the soil is given by:

$$V = V_s + V_p \tag{2.2}$$

where V is the total volume of the soil, V_s is the volume of the solid phase, V_p is the volume of the voids, and $V_p = V_a + V_w$ where V_a is the volume of air and V_w is the volume of water. The contribution from each mechanism is discussed below.

(i) Contribution to EOS from mechanism 1

In the first mechanism, pressure is carried by individual phases undergoing volumetric deformation and the EOS of individual phases was treated separately. EOS of water, air and solid is provided by (Lyakhov et al., 1972):

$$p_w = p_{wo} + \frac{\rho_{wo}\, {c_{wo}}^2}{k_w}\left[\left(\frac{\rho_w}{\rho_{wo}}\right)^{k_w} - 1\right] \tag{2.3}$$

$$p_s = p_{so} + \frac{\rho_{so}\, {c_{so}}^2}{k_s}\left[\left(\frac{\rho_s}{\rho_{so}}\right)^{k_s} - 1\right] \tag{2.4}$$

$$p_a = \left(\frac{\rho_a}{\rho_{ao}}\right)^{k_a} P_{ao} \tag{2.5}$$

where c_{wo} is speed of sound in water (typical value 1500 m/s), ρ_{wo} is the initial density of water (1000 kg/m^3), k_w is a constant (typical value 7), ρ_{so} is the density of solid (2650 kg/m^3), c_{so} is the speed of sound in solid (4500 m/s), k_s is constant (typical value 3), P_{ao} (100 kPa) is the initial pressure of the air, ρ_{ao} is the initial density of air (1.225 kg/m^3), ρ_a is the density of air at a pressure p_a, and k_a is the isentropic exponent (typical value 1.4). Pressure P_{BC} is carried by the voids, i.e. the same pressure P_{BC} acts on both air and water in the voids.

(ii) Contribution to EOS from mechanism 2

The pressure carried by the second mechanism was due to the branches D and E in Fig. 2. 8. The pressure carried by branch D was proportional to the friction between the particles and was given by:

$$P_D = f\, K_p\, \Delta V_p \tag{2.6}$$

$$\Delta V_p = V_p - V_{po} \tag{2.7}$$

where f (typically 0.56) is the coefficient of friction between soil particles, K_p is the coefficient of proportionality, and V_{po} is the initial voids in the soil. Wang et al. (2004) noted that the value of K_p varies with water content. For the pressure P_E carried by the elastobrittle bond between the solid blocks, Henrych (1979) derived a simple model with P_E proportional to the change in void in the sample and was given by:

$$P_E = \frac{E_o\, \Delta V_p\, e^{B\, \Delta V_p}}{V_p} \tag{2.8}$$

where B is assumed to be -5 irrespective of water content of the sand (Wang et al., 2004; Lu and Wang, 2006; and Wang et al., 2008) and E_o varies with water content.

For the three-phase model, Henrych (1979) derived the governing differential equation for the EOS as:

$$dP - \left(dV - \frac{\delta V_s}{\delta P} dP\right) \left[\left(\frac{\delta V_w}{\delta P_{BC}} + \frac{\delta V_a}{\delta P_{BC}}\right)^{-1} + \frac{\delta P_D}{\delta V_p} + \frac{\delta P_E}{\delta V_p}\right] = 0 \tag{2.9}$$

The EOS calibrated using the numerical simulation in the previous section was used to calibrate the three-phase model parameters for different water contents and at low pressure ranges (10-20 MPa). Luo et al. (2014) explained that an addition of water into dry sand lubricates contact points between the sand grains which reduces the friction between particles while Omidvar et al. (2012) postulated that the addition of water introduces an apparent cohesion in sand. The reduction in friction was accounted in the current model by

decreasing the parameter K_p as water content increases while apparent cohesion was accounted by the parameter E_o. It was assumed that the lubrication was effective till a water content of 7 % and addition of water beyond 7 % did not reduce the friction significantly. Thus, for the water contents (7-20 %) above the transitional water content, the pressure taken by branch D (friction component) was assumed to be constant (accounted by a constant K_p). The effect of apparent cohesion was assumed to be minimum below the transitional water content and thus the load carried by branch E was assumed to be a constant minimum value (accounted by a constant E_o) in this range of water content. Wang et al. (2004) calibrated the value of E_o to be 20 for sands at very high-water contents including saturated condition. It was noted that in the current study, the sand at 20% water content had the void ratio and water content similar to the sand used by Wang et al. (2004); thus, E_o value for the sand at 20 % water content was taken to be 20. It is assumed that the value of E_o linearly increases from 7 % to 20 % water content. The variation of E_o and K_p with water content can be obtained by solving Equation (2.9) and is shown in Fig. 2.9. It should also be noted that more experiments on sand at different water contents are necessary to increase the accuracy of the parameters calibrated.

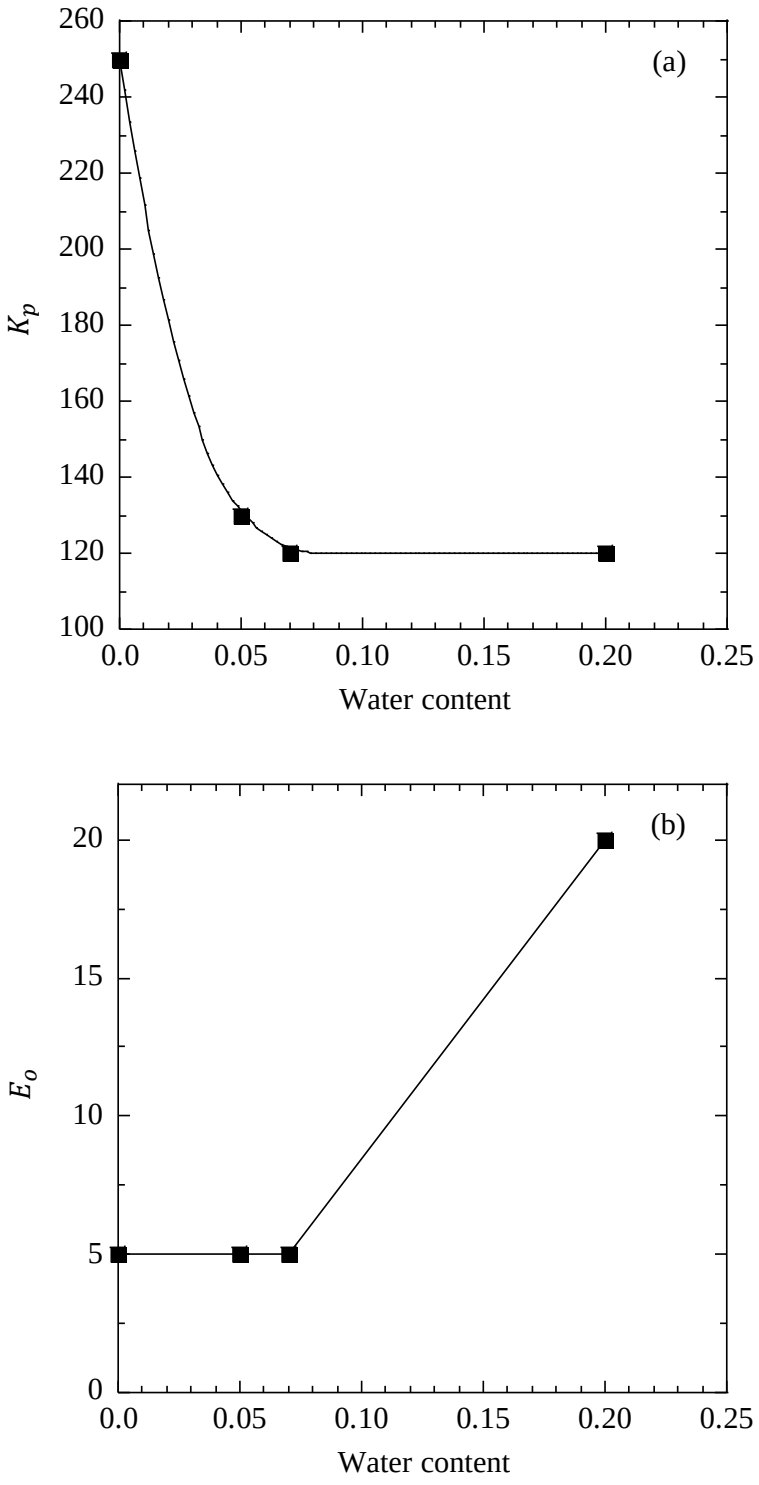

Fig. 2.9. Variation of model parameters: (a) K_p; and (b) E_o

The calibrated curves of E_o and K_p from the above section along with Equation (2.9) were used to predict the EOS of sand at water contents of 3% and 11%. The predicted EOS is shown in Fig. 2.6. The EOS calibrated in the current study was consistent with the trend observed in the stress-strain response as the EOS softens till a water content of 7% and stiffens up after the transition water content. Fig 2.10 shows the contributions from different components: P_{BC}, P_D, and P_E to the predicted EOS for water contents 3% and 11%. It is evident that for both of the EOS considered, the contribution from mechanism 1 (i.e., P_{BC}) was negligible (~200 kPa) and the contribution from friction between the blocks (i.e., P_D) dominated. For 11% (K_p=120; E_o=8) water content, the contribution from elastobrittle bond (i.e., P_E) had a relatively higher contribution to the EOS compared to the case of 3% (K_p=155; E_o=5) water content. The predicted EOS was implemented in LS-DYNA to simulate the SHPB tests for specimens at these two water contents. The simulated stress-strain responses are compared with the experimental responses reported by Martin et al. (2009) in Fig. 2.11 and a reasonable agreement is observed. The strain rate experienced by the specimen in LS-DYNA was ~ 400/s which was similar to the values reported in the experiments.

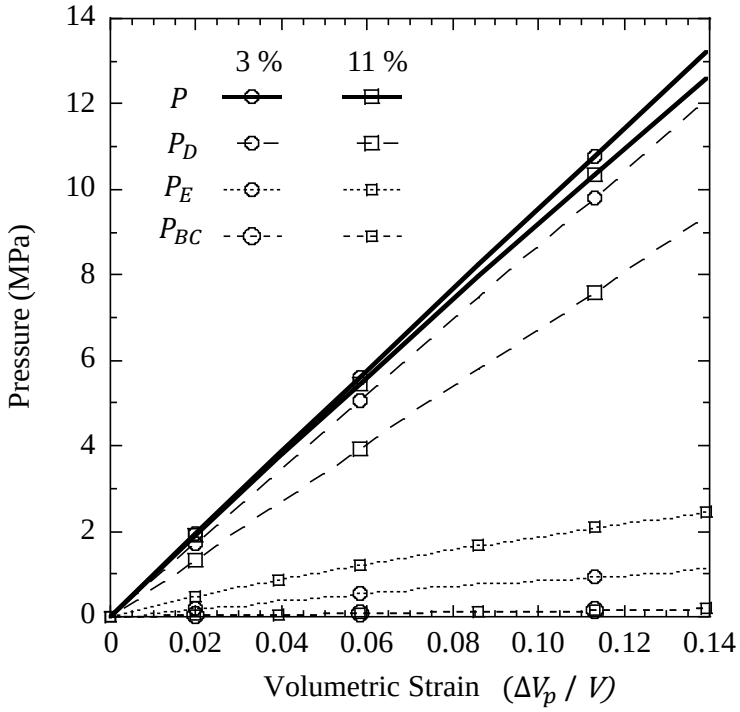

Fig. 2.10. EOS and components of EOS from the three-phase model

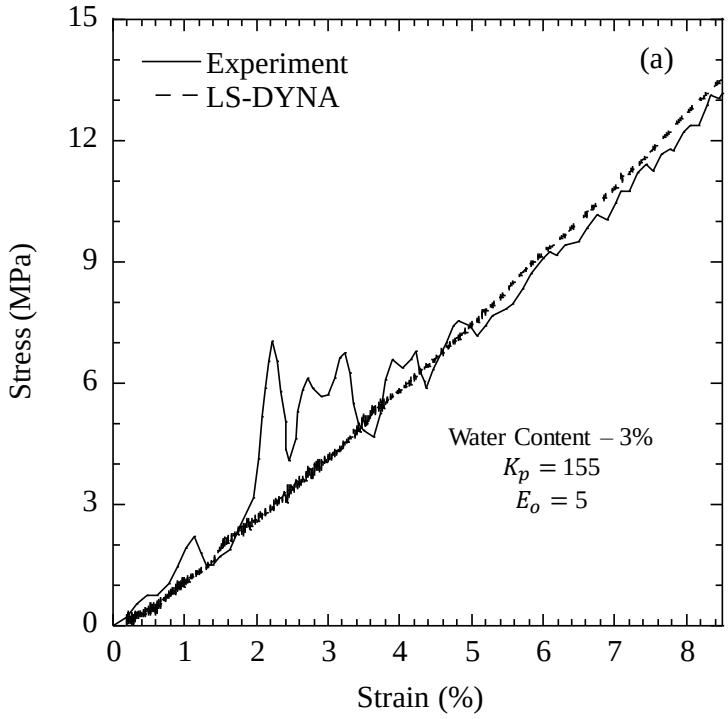

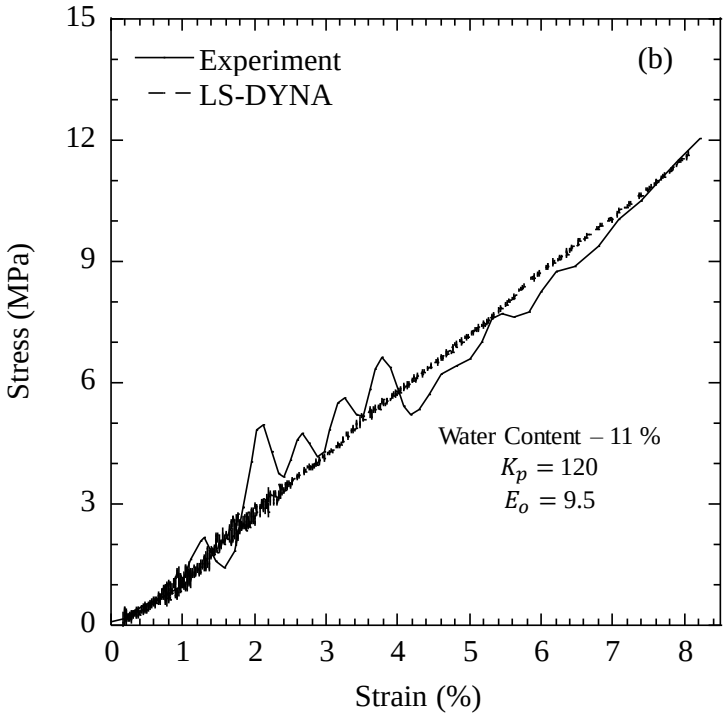

Fig. 2.11. Stress-strain curves by Martin et al. (2009) and LS-DYNA for: (a) 3% water content; (b) 11% water content

2.4 Parametric Study

2.4.1 Energy Dissipation

Sand effectively absorbs energy from the shock waves during explosions and hence finds its application in protecting the structures below the ground in the event of explosions. Huang et al. (2013) observed that higher energy was absorbed by the sand after the initialization of particle breakage or yielding. McDowell (2002) showed that the breakage stress of sand was a function of the particle size and was in the range of 10~15 MPa. Sand dissipates energy through a combination of particle rearrangement and particle breakage. The major energy dissipation mechanism at low stresses is particle rearrangement while at

high stresses this is governed by particle breakage. It is difficult to quantify the energy dissipation based on the mechanism and hence, total energy dissipation is considered. In the current section, effect of water content on the energy dissipation is studied. It is difficult to measure the absorbed energy in the field or experiments and hence we rely on analytical equations to quantify the energy absorbed. According to the wave theory of Yang et al. (2010), when an input wave energy was applied to a specimen, a part of this energy was reflected, a part was transmitted and a part was absorbed by the specimen. For a bar of area A_o, modulus E'_o, wave propagation velocity c_o, and material density per length $\rho_o A_o$, the energies carried by incident, reflected and transmitted waves are given by Equations (2.11), (2.12) and (2.13), respectively.

$$W_i = \frac{A_o}{c_o \rho_o} \int_0^t {\sigma_i}^2 \, (t') \, dt' \tag{2.11}$$

$$W_r = \frac{A_o}{c_o \rho_o} \int_0^t {\sigma_r}^2 \, (t') \, dt' \tag{2.12}$$

$$W_t = \frac{A_o}{c_o \rho_o} \int_0^t {\sigma_t}^2 \, (t') \, dt' \tag{2.13}$$

where W_i, W_r, and W_t are the energy of the incident wave, reflected wave, and transmitted wave, respectively, and σ_i, σ_r, and σ_t are the incident, reflected, and transmitted stresses, respectively. The percentage of energy dissipation was defined as the ratio of energy loss ($W_{loss} = W_i - W_r - W_t$) to the incident energy expressed as a percentage ($W_{loss}/W_i \times 100\%$).

Fig. 2.12 presents the percentage of energy dissipation of sand specimen for different water contents at 8% axial strain and the effect of particle breakage can be neglected because the corresponding axial stress levels were relatively low (see Figs. 2.4, 2.7, and 2.11). Yang et al (2009) showed that the energy dissipation of a specimen was dependent

on the sample porosity. In the current study, as all the specimens had the same porosity, the difference in energy dissipation was attributed only to the change in water content in the specimens. It can be observed from Fig. 2.12 that the percentage of energy dissipation was highest for the dry sand and as the water content increases, there is a drastic decrease until a water content of 7%. The decrease in energy dissipation can be attributed to the decrease in friction between the particles which is accounted for by the decrease in K_p in the three-phase model (see Fig. 2.9). However, as the water content increases from 7 % to 20 % the energy loss in the specimen increases marginally which can be attributed to the increase in E_o in the three-phase model (see Fig. 2.9).

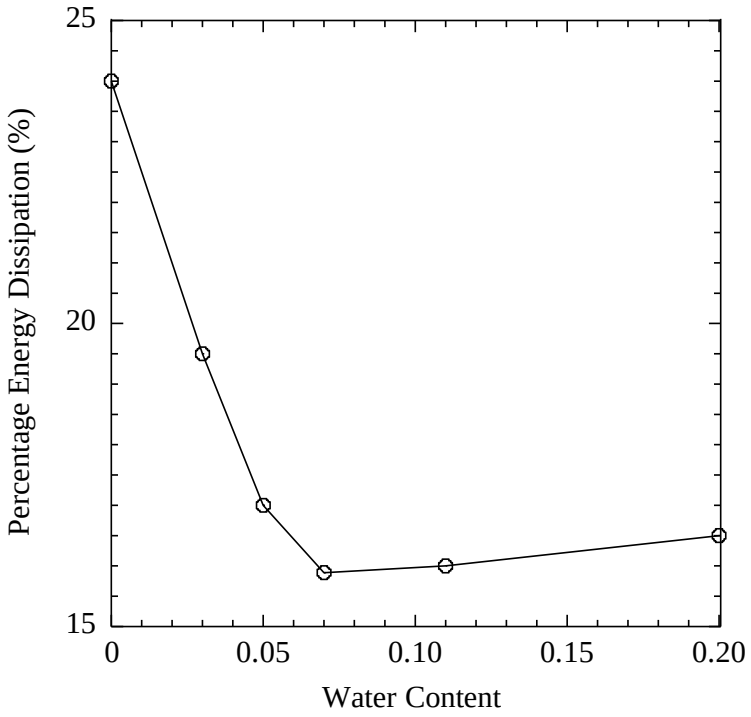

Fig. 2.12. Percentage of energy dissipation vs. water content using stress-strain curves from LS-DYNA

2.4.2 Effect of Specimen Length and Interface Friction on Stress Equilibrium and Stress Uniformity

Gray (2000) concluded that for the stress-strain analysis to be valid, the stress-equilibrium and stress uniformity condition should be satisfied, i.e., the stresses at the IB-specimen interface and TB-specimen interface are equal. For soft specimens, the aspect ratio (ratio of length L of the specimen to its diameter d) played an important role in achieving stress equilibrium and uniformity. Chen et al. (2002) observed that even though the ideal aspect ratio for soft specimen was 0.5-1, specimens like rubber could only achieve stress equilibrium and stress uniformity at much lower aspect ratios. However, for small aspect ratios, the effect of interface friction might be significant and proper lubrication need to be applied as suggested by Zhong et al. (2015).

Several SHPB tests have been carried out on sand (Luo et al. 2011; Song et al. 2009; Felice et al. 1987; Wang et al. 2017; Huang et al. 2013; Semblat et al. 1999; Charlie et al. 1990; Ross et al. 1986). The aspect ratio of the sand specimen considered in these studies were in the range of 0.15- 1 and most of the studies (except Huang et al. 2013) were carried out without lubricating the interfaces. In the current study, the calibrated LS-DYNA model for dry sand with steel confinement was used to understand the combined effect of specimen aspect ratio and interface friction on the stress equilibrium and stress uniformity in the specimen.

Butterfield and Andrawes (1972) carried out studies to understand the interface friction between steel and sand and concluded that the coefficient of friction (μ) between steel and sand ranged from 0.17 for loose sand and 0.3 for dense sand. In the current study, specimens with three aspect ratios: 0.48, 0.75, and 1 were considered and for each aspect

ratio, an interface friction of 0 (frictionless) and 0.2 (corresponding to the loose specimens simulated in the current study) were considered. The interface friction applies to IB-specimen, TB-specimen, and tube-specimen interfaces. The magnitude of the incident wave for the aspect ratio of 0.48 was the same as that considered throughout the paper while for other aspect ratios, the input stress wave was varied proportional to the L/d ratio to achieve the same strain rate for the specimen. Stress nonuniformity coefficient $\alpha(t)$ is generally used in SHPB studies to understand the uniformity of stresses experienced by the specimen and the validity of stress equilibrium condition during the SHPB tests. It is defined as the absolute value of the ratio between the stress deviation to the average stresses on the two ends of the specimen and is given by (Yang and Shim, 2005; Zhu et al., 2009):

$$\alpha(t) = \left| \frac{\sigma_i + \sigma_r - \sigma_t}{\left(\frac{\sigma_i + \sigma_r + \sigma_t}{2}\right)} \right| \tag{2.15}$$

Stress nonuniformity coefficient $\alpha(t)$ reflects the state of stress uniformity in the specimen with a value of 0 reflecting a perfect uniform stress state in the specimen under stress equilibrium condition. However, previous studies (Yuan et al., 2018; Zhu et al. 2009) have chosen an $\alpha(t)$ of 0.05 as the value below which the specimen achieves stress equilibrium and stress uniformity.

Fig. 2.13(a) shows the stress nonuniformity coefficient as a function of time for different aspect ratios and interface friction values, and Fig. 2.13(b) shows the corresponding plot for the developed strain as a function of time. It can be observed that there is a 'ringing-up' time for all the specimens and the stresses are non-uniform and equilibrium condition is not satisfied in any of the specimens initially. Davis and Hunter (1963) noted that wave velocity in the specimen was the governing factor that dictates the time needed for the specimen to achieve stress equilibrium. From their studies it was

observed that the wave had to travel π times inside an ideal specimen (frictionless and infinitely stiff) to achieve stress equilibrium. Fig. 2.13(a) shows that the specimens without interface friction reaches stress equilibrium and undergoes uniform deformation eventually, while the specimens with interface friction does not strictly satisfy the stress equilibrium and stress uniformity even after considerable time. It can be observed from Fig. 2.13(a) that as the specimen aspect ratio increases, the time needed for the specimen to reach stress equilibrium also increases irrespective of the friction at the interface. It is also interesting to note that for the same aspect ratio, the specimen with interface friction takes longer to reach a lower stress nonuniformity coefficient value. However, for L/d = 0.48, the effect of friction was minimum compared to the cases of higher L/d ratios of 0.75 and 1. For higher L/d ratios of 0.75 and 1, longer time is needed for the specimen to reach a low value of $\alpha(t)$ but substantial strains would have already occurred in the specimen as observed from Fig. 2.13(b). Fig. 2.13(b) also shows that the strain rate (i.e., slope of the curves) experienced by all the specimens were the same. From the current study it can be concluded that for a specimen with L/d = 0.48, the effect of interface friction was minimal thus supporting the claim by Martin et al. (2009). Fig. 2.13 also supports the conclusion of Gray (2000) that for soft specimens including sand specimens, the aspect ratio should be smaller than 0.5 for stress equilibrium and stress uniformity considerations.

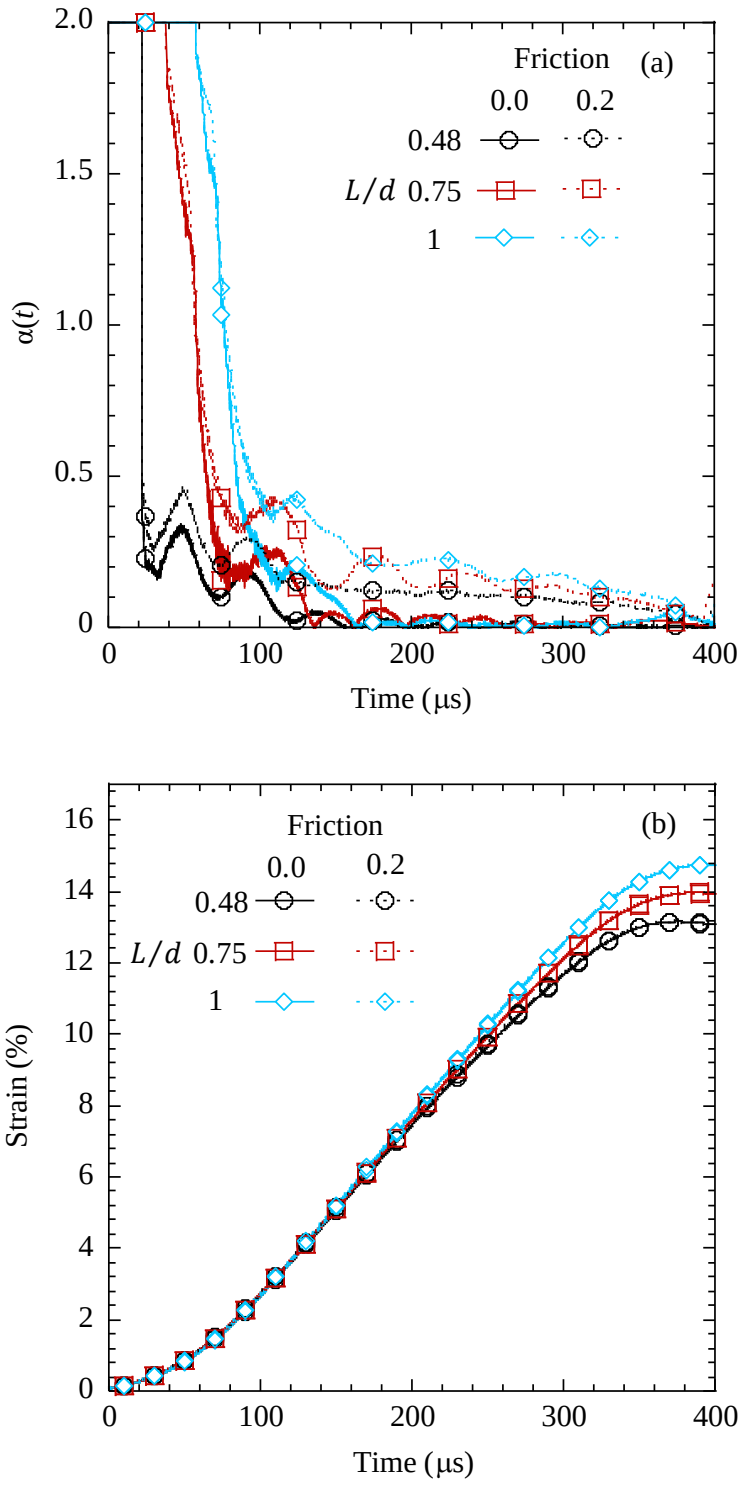

Fig. 2.13. Stress ratio and strain vs. time for specimens with different aspect ratios and different interface friction: (a) stress nonuniformity coefficient; (b) strain

2.5 Conclusions

In this paper, numerical simulations of SHPB were carried out in LS-DYNA to back calculate the EOS at different water contents using the experimental stress-strain curves. These EOS curves were then used to calibrate a three-phase model that could effectively capture the sand response at any given water content. The calibrated model was subsequently used in the numerical simulations to predict the stress-strain response of sand at different water contents and the results were compared with the experimental results. A parametric study was also carried out to understand the effect of aspect ratio and interface friction on the validity of the SHPB results. From the numerical simulations carried out, the following conclusions were obtained.

1. Initial studies on dry sand revealed that the back-calculation method implemented to calibrate the EOS was effective in capturing the sand response. It was also observed in the numerical simulation that the steel tube provided much higher confinement to the sand specimen compared to the polycarbonate tube.

2. The calibrated three-phase model could effectively capture the EOS of sand specimens at low water contents and pressures, which could be used to model the softening and stiffening response of sand as a function of water content.

3. Parametric studies showed that the energy absorption initially decreased with increase in water content till the transitional water content and marginally increased afterwards. It was also observed that specimens with higher aspect ratio attains stress equilibrium and stress uniformity only after considerable strains have already occurred in the specimen while stress equilibrium is never strictly satisfied in specimens having interface friction.

References

An, J., Tuan, C. Y., Cheeseman, B. A. and Gazonas, G. A., (2011). "Simulation of soil behavior under blast loading." *International Journal of Geomechanics*. 11(4): 323–334.

Bazhenov, V. G., Bragov, A. M., Kotov, V. L., Zefirov, S. V., Kochetkov, A. V., Krylov, S. V. and Lomunov, A.K. (2000). "Analysis of the applicability of a modified Kolsky's method for dynamic tests of soils in a deformable casing." *Journal of Applied Mechanics Technical Physics.* 41: 519–525

Busch, C. L., Tarefder, R. A. and Aimone-Martin, C. T. (2017). Deformation-Induced stability of earthen embankment dams subjected to explosive air blast loading. *International Journal of Geomechanics*.17(10): 04017090.

Busch, C. L. and Tarefder, R. A. (2017). "Evaluation of appropriate material models in LS-DYNA for MM-ALE finite element simulations of small-scale explosive air blast tests on clay soils." *Indian Geotech Journal*. 47: 173–86.

Butterfield, R. and Andrawes, K. Z. (1972). "On the angles of friction between sand and plane surfaces." *Journal of Terramechanics*. 8: 15–23.

Chapman, D. J., Tsembelis, K. and Proud, W. G. (2006). "The behavior of dry sand under shock compression." *Proceedings of Conference on Shock Compression of Condensed Matter* - 2005.

Charlie, W.A., Ross, C. A. and Pierce, S. J. (1990). "Split-Hopkinson pressure bar testing of unsaturated sand." *Geotechnical Testing Journal*. 13(6): 291-300.

Chen, W., Lu, E. and Zhou, B. (2000). "A quartz crystal embedded split Hopkinson bar for soft materials." *Experimental Mechanics*. 40: 1-6.

Chen, W., Lu, K., Frew, D. J. and Forestal, M. J. (2002). "Dynamic compression testing of soft materials." Transactions of the ASME, *Journal of Applied Mechanics*. 69: 214-223.

Davies, E. D. H. and Hunter, S. C. (1963). "The dynamic compression testing of solids by the method of the split Hopkinson pressure bar." *Journal of Mechanics and Physics of Solids.* 11: 155-179.

Emerson, M.W.C. and Hendron, A.J. (1971). "Measurement of stress and strain during one dimensional compression of large compacted soil and rockfill specimens." Contract Report S-71-4.

Felice, C. W. (1985). "The response of soil to impulse loads using the S.H.P.B technique." Ph.D. Thesis, University of Utah, Salt Lake City.

Felice, C. W, Gaffney, E. S., and Brown, J. A. (1987). "Dynamic high stress experiments on soil." *Geotechnical Testing Journal.* 10(4): 192-202.

Fiserova, D. (2006). "Numerical analyses of buried mine explosions with emphasis on effect of soil properties on loading." Ph.D. Thesis Defense College of Management and Technology, Cranfield University.

Frew, D. J., Forrestal, M. J. and Chen, W. (2002). "Pulse shaping techniques for testing brittle materials with a split Hopkinson pressure bar." *Experimental Mechanics* 42(1): 93-106.

Follansbee, P. S. and Franz, C. (1983). "Wave propagation in the split Hopkinson pressure bar." *Journal of Engineering Mechanics*. 105: 61-66.

Follansbee, P. S. (1986). “High strain rate deformation of FCC metals and alloys.” In Metallurgical Application of Shock Wave and High Strain Rate Phenomena. 451-479. Mareel Dekker, New York.

Gama, B. A. (2004). “Split Hopkinson pressure bar technique: experiments, analyses and applications.” Ph.D. Dissertation. University of Delaware.

Gama, B. A, Lopatnikov, S. L. and Gillespie, J. W. (2004). Hopkinson bar experimental technique: A critical review.” *Applied Mechanics*. 57(4): 223–250.

Gray, G.T. (2000). Classic split-Hopkinson pressure bar testing. ASM Handbook, *Mechanical Testing and Evaluation*. Materials Park, OH, 462–476.

Grujicic, M., Pandurangan, B., Cheeseman, B. A., Roy, W. N. and Skaggs, R. R. (2008). “Parameterization of the porous material model for sand with different levels of water saturation.” *Soil Dynamics and Earthquake Engineering.* 28: 20–35.

Hallquist, J. O. (2013). “LS-DYNA Keyword User’s Manual—Version R7.0.” Livermore CA: Livermore Software Technology Corporation.

Hendron, A. J., Davisson, M. T., and Parola, J. F. (1969). “Effect of degree of saturation on compressibility of soils from the defense research establishment Suffield.” Technical report, US Army Engineer Waterways Experiment Station.

Henrych, J. (1979). “The dynamics of explosion and its use.” Elsevier, Amsterdam, The Netherlands.

Huang, J., Xu, S. and Hu, S. (2013). “Effects of grain size and gradation on the dynamic responses of quartz sands.” *International Journal of Impact Engineering.* 59, 1–10.

Jankowiak, T., Rusinek, A. and Lodygowski, T. (2011). "Validation of the Klepaczko–Malinowski model for friction correction and recommendations on split Hopkinson pressure bar." *Finite Element Analysis and Design.* 47, 1191–1208.

Kabir, M. E., Song, B., Martin, B. E., and Chen, W. (2010). "Compressive behavior of fine sand." SANDIA report, Terminal Ballistics Technology Department, Sandia Laboratories; New Mexico.

Kolsky, H. (1949). "An investigation of the mechanical properties of materials at very high rates of loading." *Proceedings Royal Society London.* B62, 676–700.

Laine, L. and Sandvik, A. (2001). "Derivation of mechanical properties for sand." *4th Asia-Pacific Conference on Shock and Impact Loads on Structures* (Singapore, November), 361 – 368.

Lu, N. and Likos, W. J. (2004). "Unsaturated soil mechanics." Wiley, New York.

Luo, H, Lu, H., Cooper, W.L. and Komanduri. R. (2011). "Effect of mass density on the compressive behavior of dry sand under confinement at high strain rates." *Experimental Mechanics.* 51: 1499-1510.

Luo, H., Cooper, W.L. and Lu, H. (2014). "Effects of particle size and moisture on the compressive behavior of dense Eglin sand under confinement at high strain rates." *International Journal of Impact Engineering.* 65: 40–55.

Lyakhov, G. M, Okhitin, V. M and Chistov, A. G. (1972). "Shock waves in soils and in water near the point of an explosion." *Journal of Applied Mechanics and Technical Physics.* 13(3): 390-397.

Lyakhov, G. M. and Okhitin, V. N. (1977). "Plane waves in nonlinear viscous multicomponent media." *Journal of Applied Mechanics*. 18 (2): 241–248.

Martin, B. E. (2007). "Moisture effects on the high strain rate behavior of sand." Master of Science Thesis, University of Florida.

Martin, B. E., Chen, W., Song, B. and Akers, S. A. (2009). "Moisture effects on high strain-rate behavior of sand." *Mechanics of Materials* 41: 786 – 798.

McDowell, G. R., (2002). "On the yielding and plastic compression of sand. Soils and Foundations." 42 (1): 139–145.

Omidvar, M, Iskander, M. and Bless, S. (2012). "Stress–strain behavior of sand at high strain rates." *International Journal of Impact Engineering.* 49: 192–213.

Ross, C. A., Nash, P. T. and Friesenhahn, G. J. (1986). "Pressure waves in soils using a split Hopkinson pressure bar." Report No. ESL-TR-86e29. Florida: Engineering & Services laboratory, Air Force Engineering and Service Center, Tyndall Air Force Base; 32403.

Semblat, J. F, Luong, M. P. and Gary, G. (1999). "3D-Hopkinson Bar: New Experiments for Dynamic Testing on Soils." *Soils and Foundations.* 39(1): 1-10.

Song, B. and Chen, W. (2004). "Dynamic stress equilibration in split Hopkinson pressure tests on soft materials." *Experimental Mechanics*. 44: 300–312.

Song B, Chen, W. and Luk, V. (2009). "Impact compressive response of dry sand." *Mechanics of Materials*. 41(6): 777 -785.

Wang, Z., and Lu, Y. (2003). "Numerical analysis on dynamic deformation mechanism of soils under blast loading." *Soil Dynamics and Earthquake Engineering.* 23: 705-714.

Wang, Z., Hao, H. and Lu, Y. (2004). "Numerical investigation of effects of water saturation on blast wave propagation in soil mass." *Journal of Engineering Mechanics*. 5: 551–561.

Wang, Z., Hao, H. and Lu, Y. (2004). "A three-phase soil model for simulating stress wave propagation due to blast loading." *International Journal for Numerical and Analytical methods in Geomechanics.* 28: 33–56.

Wang, Z., Lu, Y. and Bai, C. (2008). "Numerical analysis of blast-induced liquefaction of soil." *Computers and Geotechnics*. 35: 196–209.

Wang, S., Shen, L., Maggi, F., El-Zein, A. and Nguyen, G. D. (2017). "Uniaxial compressive behavior of partially saturated granular media under high strain rates." *International Journal of Impact Engineering.* 102: 156–168.

Wu, X.J. and Gorham, D.A. (1997). "Stress equilibrium in the split Hopkinson pressure bar test." *Journal de Physique IV France Colloq.* C3 (DYMAT 97), 7: 91-96.

Veyera, G.E. (1994). "Uniaxial stress-strain behavior of unsaturated soils at high strain rates." WL-TR-93e3523. Tyndall AFB, FL: Wright Laboratory, Flight Dynamics Directorate.

Vural, M. and Ravichandran, G. (2004). "Transverse failure in thick s2-glass/epoxy fiber-reinforced composites." *Journal of composite materials.* 38: 609-623

Yang, J., Huijie, W., Yongming, Y., Qinang, H. and Ruidong, P. (2010). "Numerical simulation of mechanisms of deformation, failure and energy dissipation in porous rock media subjected to wave stresses." *Science China*. 53: 1098 – 1113.

Yang, L., M. and Shim, V., P. (2005). "An analysis of stress uniformity in split Hopkinson bar test specimens." *International Journal of Impact Engineering*. 31(2): 129–150.

Yuan, P., Ma, Q. and Ma, D. (2018). “Stress uniformity analyses on nonparallel end-surface rock specimen during loading process in SHPB tests.” *Advances in Civil Engineering.* 5406931,

Zakrisson, B., Haggblad, H. A. and Jonsen, P. (2012). “Modelling and simulation of explosions in soil interacting with deformable structures.” *Central European Journal for Engineering.* 2(4): 532–550.

Zhu, J., Hu, S.S. and Wang, L.L. (2009). “An analysis of stress uniformity for concrete-like specimens during SHPB tests.” *International Journal of Impact Engineering.* 36(1): 61–72.

CHAPTER 3

EFFECT OF PARTICLE SIZE ON HIGH-STRAIN RATE RESPONSE OF SAND

This chapter is published as: Prabhu, S.S. and Qiu, T. (2012). “Effect of Particle Size on High-Strain Rate Response of Sand.” *Geo-Congress* 2019 (GSP 310), 155-164.

Abstract

Sand is extensively used in geotechnical engineering applications due to its abundance in the field. In general, sands are subjected to very low strain rates in most geotechnical engineeringa applications; however, during air or surface blasts, sands are subjected to high strain rates and their response needs to be studied in detail. The recent years have seen an increase in the usage of split Hopkinson pressure bar (SHPB) device to study the response of sand at very high stresses (on the order of MPa) and strain rates (10~1000/s). Researchers have shown that the particle size in sand influences its mechanical behavior at low strain rates. However, the effect of particle size on the stress-strain response of sand obtained from an SHPB device where particles are subjected to high strain rates is seldom studied. The particle size could also have an influence on the stress equilibrium condition which needs to be satisfied by the specimen for the stress-strain analysis from the SHPB to

be valid. However, the afore mentioned criteria are seldom studied and need to be studied in detail. In the current study, the SHPB device is modelled using a commercial software package LS-DYNA with a coupled finite elements-discrete element method. The sand specimens are modelled using polydisperse (spheres with varying sizes) and monodisperse discrete spheres. These simulations are used to understand the variation of stress-strain response of sand as a function of particle sizes. The study also provides insight into the effect of friction at the boundaries on the stress-strain response of the specimen. The results indicate that the specimen having larger polydisperse spheres provided similar stress-strain response as the specimen having smaller polydisperse spheres. However, the monodisperse specimen provided a softer response compared to the polydisperse specimens.

3.1 Introduction

Over the past decade, there has been a rapid increase in the construction of underground structures like tunnel, reservoirs etc. These structures are strategically important and needs to be protected against events like air blast, surface explosion etc. The surrounding soil during these events is subjected to very high strain rates of the order 10^3/s and to study the impact of explosion on these structures, there is a need to study the mechanical response of overburden soil under high-strain-rate loading. As the large-scale experiments of explosions are impractical, researchers resort to small-scale laboratory experiments and numerical modellings to understand the reaction of soil under these high strain rates. For laboratory experiment, one of the main equipment used to study the high-strain-rate response is the Split Hopkinson Pressure Bar (SHPB). SHPB was introduced by Kolsky

(1949) to understand the high-strain-rate response of alloys and metals. One of the earliest studies on sand using SHPB was carried out by Felice (1985) at strain rates on the order of 1000/s. Recently, Song et al. (2009) carried out high-strainrate SHPB tests on dry sand at strain rates of ~470/s and reported their stress-strain response. Coming to the numerical studies, Discrete Element Modelling (DEM) is a handy tool to study the behavior of soil and has gained popularity in recent years as this approach connected the micromechanical properties of soil with macro-mechanical properties. In DEM, each individual grain in the soil is modelled as a particle and studies have shown that DEM could effectively replicate the quasi-static response of the soil specimens (Sullivan 2011). However, the usage of DEM was limited due to the large number of particles and contacts even in a small sample. Thus, there is a need to reduce the number of particles and contacts in the specimen without compromising the simulated material behavior.

From the simulation of triaxial tests on sand particles, Huang et al. (2014) showed that the size of the sample as well the size of the particles played an important role in the material response. Studies by Kuhn and Bagi (2009) showed that there was a minimum number of particles to accurately represent the continuum behavior of a specimen and for the 2-D DEM simulations this number was shown to be 10000. Powrie et al. (2005) was able to replicate the experimental triaxial results on Leighton Buzzard sand using bonded DEM particles having size 2.7 times of the original particle size distribution (PSD). Kermani et al. (2015) used a different approach where the mean particle size D_{50} of the sand as the representative sample size and used monodisperse spheres to represent the entire specimen. In a similar approach, Bonn and McDowell (2013) studied the particle breakage in sand using monodisperse particles with a particle size of 2 mm which was much higher

than the actual particle size. Yan and Dong (2011) noted that the response of the monodisperse particles differed from the original sand sample polydisperse distribution of particle with monodisperse specimen showing higher peak stress and a subsequent softening response. Sullivan (2011) also pointed out that the response of the sample constituting of only monodisperse particles was different from that of polydisperse sample. However, all the above studies were carried out on quasi-static conditions and the effect of increasing the particle size on the material response at high strain rates is seldom studied. The paper addresses this gap in knowledge and studies the effect of particle size distribution on the specimen response at high strain rates (470/s) by carrying out numerical simulations. The SHPB experiment on dry sand reported by Song et al. (2009) was numerically simulated and the results were compared to provide insights into the effect of PSD. The study also discusses the stress equilibrium in the sample and validity of the numerical simulations. Finally, the paper discusses the effect of interface friction in the SHPB on the stress-strain response of the material.

3.2 Experimental Studies on SHPB by Song et al. (2009)

Song et al. (2009) carried out SHPB studies on uniformly-graded dry silica sand with rounded particles. The specimen had a dimension of 9.3 mm length and 19.1 mm diameter which corresponds to an aspect ratio of 0.48. The specimen was prepared in loose condition with a void ratio of 0.45 and was confined in a steel tube of 50 mm in length. The incident bar (IB) and transmission bar (TB) were made of steel with lengths of 4100 mm and 2400 mm, respectively, with both having a diameter of 19.1 mm. The tests were carried out at a

strain rate of ~ 470/s. The input stress in the IB was generated using a striker bar and the strains in the IB and TB were measured using strain gauges. The detailed description of the input stress wave and output stress wave used in the experiment are provided in Song et al. (2009). Strain gauge readings from the IB and TB were converted to the specimen stress-strain response using the SHPB equations (Gama et al. 2004).

3.3 Numerical simulation of SHPB tests using LS DYNA

A coupled FEM-DEM simulation was carried out using the Finite Element Package LSDYNA which recently introduced a new DEM feature. The IB, TB and steel confining tube were modelled using FEM as Lagrangian eight-noded fully-integrated solid elements while the sand specimen was modelled as discrete particles. A biased mesh as shown in Figs. 3.1(a) and 1(b) was used for the simulation with higher mesh density at the specimen interface. The IB, TB and confining tube were modelled as elastic material with steel property (E =200 GPa, Poisson ratio ν = 0.33 and density ρ =8100 kg/m3). A sample specimen generated using DEM is shown in Fig. 3.1(c).

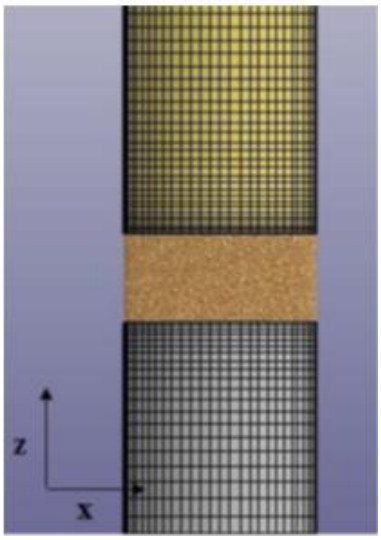

(a)

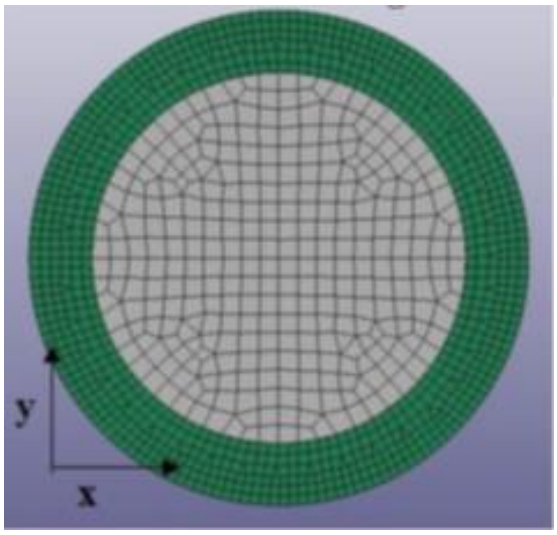

(b)

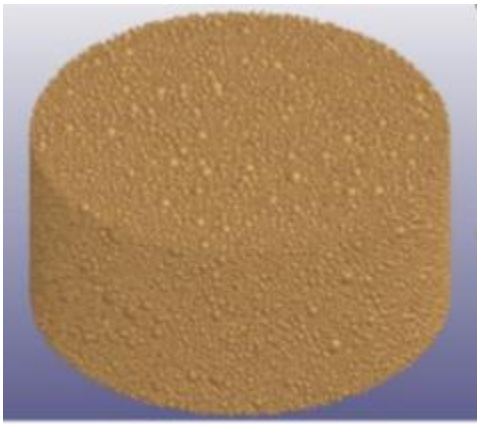

(c)

Fig. 3.1. FE mesh and DEM specimen used for the simulation: (a) plan view; (b) cross section view; (c) specimen in LS DYNA with original PSD

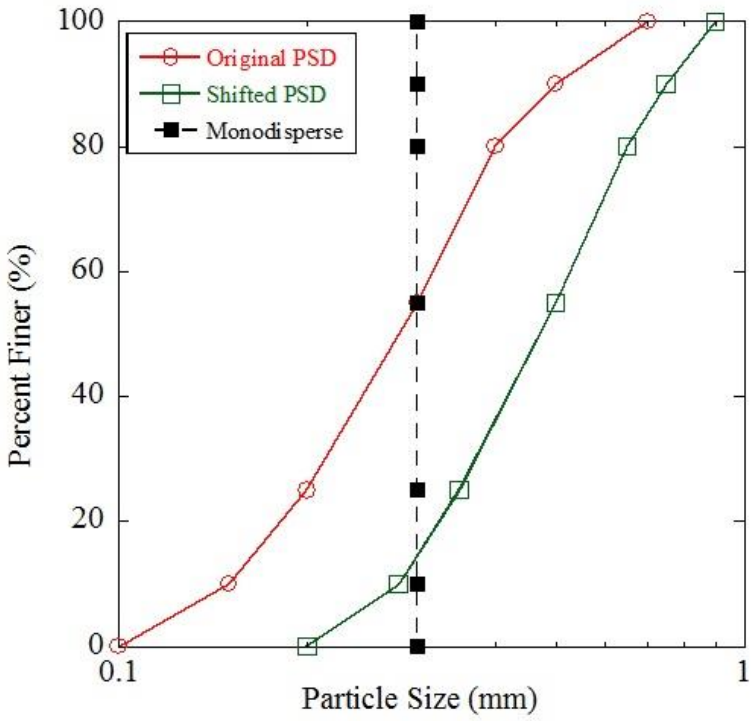

Fig. 3.2. Different Particle Size Distribution considered in the numerical simulation

Three different PSDs (Fig. 3.2) were used for the preparation of the specimen. The first was a set of spheres that constituted the original PSD of sand, second where the sphere sizes from the original PSD were increased 1.5 times, and third being a set of monodisperse particles with a radius of 0.15 mm (approximate D_{50} of the original PSD). An inbuilt packing algorithm is used by LS-DYNA to pack the spheres with a porosity of ~ 0.465. This was slightly higher than the experimental porosity of 0.45 reported by Song et al. (2009) and thus, the numerical simulation results might slightly deviate from the experimental results. However, it should be noted that the focus of the paper is to study the effect of PSD without changing the particle properties. The corresponding number of particles used in the simulation is shown in Table 3.1.

Table 3.1. Number of particles in the specimen (9.3 mm length, 9.55 mm diameter) for different PSD

Particle Size Distribution	Number of Particles in coupled simulation
Original PSD	138,275
Shifted PSD	53,602
Uniform Particle	100,451

The DEM in LS-DYNA is based on the method developed by Cundall and Stack (1979) and has been widely used. Kudraystev and Sapozhnikov (2016) used this coupled FEM-DEM approach to simulate the ceramic target subjected to ballistic impact and showed that the coupled FEM-DEM simulation could accurately replicate the experimental results. Recently, Flores-Johnson et al. (2015) used the coupled approach to study the dynamic behavior of partially saturated sand by validating the numerical model with the experiments. DEM is an explicit method and the translational and rotational velocity at each time ($t + \Delta t$) is calculated using the velocities at the previous time (t) and solving the Newtons law of motion. Particles are modelled as spheres of different sizes which represent the individual particles in the specimen. The interaction between the spheres as well as between the spheres and the FEM solids are governed by the contact law of the spheres (e.g., Linear and Hertz-Mindlin). Studies have shown that a linear model, with certain assumptions was able to duplicate the sand behavior with reasonable accuracy and could significantly reduce the computational cost of the simulation (Kermani et al. 2015, Yan and Dong 2011). Thus, the DEM option with linear contact model was used in this paper. For a linear model, the contact stiffness (K_n) between two spherical particles are given by Eq. 3.1.

$$K_n = \frac{k_1 r_1 \; k_2 r_2}{k_1 r_1 + k_2 r_2} \; NORMK \tag{3.1}$$

where k_i and r_i are the respective stiffness and radii of the i th ball and *NORMK* is the stiffness penalty parameter. The spheres are considered to be perfectly elastic and infinitely strong with a user defined Youngs modulus (E) and Poisson's ratio (ν) and k_i is calculated for each sphere ($k_i = E_i / (1 - 2\nu_i)$) from this input. The tangential spring constant K_s was given by Eq. 3.2 (Karajan et al. 2014) where *SHEARK* is a penalty parameter for the shear stiffness.

$$K_s = K_n \, SHEARK \tag{3.2}$$

One of the shortcomings with the linear model was that it did not consider the hysteretic damping that was observed in sands and thus, a viscous damping needs to be introduced using a factor NDAMP. The detailed description of this model is presented in Flores-Johnson et al. (2016). The frictional force between the particles (F_{tr}) was based on the Coulomb's law of friction and is given by Eq. 3.3.

$$F_{tr} = fric \, F_N \tag{3.3}$$

where F_N is the normal force, *fric* is the friction between the spherical particles in the DEM. The real sand particles being non-spherical provide considerably more resistance to rotation compared to spherical particles. To account for this, the user can apply a resisting moment M_r (Eq. 3.4) to the particles that inhibits rolling of the spheres. In all the simulations an ideal situation is considered where the interfaces (IB-specimen, specimen-TB and specimen-Tube) are assumed to be frictionless unless mentioned otherwise.

$$M_r = fricr \, F_N \tag{3.4}$$

where $fricr$ is a rolling friction parameter. McDowell (2002) noted that particle breakage in sand, irrespective of their particle size or distribution, occurred at stress range of 10 - 15 MPa. However, the DEM model in LS-DYNA is still under development and cannot consider the particle breakage. Hence the stress-strain response of sand in all the simulations was terminated at a stress of 13 MPa. Below this stress, the strains on the specimen were due to the rearrangement of particles.

3.4 Results

The incident stress was applied at the end of the incident bar and the reflected and transmitted stresses were recorded and these were used to obtain the stress-strain response of the specimen. Initially, specimen with original PSD was considered in the numerical simulation. Most of the input parameters for the specimen were obtained from previous studies while factor $NORMK$ was back calculated by comparing the experimental and numerical stress-strain responses. For the back calculation, the parameters were iterated until a good match was observed between the slopes of the experimental and numerical stress-strain responses. Kabir et al. (2010) observed that the porosity of the specimen (or bulk density) governed the stress-strain response at high strain rates and all the simulations were carried out at same porosity. As the initial porosity of the sample in the experiment ($n_o = 0.45$) was slightly different from the samples in the numerical simulation ($n_o = 0.465$), only the slopes of the stress-strain responses were compared. The calibrated parameters used in the numerical simulation for the dry sand are shown in Table 3.2. The

corresponding stress-strain responses obtained from the simulation and experiments carried out by Song et al. (2009) are shown in Fig. 3.3. It can be observed from Fig. 3.3 that the slopes of the stress-strain curve predicted using the FEM-DEM coupled numerical model (from strain 2% - 6%) was similar to that reported in the experiment (strain range 0- 6%). Slope of the experimental stress-strain curve was calculated to be 230 MPa while the slope of the numerical stress-strain curve with original PSD was observed to be 235 MPa. The initial deviation of the numerical stress-strain curve from the experimental curve can be attributed to the change in porosity of samples and thus, the slopes are compared at different strain ranges.

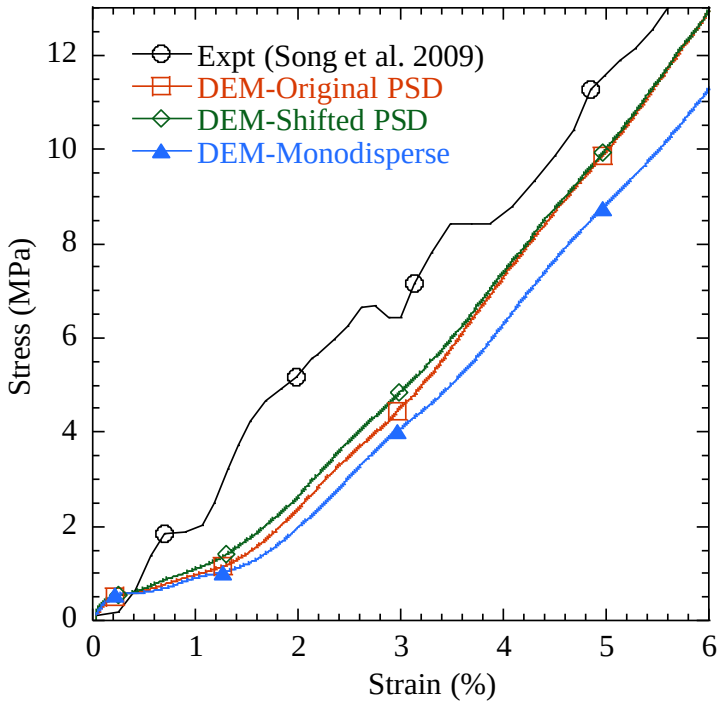

Fig. 3.3 Experimental and Numerical stress-strain response of dry sand at high strain rate

Table 3.2. DEM particle parameters

Parameter	Value	Reference
E	70 MPa	Flores-Johnson et al. (2015)
ν	0.2	Flores-Johnson et al. (2015)
$SHEARK$	1	Wang and Leung (2008)
$NORMK$	0.07	Back Calculation
$fric$	0.56	Henrych (1979)
$fricr$	0.1	Flores-Johnson et al. (2015)
$NDAMP$	0.1	Kermani et al. (2015)
$TDAMP$	0.1	

The calibrated parameters shown in Table 3.2 are used for all the subsequent simulations. In the second simulation, the number of particles was reduced to almost one third of the initial PSD. However, it should also be noted that the maximum particle size (0.9 mm) used in the specimen was less than $1/10^{th}$ of the least specimen dimension (9.3 mm) which was an essential criterion during the specimen generation in laboratory experiments. The stress-strain response obtained for the sample is shown in Fig. 3.3. It is worth noting that the stress-strain response was similar to that obtained for the initial analysis using original PSD and the slope of the stress-strain curve was similar to the experimental results.

In the third analysis, the specimen in the numerical simulation was prepared using monodisperse spheres of 0.15 mm (approximate D_{50} of the original PSD) and the specimen

comprised of 100,451 uniform spheres. The same input was applied at the end of the incident bar and the stress-strain response obtained for the specimen is shown in Fig. 3.3. A softer stress-strain response was observed for polydisperse specimen compared to the specimens with other PSDs. The slope of the stress-strain curve for polydisperse spheres was 205 MPa (strains 2%- 6%) which was softer compared to the other PSDs. It can be concluded that for the same porosity of the specimens, the shifted PSD could capture similar stress-strain behavior as the original PSD with lesser number of particles. However, polydisperse specimen with similar porosity was unable to capture similar behavior as the response was much softer which was in accordance with the quasi-static results obtained by Sullivan (2011).

3.4.1 Effect of PSD on stress equilibrium

The equations of SHPB are only valid when the stress experienced by the specimen at both ends are equal and this is known as the stress equilibrium or stress uniformity. To satisfy equilibrium condition in a soft specimen, Gray (2000) suggested the optimum specimen aspect ratio for a soft specimen to be in the range of ~ 0.5 which was similar to the specimen used by Song et al. (2009). It was observed from the previous study that the PSD with larger particles were able to replicate the behavior that is shown by the original PSD. However, the simulations were valid only if the condition of stress equilibrium was satisfied by the specimen. The stresses at the IB-specimen and TB-specimen interfaces were compared for the specimen with shifted PSD and is shown in Fig. 3.4. The stresses are compared up to 13 MPa, and it can be observed that after a certain initial time (ringing

time), the specimen deformed under stress equilibrium and the stress-strain results were valid for the particular PSD. Thus, from Figs. 3.3 and 3.4 it can be concluded that the modified PSD with lesser number of particles and contacts could effectively reproduce the material response of the original PSD.

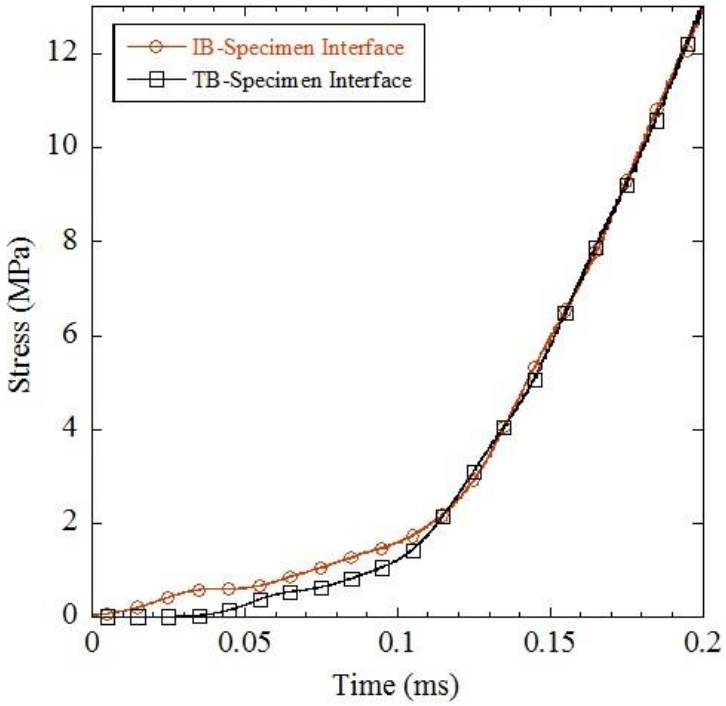

Fig. 3.4. Interfaces stresses when the incident wave impacts the specimen

3.4.2 Effect of Interface Friction on Stress-Strain Response

One of the initial studies on SHPB by Davis and Hunter (1964) has shown that the interface friction generally increases the stress-strain response of the specimen masking the actual stress-strain response of the material. In all the simulations considered above, an

ideal condition was assumed where all the interfaces i.e. the IB-specimen, TB-specimen and specimen-tube were considered to be frictionless. To understand the effect of interface friction, a comparison was done between the stress-strain response of dry sand obtained using frictionless interfaces and interfaces with maximum friction. Butterfield and Andrawes (1972) determined the maximum friction between steel and quartz to be 0.3. In this session, a numerical simulation was carried out on original PSD with interface friction and the stress-strain response was compared with the ideal case as shown in Fig. 3.5. It can be observed that the interface friction hardens the stress-strain response which was in accordance with the observation made by Meng and Li (2013).

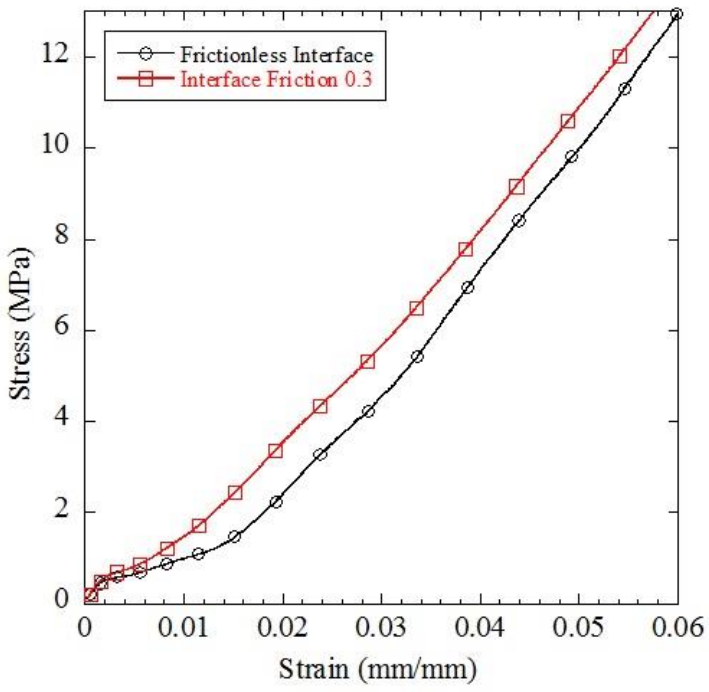

Fig. 3.5. Stress-strain response of dry sand with and without interface friction

3.5 Conclusion

In this paper, the effect of particle size distribution on the high strain rate (~470/s) response of sand was studied using coupled FEM-DEM simulation in LS DYNA and comparing the results with the stress-strain response experimentally obtained by Song et al. (2009). Three different PSDs were considered with two polydisperse assemblies and one monodisperse assembly. The basic objective of this study was to reduce the number of particles and contacts in the DEM simulation without compromising the accuracy of the material response. The parameters for the DEM were calibrated using studies by previous researchers as well as simple back calculation comparing the numerical results with the experimental results. It was observed from the simulation that increasing the particle sizes while keeping the same back bone PSD curve could reproduce the material response accurately. However, with the same parameters, the response of monodisperse particles was softer than the polydisperse particles. Thus, while using the monodisperse particles, the user should calibrate the parameters using experimental results and these parameters would be different for polydisperse DEM particles. In the subsequent study, it was also noted that for specimen with modified PSD and lesser number of particles, after an initial 'ringing up' phase, the specimen deformed under stress equilibrium and the results were valid for the SHPB simulation carried out. It was also noted that the interface friction between the DEM and FEM components stiffens the stress-strain response which was similar to that observed in the experiments as well as the continuum modelling.

Reference

Butterfield, R. and Andrawes, K. Z. (1972). “On the angel of friction between sand and plane surfaces”. *Journal of Terramechanics*. 8(4): 15 – 23.

Cundall, P. A. and Strack, O. D. L. (1979). “A discrete numerical model for granular assemblies.” *Geotechnique.* 29(1): 47– 65.

Davies, E. D. H. and Hunter, S. C. (1963). “The dynamic compression testing of solids by the method of the split hopkinson pressure bar.” *Journal of Mechanics and Physics of Solids*. 11: 155-179.

Felice, C.W, Gaffney, E. S. and Brown, J. A. (1987). “Dynamic high stress experiments on soil.” *Geotechnical Testing Journal*. 10(4): 192- 202.

Flores-Johnson, E.A., Wang, S., Maggi, F., El Zein, A., Gan, Y., Nguyen, G.D. and Shen, L.M. (2016) “Discrete element simulation of dynamic behavior of partially saturated sand.” *International Journal of Mechanical Matter Design*. 12: 495– 507.

Gama, B.A., Lopatnikov, S.L., and Gillespie, J.W. (2004). “Hopkinson bar experimental technique: a critical review.” *Applied Mechanics.* 57(4): 223–250

Gray, G.T. (2000). “Classic split-Hopkinson pressure bar testing.” ASM handbook, volume 8. *Mechanical testing and evaluation*. Ohio: ASM International: Materials Park; 462–476.

Henrych, J. (1979). “the dynamics of explosion and its use.” Elsevier, Amsterdam, the Netherlands.

Huang, X., Hanley, K., O’Sullivan, C. and Kwok, C.Y. (2014). “Effect of sample size on the response of DEM samples with a realistic grading.” *Particuology*. 15: 107–115.

Kabir, M. E., Song, B., Martin, B. E. and Chen, W. (2010). Compressive behavior of fine sand. SANDIA report, Terminal Ballistics Technology Department, Sandia Laboratories; New Mexico.

Karajan, N., Han, Z., Teng, H. and Wang, J. (2014). "On the parameter estimation for the discrete-element method in LS-DYNA." *13th International LS-DYNA Conference*. Detroit.

Kolsky, H. (1949). "An investigation of the mechanical properties of materials at very high rates of loading." *Proceedings Royal Society London*, B. 62: 676–700

Kudryavtsev, O.A. and Sapozhnikov, S.B. (2016). "Numerical simulations of ceramic target subjected to ballistic impact using combined DEM/FEM approach." *International Journal of Mechanics*, 114: 60–70.

Kuhn, M. R. and Bagi, K. (2009). "Specimen size effect in discrete element simulations of granular assemblies." *Journal of Engineering Mechanics*, 135(6), 485–492

McDowell, G. R. (2002). "On the yielding and plastic compression of sand." *Soils and Foundations.* 42(1): 139–145.

McDowell, G. R., and De Bono, J. P. (2013). "On the micro mechanics of one-dimensional normal compression." *Geotechnique*. 63: 895–908.

Meng, H. and Li, Q. M. (2003). "Correlation between the accuracy of a SHPB test and the stress uniformity based on numerical experiments." *Int J Impact Eng.* 28:537–555.

O'Sullivan, C. (2011). "Particulate discrete element modelling: A geomechanics perspective (1st ed.)." Oxford: Taylor & Francis.

Powrie, W., Ni, Q., Harkness, R. M. and Zhang, X. (2005). "Numerical modelling of plane strain tests on sands using a particulate approach." *Geotechnique*. 55(4): 297–306.

Song, B., Chen, W. and Luk, V. (2009). “Impact compressive response of dry sand.” *Mechanics of Materials*. 41 (6): 777-785

Wang, Y.H. and Leung, S.C. (2008). “Characterization of cemented sand by experimental and numerical investigations.” *Journal of Geotechnical and Geoenvironmental Engineering*. 134(7): 992–1004.

Yan, W. M. and Dong, J. J. (2011). “Effect of particle grading on the response of an idealized granular assemblage.” *International Journal of Geomechanics*. 11(4): 276–285.

CHAPTER 4

SIMULATION OF SPLIT HOPKINSON PRESSURE BAR TESTS ON SANDS USING THE DISCRETE ELEMENT METHOD

This chapter is submitted as: Prabhu, S.S. and Qiu, T. (2012). "Simulation Of Split Hopkinson Pressure Bar Tests On Sands Using The Discrete Element Method." *International Journal of Geomechanics*, and is currently under review.

Keywords: Discrete Element Modelling; Split Hopkinson Pressure Bar; High Strain Rate; Dynamic Loading

Abstract

Split Hopkinson Pressure Bar (SHPB) tests have been used extensively to study the dynamic sand response. However, the low impedance of sand leads to specimen taking longer to attain stress equilibrium and therefore, the reported results from the SHPB tests, assuming stress equilibrium, might be invalid at low stresses. Discrete element modelling is used to model SHPB test on dry sand and the stress-strain response in low stress regime are compared. The stress equilibrium in the DEM specimen at low stresses is discussed by

calculating the stress non-uniformity coefficient. The calibrated DEM model is subsequently used to study the effect of rotational resistance on the calculated stress-strain response and the stress non-uniformity coefficient. The methodology used in this paper replicates the actual laboratory SHPB test and replicates the dynamic response of dry sand reported in literature. Although, the specimens do not achieve stress equilibrium at low stresses, the reported and actual specimen responses are within the error bar reported from the laboratory experiments.

4.1 Introduction

Sand is subjected to varying strain rates in the field, ranging from quasi-static to dynamic impact conditions. The mechanical behavior of sand under low strain rates has been extensively studied in geotechnical engineering; however, its mechanical behavior under high strain rates is reported to a much lesser extent. Split Hopkinson Pressure Bar (SHPB) device has been used to understand the dynamic sand response for strain rates of 100 – 2000/s (Semblat et al. 1999; Lu et al. 2009). The stress-strain response reported in an SHPB test is valid only if stress equilibrium condition is satisfied in the test (Omidvar et al., 2012; Chen et al., 2003; Yang and Shim, 2005; Song et al. 2006). However, Gray (2000) and Luo et al. (2014) noted that such condition is satisfied only at high stresses for low-impedance materials (e.g., sand and rubber), thus seriously questioning the dynamic sand response reported in SHPB tests under low stresses. Therefore, the validity of the stress equilibrium assumption and reported dynamic response of sands in SHPB tests, particularly under low stresses, need to be studied further.

Stress equilibrium in an SHPB test is achieved by stress reverberations inside the specimen between the incident and transmission bars, causing the stress gradients to diminish at the specimen ends. However, soft specimens undergo large strains during the initial stress reverberations before achieving stress equilibrium (Song et al. 2006), making large portions of the reported stress-strain response invalid. Experiments by Song et al. (2006) on low-impedance epoxy foam showed that even shaped pulses might not satisfy the stress equilibrium condition in the specimen. Generally, the three-wave method is used to check the stress equilibrium validity where the incident, reflected, and transmitted stresses are compared (Felice 1985; Felice et al. 1987; Semblat et al. 1999; Song et al. 2009; Luo et al. 2011; Luo et al. 2014; Wang et al. 2018). However, Song and Chen (2004) noted that the three-wave method is inaccurate for SHPB tests on low-impedance specimens.

Discrete element method (DEM) is an effective tool capable of capturing sand response in quasi-static loading regimes (Sullivan and Cui 2009; Teufelsbauer et al. 2011). However, studies on the effectiveness of DEM in the dynamic strain rate regime are limited and no attempt has been made in the literature to model SHPB tests using DEM. In this paper, the laboratory SHPB tests reported by Song et al. (2009) are simulated using DEM. The dynamic sand response obtained from the DEM simulations is compared with the reported laboratory test results under low stresses. Studies (Huang et al. 2013 and 2014) have shown that particle breakage is insignificant at low stresses (<10 MPa); therefore, particle breakage is not modelled in this paper. The calibrated numerical model is then used to discuss the validity of stress equilibrium assumption at low stresses. A parametric study is

also carried out to understand the necessity of calibrating the rotational resistance applied on the DEM spheres to account for the effect of particle shape.

4.2 Experimental Studies by Song et al. (2009)

Song et al. (2009) carried out SPHB tests on poorly graded dry silica sand. The sand specimens were prepared in a steel confining tube with a length of 9.3 mm and a diameter of 19.1 mm, resulting in an aspect ratio of 0.48. Detailed physical properties of the sand are reported in Martin (2007) and Kabir et al. (2010). The sand specimens had a porosity of 0.45. The SHPB device consisted of an incident bar (IB) and a transmission bar (TB) made of steel. The diameter of both bars was 19.1 mm, and length of IB and TB was 4100 mm and 2440 mm, respectively. Song et al. (2009) reported that the specimen achieved stress equilibrium condition, therefore, the strains measured using the strain gauges on the IB and TB were converted into stress-strain response using the classic SHPB equations:

$$\varepsilon(t) = -2\frac{c_o}{L_s}\int_0^t \varepsilon_r(t)\ dt \tag{4.1}$$

$$\sigma_t(t) = \frac{A_o}{A_s}E_o\varepsilon_r(t) = E_o\varepsilon_r(t) \tag{4.2}$$

where $\varepsilon(t)$ is the strain in the specimen, c_o is the wave velocity in the IB and TB, L_s is the length of the specimen, $\varepsilon_r(t)$ is the reflected stress wave, $\varepsilon_t(t)$ is the transmitted stress wave, E_o is the elastic modulus of the IB and TB, $\sigma_t(t)$ is the transmission bar stress, A_o is the area of the incident/transmission bar, and A_s is the area of the specimen. Martin (2007) pointed out that application of lubricants at interfaces might alter the porosity of specimens; therefore, Song et al. (2009) carried out the experiments without lubricating the interfaces. Fig. 4.1 shows the incident stress wave.

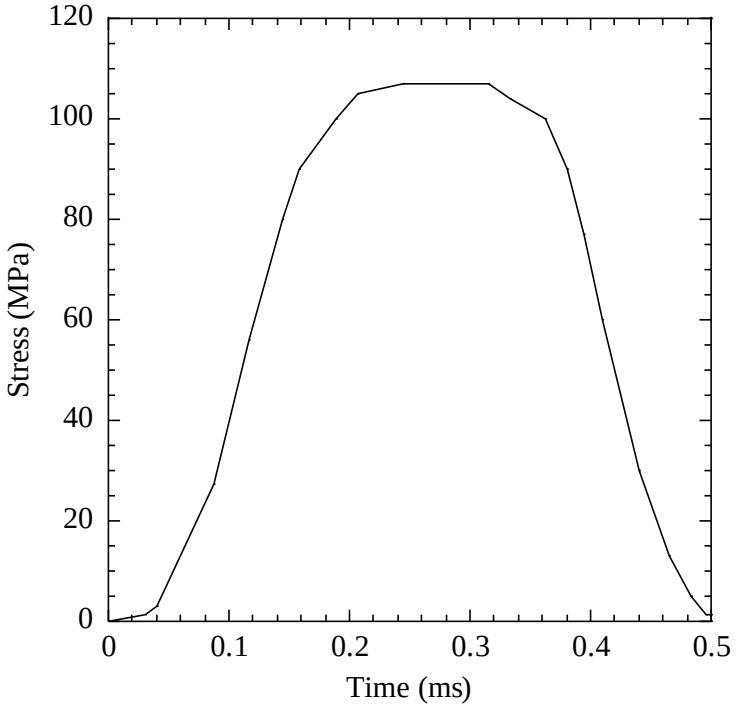

Fig. 4.1. Incident stress pulse used by Song et al. (2009) (data digitized from Song et al. 2009)

4.3 DEM Modeling of SHPB test

In the present study, commercial package *PFC3D* 5.0 is used to model the SHPB tests on dry sand reported by Song et al. (2009). The IB and TB metal bars are modeled as a set of spheres aligned in a line representing a cylindrical steel metal bar. Properties of the spheres are calculated to replicate the wave propagation in the steel bar (Itasca 2016). Each sphere in this set represents an equivalent cylindrical bar of radius R and height $2R$. The number of balls representing the IB (N_I) and TB (N_T) are obtained using the following equations

$$N_I = \frac{L_I}{2R} \tag{4.3}$$

$$N_T = \frac{L_T}{2R} \tag{4.4}$$

where L_I and L_T are the IB and TB bar lengths, respectively. Linear contact model is used for these spheres and for the continuum bar, the Youngs modulus (E) can be calculated as

$$E = \frac{\sigma}{\varepsilon} = \frac{F/\pi R^2}{u/2R} \tag{4.5}$$

where σ and ε are applied stress and strain, F and u are contact force and displacement. At a contact

$$F/u = k_n^{ball}/2 \tag{4.6}$$

Substituting Eq. (6) into Eq. (5) yields

$$E = k_n^{ball}/\pi R \tag{4.7}$$

The stress wave propagation through a medium is governed by the mass density of the particle; therefore, mass conservation is used to obtain the density of spheres in the IB and TB

$$4\pi R^3/3 \times \rho_{ball} = 2\pi R^3 \times \rho_{bar} \tag{4.8}$$

The longitudinal wave velocity in a bar is given by $c_{bar} = \sqrt{E/\rho_{bar}}$, which can be substituted into Eq. (7) and yields

$$k_n^{ball} = \pi R \rho_{bar} c_{bar}^2 \tag{4.9}$$

For a longitudinal stress wave passing through a metal bar, the stress magnitude is provided by

$$\sigma = \rho_{bar} c_{bar} \dot{u} \tag{4.10}$$

The IB-specimen, TB-specimen, and specimen-confining tube interfaces are modeled using wall elements in *PFC3D* 5.0. Input stress wave (Fig. 4.1) is applied as a time-varying stress pulse at the 'free end' of the IB, away from the specimen. The generated stress wave propagates through the spheres representing the IB and reaches the IB-specimen interface. The IB-specimen interface is moved using a servo control mechanism. A part of the incident pulse is reflected and a part is transmitted into the specimen at the IB-specimen interface. The sand specimen is modeled using discrete spheres with each sphere representing a single sand grain. As the stress wave propagates in the specimen and reaches the TB-specimen interface, a similar servo control mechanism is used to control the movement of the TB-specimen interface. The wave velocity in the IB and TB is converted into stresses using Eq. (4.10) and stress-strain response of the specimen is derived using Eqs. (4.1) and (4.2). Fig. 4.2 shows the SHPB test setup generated in *PFC3D* 5.0.

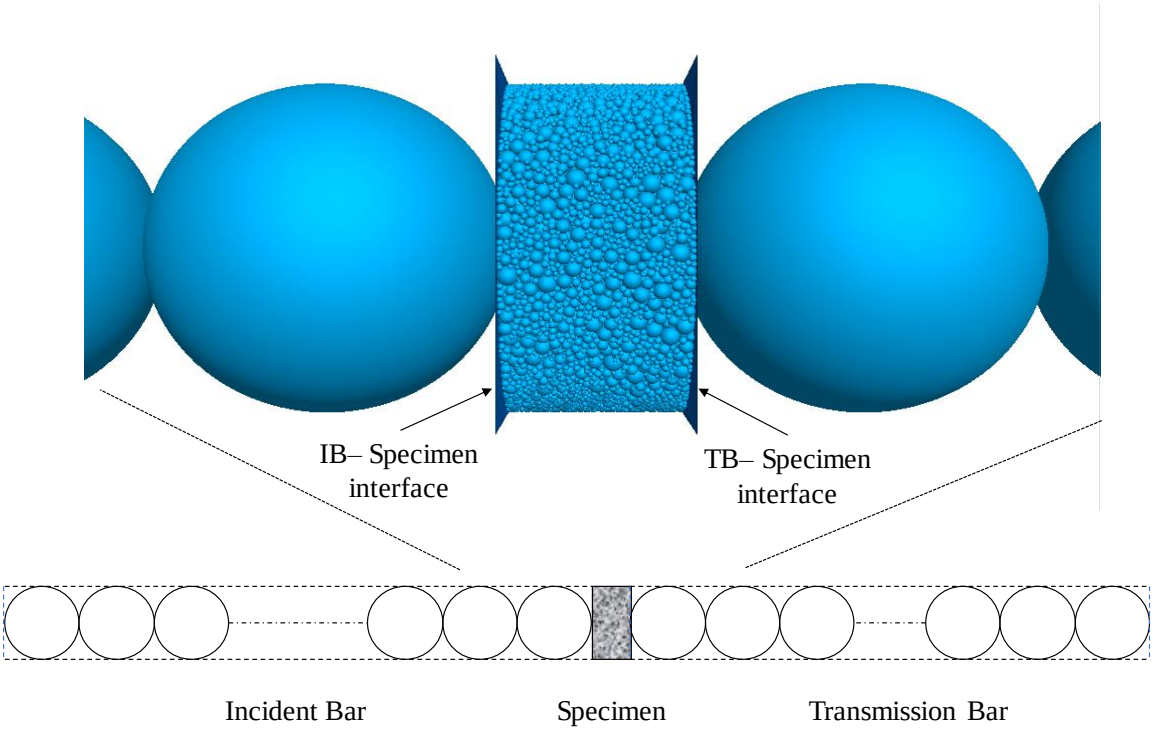

Fig. 4.2. Images of the DEM specimen, IB and TB used in the current study (not to scale)

The DEM specimen is prepared at a porosity of 0.44 with the same dimensions as that used by Song et al. (2009). Prabhu and Qiu (2019) noted that proportional particle size upscaling, i.e., increasing the particle sizes in the DEM specimen proportionally, reduces the computation cost without compromising the granular behavior during dynamic loading. Therefore, the particle upscaling procedure is adopted in this paper. Fig. 4.3 shows the original particle size distribution (PSD) from Song et al. (2009) and the scaled PSD used in this study. For the PSD and porosity considered, the specimen consists of 34,411 DEM particles.

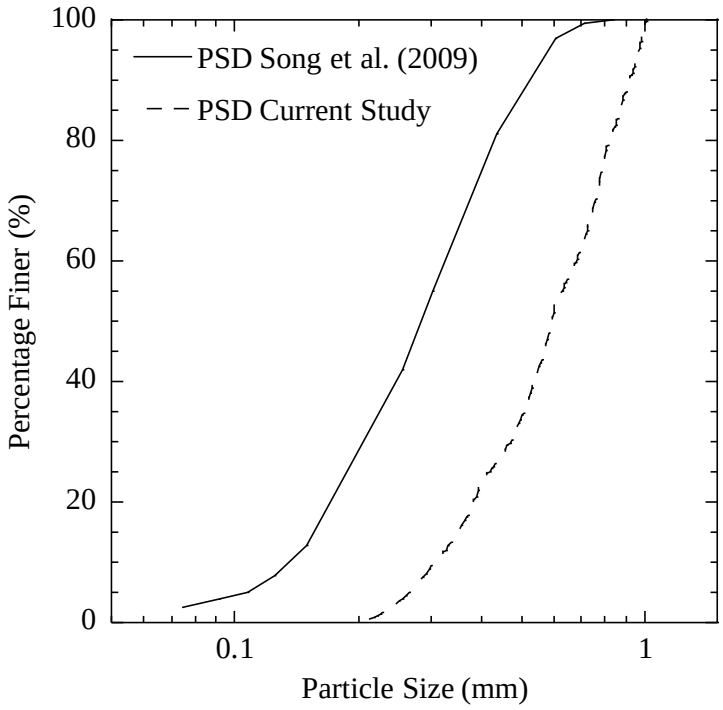

Fig. 4.3. Particle size distributions of Silica sand used by Song et al. (2009) and current study

The interaction between the interface walls and specimen is modelled using linear contact model. The interaction between sand particles in DEM is captured using non-linear Hertz-Mindlin contact model, which has been extensively used to capture the actual sand response (e.g., Bono and McDowell 2014; Huang et al. 2014). In the Hertz-Mindlin model, the normal stiffness (k_n^H) and tangential stiffness (k_s^H) vary with overlap as (Mindlin 1949)

$$k_n^H = \left(\frac{2G\sqrt{2\bar{R}}}{3(1-\upsilon)}\right)\sqrt{U} \tag{4.10}$$

$$k_S^H = \left(\frac{2G\sqrt{2\bar{R}}}{3(1-\upsilon)}\right)\sqrt{U^n} \tag{4.11}$$

where U is particle-particle overlap, n is the power exponent (typically 0.5), G is the shear modulus of sphere, υ is the poisons ratio, and $\bar{R}$ is the effective radius between two spheres in contact. Material properties reported by Song et al. (2009) and corresponding DEM properties are shown in Table 4.1.

Table 4.1. Properties used in experiments (Song et al. 2009) and DEM simulations

Property	Value
N_I	216
N_T	108
E	200 GPa
ρ_{bar}	8.1×10^3 kg/m^3
c_{bar}	4959 m/s
R	0.00955 m
IB and TB ball: k_n^{ball}	6×10^9 N/m
ρ_{ball}	1.251×10^3 kg/m^3
G	30 GPa (Yimsiri and Soga 2010)
υ	0.3
Ball-ball friction	0.5
Ball-interface friction	0.3 (rough: Frost et al. 2002)
Wall-specimen interface: k_n	2.6×10^6 N/m
Wall-specimen interface: k_s	1.6×10^6 N/m

The silica sand particles used by Song et al. (2009) in their SHPB tests are sub-angular. Several studies used clump particles to capture the angularity of sand in DEM. However, it is computationally expensive to model angular particles in DEM; therefore, the sand particles in this study are modeled as spheres with additional rotational resistance to account for the effect of particle shape. Calvetti et al. (2002) introduced a pseudo rotational resistance to individual DEM particles and the magnitude the pseudo rotational resistance was kept constant throughout the simulation. This method has been observed to be computationally efficient and produce reliable results (Ai et al. 2011; Teufelsbauer et al. 2009; Kermani et al. 2015). In the present study, this method is implemented to impart the additional rotational resistance and the methodology is illustrated below.

The angular velocity at a particular time (ω_i^{t+1}) is obtained by reducing the angular velocity from the previous time step (ω_i^{t}) as (Teufelsbauer et al. 2009)

$$\omega_i^{t+1} = k_\lambda^{\xi}\, \omega_i^{t} \tag{4.12}$$

$$k_\lambda = \frac{1}{1+c^n} \tag{4.13}$$

$$\xi = \Delta t/\lambda \tag{4.14}$$

where k_λ^{ξ} is the rotational resistance, k_λ is a retarding coefficient, ξ is time discretized retarding time, c is the mean number of contacts around a particle, λ is the retarding time, Δt is the timestep used in the DEM simulation, n is a sensitivity parameter, and $I = x$, y and z directions. Teufelsbauer et al. (2009) reported the value of n to be in the range of 0.5 to 1 while λ to be 0.01 s. Bolton et al. (2008) noted that for an applied stress range of 0 – 10 MPa, the average number of contacts (c) on particles ranged from 6 to 10. The time step used in the simulations was calculated to be 10^{-9} s/step. From Eqs. (4.13) and (4.14), the value of k_λ^{ξ} is calculated to be between 0.9999995 to 0.999999 for the range of c values considered. Therefore, an average value of 0.99999975 is used for k_λ^{ξ} throughout the simulations unless specified otherwise.

4.4 Results and Discussion

4.4.1 Model Validation and Stress Equilibrium

The SHPB tests conducted by Song et al. (2009) are simulated using the DEM model. The simulated stress-strain response of dry sand is compared with the experimental response. The results are limited to the stress level of 10 MPa where the particle breakage is insignificant and the validity of the SHPB test is discussed in this section in terms of

stress equilibrium in the specimen. Fig. 4.4 shows the comparison of simulated stress-strain response from the DEM simulation using $\sigma_t(t)$ (Eqs. (4.1) and (4.2)) and the experimental stress-strain response reported by Song et al. (2009), assuming stress equilibrium. It is evident from Fig. 4.4, that the DEM model replicates the SHPB experiments accurately at low stresses (< 10 MPa) as it provides similar stress-strain response as the experiments. Initially, the confined modulus of the DEM specimen, for the stress-strain response obtained using $\sigma_t(t)$, is 220 MPa which is slightly lower than the average value of 228 MPa reported for the experiments by Song et al. (2009). The simulated response stiffens at higher stresses compared to the experimental response as the confined modulus reaches 300 MPa. This stiffening is attributed to particle arrangement and densification.

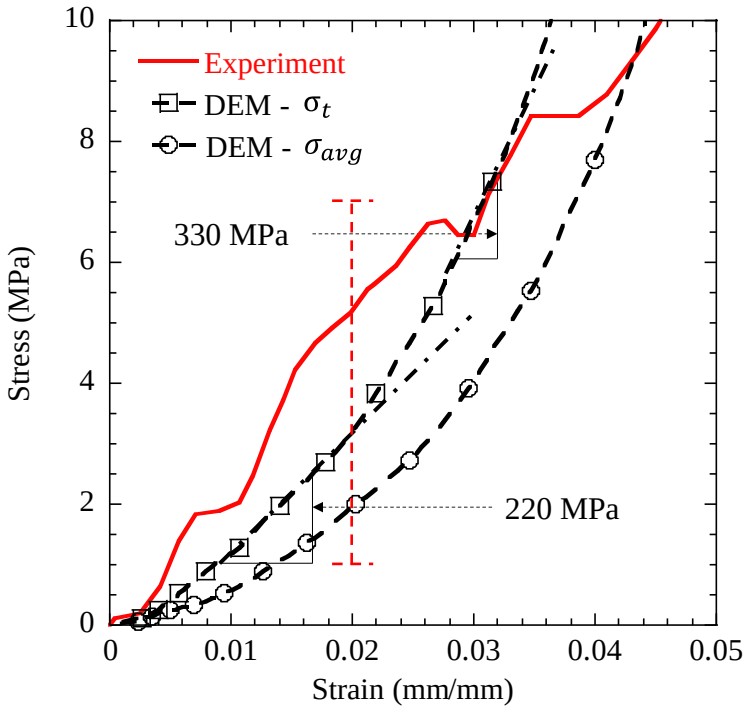

Fig. 4.4. Stress-strain response of dry sand with steel confinement reported by Song et al. (2009) and obtained from DEM simulations

Song et al. (2004) and Song and Chen (2004) used quartz crystal to measure the interface stresses, i.e., stresses at the front and back of the specimen, to observe whether the stress equilibrium condition was satisfied in the rubber specimens. Similar approach is used in the present study and the stress-equilibrium assumption is checked by comparing the IB-specimen and TB-specimen interface stresses, directly obtained in the simulations. Researchers (Ravichandran and Subhash 1993; Zencker and Clos 1999; Yang and Shim 2005; Zhu et al. 2009) proposed a non-uniformity factor, α_k, to better understand the stress equilibrium and uniformity condition in specimens during dynamic testing and α_k is defined as the absolute value of the ratio of stress difference at specimen interfaces to the average stress at the interfaces

$$\alpha_k = \left| \frac{\sigma_i(t) + \sigma_r(t) - \sigma_t(t)}{\frac{\sigma_i(t) + \sigma_r(t) + \sigma_t(t)}{2}} \right| \tag{4.15}$$

where $\sigma_i(t) + \sigma_r(t)$ is the stress at the IB-specimen interface. During SHPB experiments, the value of α_k varies between 0 and 2. A value of 0 represents perfect equilibrium while 2 represents perfect non-equilibrium. As it is nearly impossible to achieve a strict equilibrium with α_k of 0, 0.05 has been used as the limiting value (Zencker and Clos 1999; Yang and Shim 2005; Prabhu and Qiu 2020). Thus, a specimen deforming at values of α_k less than 0.05 is assumed to satisfy the stress equilibrium and the stresses along the longitudinal direction are deemed uniform.

Fig. 4.5 depicts the variation of α_k with time for the simulated SHPB test along with the particle velocity contour inside the specimen at different times. Typically, the time 0 in the *x*-axis is when the incident wave arrives at the IB-specimen interface. The variation of

α_k in Fig. 4.5 is reported until the stress at the TB-specimen interface reaches a value of 10 MPa. Fig. 4.5 shows that initially, the specimen deforms under non-equilibrium stress condition. As time progresses, the wave reverberates inside the specimen and the α_k decreases. However, even after considerable time, α_k does not reduce below the limiting value of 0.05.

The particle velocity contour inside the specimen at different time in Fig. 5.5 shows that 1) the particles close to the IB-specimen interface start to move at high velocities shortly after the incident wave arrival while the particles close to the TB-specimen interface remain stationary, 2) as the wave reverberates inside the specimen, the particle velocity gradient decreases, however, the value never reaches zero, corroborating the non-equilibrium stress condition. Song et al. (2006) also observed a similar phenomenon where a compaction stress wave was generated at the IB-specimen interface traveling to the TB-specimen interface in soft specimens.

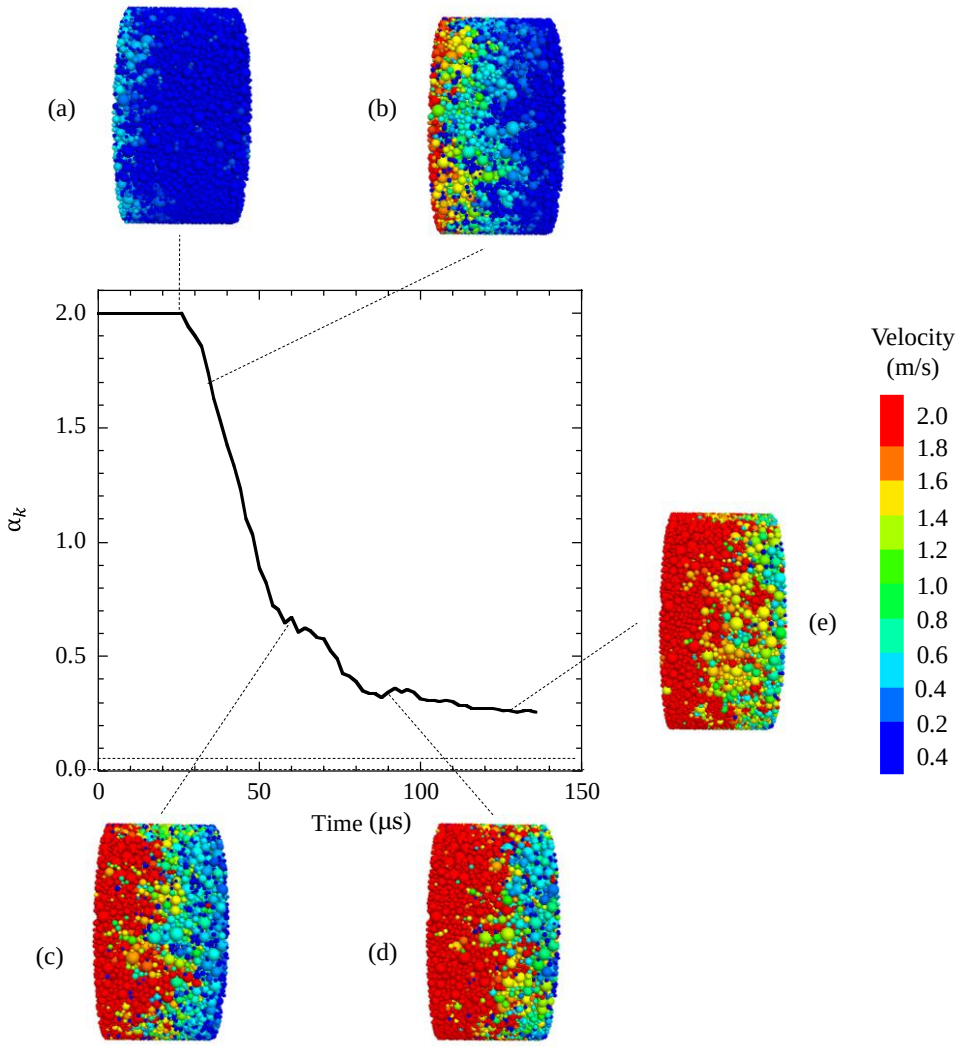

Fig. 4.5. Variation of α_k with time for simulated SHPB test and particle velocity contour inside specimen at different time: (a) 25 μs; (b) 35 μs; (c) 60 μs; (d) 90 μs; (e) 130 μs

For specimens violating the stress equilibrium condition, the actual stress-strain response can be obtained using the average stress (σ_{avg}) given by (Challita and Othman 2010; Zhu et al. 2012),

$$\sigma_{avg} = \frac{\sigma_i(t) + \sigma_r(t) + \sigma_t(t)}{2} = E_o \frac{\varepsilon_i(t) + \varepsilon_r(t) + \varepsilon_t(t)}{2} \tag{4.16}$$

In the DEM simulations, σ_{avg} is calculated as the average of IB–specimen and TB–specimen interface stresses. As noted in Fig, 4.5, the DEM specimen does not attain stress-equilibrium at low stress. Therefore, the actual stress-strain response obtained using σ_{avg} is also shown in Fig. 4.4 for comparison purpose. Fig. 4.4 shows that the stress-strain response obtained using σ_{avg} is softer compared to $\sigma_t(t)$ response. Although the stress-strain responses obtained using $\sigma_t(t)$ and σ_{avg} are both within the experimental error bar reported, Fig. 4.4 highlights the importance of achieving stress-equilibrium for deriving the actual stress-strain response form SHPB tests.

4.4.2 Effect of particle rotational resistance

A parametric study is carried out to understand the effect of particle rotational resistance on the stress-strain response and the ability of the DEM specimen to achieve stress equilibrium. For the same DEM model considered in the previous section, simulations are carried out with different k_λ^ξ values applied to the DEM spheres representing sand particles. Studies (Teufelsbauer et al. 2009; Gabrieli et al. 2009) have shown that applying additional rotational resistance to spherical DEM particles accurately captures the angular sand behavior in DEM; however, the magnitude of rotational resistance to be applied is still an ongoing debate. Some studies (Teufelsbauer et al. 2011; Kermani et al. 2015) calibrated the rotational resistance applied while others (Calvetti 2008; Calvetti et al. 2017) neglected the importance of this parameter calibration and completely restricted the particle rotation (k_λ^ξ=0) in DEM spheres. In this parametric study, DEM simulations are carried out with three additional k_λ^ξ values representing a complete

rotational restraint (k_λ^ξ=0), no rotational restraint (k_λ^ξ=1), and an intermediate rotational restraint (k_λ^ξ= 0.999). All other DEM model parameters are kept the same as those in Table 4.1. Figs. 4.6 and 4.7 show effect of the k_λ^ξ on the simulated stress-strain response and variation of α_k with time, respectively.

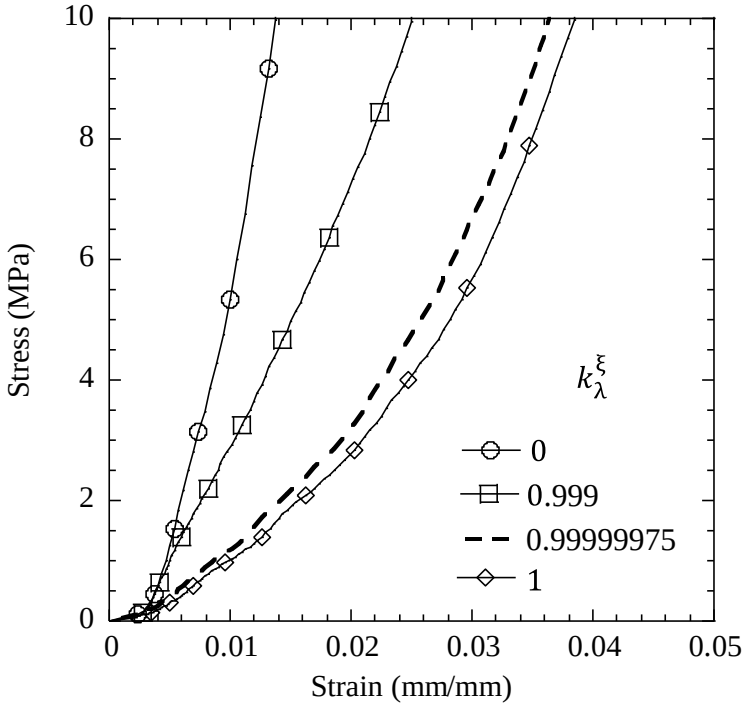

Fig. 4.6. Effect of particle rotational resistance on simulated stress-strain response

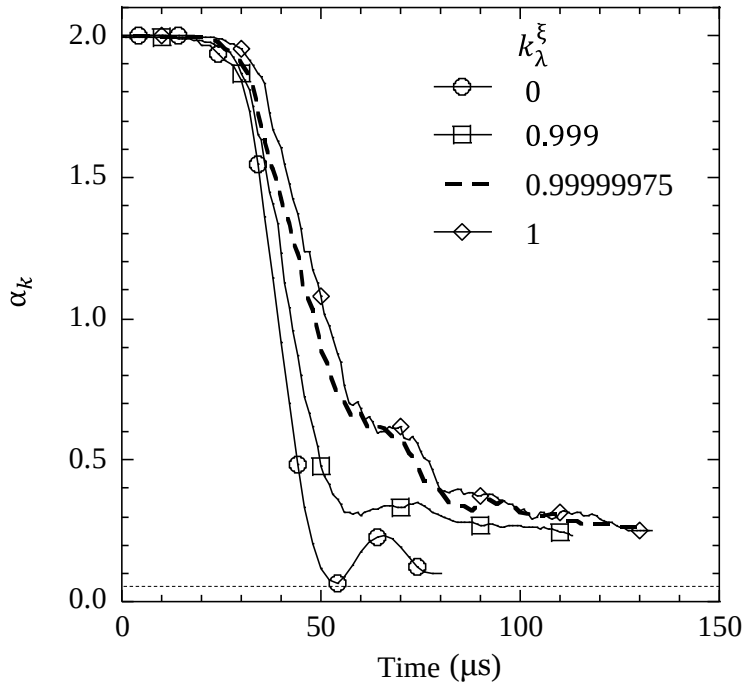

Fig. 4.7. Effect of particle rotational resistance on variation of α_k with time

It is evident from Figs. 4.6 and 4.7 that particle rotation affects the dynamic response of sand specimens in the DEM simulations. An increase in rotational resistance stiffens the mechanical response, with the complete rotational restraint resulting in the stiffest response and no rotational restraint resulting in the softest response. An increase in rotational resistance hinders the rolling but allows translation of spheres, leading to a quicker formation of force chains and a stiffer response. The value of k_λ^ξ influences the wave travel time in the specimen and the highest wave velocity is observed in specimen with complete rotational restraint (Fig. 4.7). Figs. 4.5 and 4.6 also show that the stress-strain response for the calibrated model (k_λ^ξ=0.99999975) is similar to the simulation without any rotational restraint (k_λ^ξ=1); this observation suggests that particle angularity does not significantly contribute to the sand response during SHPB tests since particle rotation is not a dominant

mode of motion during these tests. Fig. 4.7 shows that all specimens do not attain strict stress equilibrium, although the specimen with k_{λ}^{ξ}=0 comes close.

4.5 Conclusion

In this study, a method is developed in DEM to model SHPB tests on sand. Detailed procedures for calibrating the different DEM element properties are provided. The methodology is used to model the laboratory SHPB test on dry sand reported by Song et al. (2009). Computational cost is reduced by preparing DEM specimens with larger PSD. The calibrated model is further used to understand the effect of the rotational resistance magnitude on the stress-strain response and the non-uniformity coefficient variation with time. Following conclusions are obtained from the study:

1. Calibrated DEM model accurately captures the reported in the SHPB experiments at low stresses. Specimen does not attain stress equilibrium at low stresses, however, the stress-strain responses obtained using σ_T and σ_{avg} are within reported error bar in the experiment.

2. The parametric study highlights the importance of calibrating the additional rotational resistance with a higher rotational resistance magnitude stiffening the stress-strain response.

Reference

Ai, J., Chen, J.F., Rotter, J. M. and Ooi, J.Y. (2011). "Assessment of rolling resistance models in discrete element simulations." *Powder Technology*. 206(3): 269–282.

Calvetti, F., Tamagnini, C. and Viggiani, G. (2002). “On the incremental behavior of granular soils.” NUMOG VIII, G.N. Pande and S. Pietrusczczak, eds., Balkema, Lisse, The Netherlands, 3–9.

Calvetti, F. (2008). “Discrete modelling of granular materials and geotechnical problems.” *European Journal of Environmental and Civil Eng.* 12(7–8):951–965.

Calvetti, F., di Prisco, C. G. and Vairaktaris, E. (2017). “DEM assessment of impact forces of dry granular masses on rigid barriers.” *Acta Geotechnica*. 12:129–144.

Chen, W., Song, B., Frew, D.J., and Forrestal, M.J. (2003). “Dynamic small strain measurements of a metal specimen with a split Hopkinson pressure bar," *Experimental Mechanics.* 43: 20-23.

Challita, G. and Othman, R. (2010). “Finite-Element analysis of SHPB tests on double-lap adhesive joints.” *International Journal of Adhesion and Adhesive*. 30:236–44.

Ciantia, M. O., Arroyo, M., Calvetti, F., and Gens, A. (2015). “An approach to enhance efficiency of DEM modelling of soils with crushable grains.” *Géotechnique*. 65(2): 91-110.

de Bono, J.P. and McDowell, G.R. (2014). “DEM of triaxial tests on crushable sand.” *Granular Matter.* 16(4): 551–562.

Felice, C. W. (1985). “The response of soil to impulse loads using the S.H.P.B technique.” Ph.D. Thesis, Department of Civil Engineering, University of Utah, Salt Lake City.

Felice, C.W., Gaffney, E. S. and Brown, J. A. (1987). “Dynamic high stress experiments on soil.” *Geotechnical Testing Journal.* 10(4): 192-202.

Gabrieli, F., Cola, S. and Calvetti, F. (2009). "Use of an upscaled DEM model for analyzing the behavior of a shallow foundation on a model slope." *Geomechanics and Geoengineering.* 4(2): 109–122.

Gray, G. T. (2000). "Classic split-Hopkinson pressure bar testing." ASM Handbook, Vol 8, Mechanical Testing and Evaluation, H Kuhn and D Medlin eds., ASM Int Materials Park OH, 462–476.

Huang, J., S. Xu, and S. Hu. (2013). "Effects of grain size and gradation on the dynamic responses of quartz sands." *International Journal of Impact Eng*. 59:1–10.

Huang, J., Xu, S. and Hu, S. (2014). "Influence of particle breakage on the dynamic compression responses of brittle granular materials." *Mechanics of Material*. 68(1): 15-28.

Itasca (2016). "Particle flow code in three dimensions: Software manual." Minnesota, MN, USA.

Kabir, M. E., Song, B., Martin, E. and Chen. W. (2010). "Compressive behavior of fine sand." New Mexico: Terminal Ballistics Technology Dept., Sandia Laboratories.

Kermani, E., Qiu, T. and Li, T. (2015) "Simulation of collapse of granular columns using the discrete element method." *Int J Geomech*. 15(6): 04015004.

Lu, H., Luo, H. and Komoduri, R. (2009). "Dynamic compressive response of sand under confinements." Proc., SEM Annual Conf., Society for Experimental Mechanics, Albuquerque, NM, 1–7.

Luo, H., Lu, W.L. and Komanduri, R. (2011). "Effect of mass density on the compressive behavior of dry sand under confinement at high strain rates." *Experimental Mechanics*. 51(9): 1499–1510.

Luo, H., Cooper, W. L. and Lu, H. (2014). “Effects of particle size and moisture on the compressive behavior of dense eglin sand under confinement at high strain rates.” *Int. J. Impact Eng*. 65: 40–55.

Martin, B. E. (2007). “Moisture effects on the high strain rate behavior of sand.” Master of Science Thesis, Dept. of Mechanical Engineering, University of Florida.

Mindlin, R.D. (1949). “Compliance of elastic bodies in contact.” *Journal of Applied Mechanics,* ASME, 16: 259–268.

Omidvar, M., Iskander, M. and Bless, S. (2012). “Stress–strain behavior of sand at high strain rates.” *International Journal of Impact Eng*. 49:192–213.

O'Sullivan, C., and Cui, L. (2009). “Micromechanics of granular material response during load reversals: Combined DEM and experimental study.” *Powder Technology*. 193: 289–302.

Prabhu, S. and Qiu, T. (2019). “Effect of particle size on high-strain rate response of sand.” Geocongress. Geocongress Special Publication. 310: 155 – 164.

Prabhu, S. and Qiu, T. (2020). “Simulation of split hopkinson pressure bar tests on sands with low water content.” *Journal of Engineering Mechanics*. 146 (8): 04020082.

Ravichandran, G. and Subhash, G. (1993). “Critical appraisal of limiting strain rates for compression testing of ceramics in a split Hopkinson pressure bar.” *Journal of American Ceramic Society*. 77: 263-267.

Semblat, J. F., Luong, M. P., and Gary, G. (1999). “3D-Hopkinson Bar: New experiments for dynamic testing on soils.” *Soils and Foundations*. 39(1):1-10.

Song, B. and Chen. W. (2004). “Dynamic stress equilibration in split hopkinson pressure tests on soft materials.” *Exp. Mech*. 44(3): 300–312.

Song, B., Forrestal, M.J. and Chen, W. (2006). “Dynamic and quasi-static propagation of compaction waves in a low-density epoxy foam.” *Exp. Mech.* 46: 127-136.

Song, B., Chen, W., and Luk, V. (2009). “Impact compressive response of dry sand.” *Mechanics of Materials.* 41(6):777-785.

Teufelsbauer, H., Wang, Y., Chiou, M. C. and Wu, W. (2009). “Flow–obstacle interaction in rapid granular avalanches: DEM simulation and comparison with experiment.” *Granular Matter*. 11(4): 209–220.

Teufelsbauer, H., Wang, Y., Pudasaini, S.P., Borja, R.I. and Wu, W. (2011). “DEM simulation of impact force exerted by granular flow on rigid structures.” *Acta Geotechnica*. 6:119–133.

Wang, S., Shen, L., Maggi, F., El-Zein, A., Nguyen, G.D., Zheng, Y., Zhang, H. and Chen, Z. (2018). “Influence of dry density and confinement environment on the high strain rate response of partially saturated sand.” *International Journal of Impact Eng*. 116: 65-78.

Yang, L. M. and Shim, V. P. (2005). “An analysis of stress uniformity in split Hopkinson bar test specimens.” *International Journal of Impact Engineering.* 31(2): 129–150.

Yuan, P., Ma, Q. and Ma, D. (2018). “Stress uniformity analyses on nonparallel end-surface rock specimen during loading process in SHPB tests.” *Advances in Civil Engineering*. 12.

Zencker U. and Clos R. (1999). “Limiting conditions for compression testing of flat specimens in the split Hopkinson pressure bar.” *Exp. Mech.* 39: 343-348

Zhu, J., Hu, S. and Wang, L. (2009). “An analysis of stress uniformity for concrete like specimens during SHPB tests.” *Int J Impact Eng.* 36(1): 61-67.

Zhu, W., Bai, C., Y., Li, X. B. and Niu, L. L. (2012). “Numerical simulation on rock failure under combined static and dynamic loading during SHPB tests.” *Int. J. Impact Eng.* 49: 142–157.

CHAPTER 6

MODELING OF SAND PARTICLE CRUSHING IN SPLIT HOPKINSON PRESSURE BAR TESTS USING THE DISCRETE ELEMENT METHOD

This chapter is submitted as: Prabhu, S.S. and Qiu, T. (2012). "Modeling of Sand Particle Crushing in Split Hopkinson Pressure Bar Tests using the Discrete Element Method." *International Journal of Impact Engineering*, and is currently under review.

Keywords: Discrete element method; Grain size distribution; Particle breakage; Sand; Split Hopkinson pressure bar; Wave propagation

Abstract

The discrete element method (DEM) has been extensively used to study the micro-mechanical behavior of sand subjected to quasi-static strain rates. In most of these studies, the sand specimens were prepared with an upscaled particle size distribution (PSD) to reduce the computational cost. However, the effectiveness of this upscaling approach in replicating the dynamic sand response is not well understood, especially at high stresses

where significant particle breakage occurs. In this paper, several split Hopkinson pressure bar (SHPB) tests reported in literature are modeled in DEM using two methodologies: 1) applying the reported strain rates directly to the DEM specimen without accounting for wave propagation in the incident and transmission bars; and 2) modeling the complete SHPB test setup including the incident and transmission bars. The results show that with well-calibrated parameters for contact behavior and particle crushing, specimens with upscaled PSD provide similar dynamic stress-strain response and PSD evolution as those reported in literature. This study shows the importance of particle breakage in the stress-strain response under high pressures as the specimens without particle breakage provide a much stiffer response compared to the specimens with particle breakage. The developed DEM model may be a useful tool to model the complete SHPB test setup as the incident, reflected and transmitted stress waves can be accurately replicated.

5.1 Introduction

High strain-rate sand response has been widely studied in recent years to understand the dynamic behavior of sand. Studies have shown the importance of particle breakage on sand response at both quasi-static and dynamic strain rates (Mun and McCartney 2017; Xiao et al. 2019). However, particle breakage and the associated evolution of particle size distribution (PSD) of sands subjected to high strain rates are difficult to monitor and hence not well studied. Several advanced constitutive models at the continuum scale have been developed to capture the dynamic sand behavior (Barr et al. 2015; Prabhu and Qiu 2020).

However, these models could neither capture the micromechanics nor particle breakage in sand at high strain rates.

The discrete element method (DEM), first developed by Cundall and Strack (1979), has been used to understand the micromechanics of sands. Calibrated DEM models have accurately replicated sand response at quasi-static strain rates (Widulinski et al. 2009; Nguyen et al. 2018). However, the large number of particles in a real sand specimen and the lack of calibrated and validated particle breakage models have restricted the implementation of these models in dynamic studies of sand. To reduce the particles in the simulation and the computational cost, particle upscaling methodology is generally adopted to model quasi-static experiments (Ciantia et al. 2015; Roessler and Katterfeld 2018). During upscaling, the PSD is shifted to the right by an upscaling factor, N, effectively increasing the particle size and reducing the number of particles in a specimen while capturing the overall sand response accurately. Ciantia et al. (2015) carried out one dimensional compression tests in DEM with upscaled specimens and after the simulation, a downscaling procedure was adopted and the PSD was shifted to the left by the same factor, N. The study showed that the upscaling-downscaling procedure effectively reduced the number of particles in the simulation while capturing the quasi-static sand response accurately and providing comparable PSD evolution as that measured in the experiments. However, the validity of the upscaling-downscaling procedure for sands during dynamic loading is not well understood. Combined FEM-DEM simulation by Prabhu and Qiu (2019) showed that during dynamic loading of sand, upscaling is effective at low stresses where particle breakage is insignificant. However, the effectiveness of particle upscaling in dynamic problems involving particle breakage is still unknown.

Different methodologies have been adopted to implement particle breakage in DEM. In a widely used approach, individual sand grains are replaced with agglomerates made of 135 to 1477 bonded spheres (Lim and McDowell 2007; Cil and Alshibli 2012; Wang and Yan 2012). The individual bond strengths are calibrated using the experimental data from individual grain crushing tests. The method is accurate and provides reliable results in simulations; however, the methodology is unsuitable for sand specimens with large number of particles as the simulation becomes computationally expensive. In a different approach, researchers used force/stress criterion to check for particle breakage (Lobo-Guerrero and Vallejo 2005a; Ben-Nun and Einav 2008; De Bono et al. 2014, Hanley et al. 2015). Individual sand grains are modeled as spheres and particles satisfying the force/stress criterion are replaced with either a set of daughter spheres with significant particle-particle overlap (McDowell and de Bono 2013; de Bono and McDowell 2014) or without any overlap (Guerrero and Vallejo 2005a; Ciantia et al. 2019). Systems with overlapping daughter particles conserve mass of the system; however, after each particle breakage, the system needs to be equilibrated to dissipate excessive forces arising from the particle overlaps (McDowell and De Bono 2013, 2016). This method is unsuitable for dynamic simulations as the response is governed by transient response (e.g., wave propagation) and the simulation cannot be paused for re-equilibrium (e.g., SHPB test, flyer plate tests). Therefore, in this study, the second methodology is adopted and the particles satisfying the force/stress criterion are replaced by non-overlapping daughter particles. Although it does not conserve mass of the systems, this method has been observed to be effectively representative of quasi-static tests on sand (Lobo-Guerrero and Vallejo 2005a; Ciantia et al. 2015, 2019). Researchers noted that the lost mass during each particle breakage did not

contribute to the mechanical behavior significantly and, therefore, can be reasonably ignored from the simulation (Guerrero and Vallejo 2005a, b; Ciantia et al. 2019). Ciantia et al. (2014, 2015, 2019) also used similar methodology and ignored the lost mass in their simulations; however, the lost mass during each particle breakage was accounted in the PSD evolution.

Split Hopkinson Pressure Bar (SHPB) tests have been extensively used to study high strain-rate responses of different materials (Cao et al. 2018; Li et al. 2019). The SHPB test setup consists of a metal striker bar, a metal incident bar (IB), a metal transmission bar (TB), a confining tube and a specimen. The stress wave is applied to the IB from the striker bar and propagates until reaching the IB-specimen interface. Wave interaction occurs at the IB-specimen interface and a part is transmitted into the specimen and subsequently into the TB while a part is reflected back into the IB. Using the incident, reflected and transmitted stresses, the stress-strain response of the specimen can be determined using classic SHPB equations. The strain rate experienced by the specimen is determined from the reflected wave in the SHPB tests. SHPB tests have been extensively used to study the high strain-rate response of sand (Omidvar et al. 2011; Luo et al. 2014; Wang et al. 2018). Gray (2000) noted that results from the SHPB tests with specimen aspect ratios in the range of 0.25-0.5 are reliable. Therefore, in this paper, SHPB tests with specimen aspect ratios in this range from the literature are modeled using DEM.

In this study, SHPB studies on sand by Wang et al. (2018), Huang et al. (2013) and Song et al. (2009) are modeled using DEM to understand its ability in capturing the stress-strain response and PSD evolution during dynamic loading of sand. In the following sections, an overview of these SHPB tests is first presented, followed by different

methodologies adopted to model these tests in DEM including the SHPB test setup, the specimen, and particle breakage. The developed methodologies and DEM models are validated by comparing the simulated and experimental stress-strain response and evolution of PSD. The effectiveness of upscaling-downscaling procedure and particle breakage models in capturing the sand response under high strain-rate loading conditions is discussed.

5.1 Overview of SHPB Tests Modeled

Details of the three experimental SHPB studies on silica sand from the literature which are modeled in this study are shown in Table 5.1. Depending on the specimen size and whether the strain rate or stress wave was reported, the modeling of these SHPB studies serves different purposes. The purpose of modeling the tests of Wang et al. (2018) is to understand the effectiveness of upscaling–downscaling procedure for its usage in dynamic problems. The small specimen dimensions used by Wang et al. (2018) in their SHPB tests make it possible to limit the number of DEM particles and simulations are carried out with specimens prepared using the original and upscaled PSDs. The simulated stress-strain responses are compared with the reported experimental results. The PSD evolutions from the simulations are also compared. Subsequently, SHPB test by Huang et al. (2013) is simulated using upscaled specimens to study the effectiveness of an upscaled specimen in capturing the experimental stress-strain response and PSD evolution. Studies by Wang et al. (2018) and Huang et al. (2013) only reported the strain rates experienced by the specimens; therefore, the SHPB tests are modelled using the strain rate boundary condition.

Finally, the SHPB tests by Song et al. (2009) is modeled using the incident stress boundary condition. The complete SHPB test is modeled along with the specimen prepared with the upscaled PSD. The incident stress wave is applied in the IB and the dynamic stress-strain response is obtained using classic SHPB equations. The simulated response is compared with the reported dynamic response. The methodologies for modeling the SHPB tests are described in the subsequent sections.

Table 5.1. Details of the SHPB tests from literature used in this study

Studies	Reported Strain Rate or Incident Wave	Specimen Dimensions		Reported PSD Evolution	Peak Strain Rate Applied
		Length (mm)	Diameter (mm)		
Wang et al. (2018)	Strain rate	5	15	No	1200/s
Huang et al. (2013)	Strain rate	10	37.2	Yes	700/s
Song et al. (2009)	Incident wave	9.3	19.1	No	480/s

5.2 Modeling SHPB Tests in DEM

5.2.1 Methodologies in modeling SHPB setup

DEM simulations are carried out in commercial code *PFC3D* 5.0. Sand specimens are modeled as spherical particles. Two methodologies are adopted in this paper to model SHPB test setup. In the first methodology, instead of modeling the entire SHPB setup, only the IB-specimen, TB-specimen and confining tube-specimen interfaces are modeled, along with the specimen. This methodology is used to model the SHPB tests of Wang et al. (2018)

and Huang et al. (2013), where only the strain rate was reported. The interfaces are modeled using wall elements in *PFC3D*. The reported strain rates are directly applied to the DEM specimens by specifying the corresponding velocities to the IB-specimen interface while keeping the TB-specimen interface stationary. This methodology has been adopted to model quasi-static and dynamic tests on sand and concrete (Hentz et al. 2004; Huang et al. 2014; Hanley et al. 2015). Specimen strain (ε) is calculated from the applied strain rate $\dot{\varepsilon}$ as

$$\varepsilon\,(t) = \int_0^t \dot{\varepsilon}(t)\; dt \tag{5.1}$$

while the IB-specimen and TB-specimen interface forces are converted to interface stresses by dividing the specimen cross-sectional area. The stress in the specimen can be either taken as the calculated stress at the TB-specimen interface or the average of the two interface stresses; if stress equilibrium is valid during the tests, these two approaches give similar specimen stress.

The second methodology is used to model the SHPB test by Song et al. (2009), where the stress waves were reported, and the complete SHPB test setup including the IB, TB, confining tube and sand specimen are modeled in *PFC3D*. The IB and TB metal bars are modeled as a set of spheres aligned in a line representing a cylindrical steel metal bar. Properties of the spheres are calculated to replicate the wave propagation in the steel bar (Ithasca 2016). Each sphere in this set represents an equivalent cylindrical bar of radius *R* and length 2*R*. The number of balls representing the IB (N_I) and TB (N_T) are obtained using the following equations

$$N_I = \frac{L_I}{2R} \tag{5.2}$$

$$N_T = \frac{L_T}{2R} \tag{5.3}$$

where L_I and L_T are the IB and TB bar lengths, respectively. Linear contact model is used for these spheres and for the continuum bar, the Youngs modulus (E) can be calculated as

$$E = \frac{\sigma}{\varepsilon} = \frac{F/\pi R^2}{u/2R} \tag{5.4}$$

where σ and ε are applied stress and strain, respectively; F and u are the contact force and displacement, respectively. At a ball-ball contact

$$F/u = k_n^{ball}/2 \tag{5.5}$$

where k_n^{ball} is the normal stiffness of the ball-ball contact. Substituting Eq. (5.5) into Eq. (5.4) yields

$$E = k_n^{ball}/\pi R \tag{5.6}$$

The stress wave propagation through a medium is dependent on the mass density of the particle; therefore, mass conservation is used to obtain the density of spheres ρ_{ball} representing the IB and TB

$$4\pi R^3/3 \times \rho_{ball} = 2\pi R^3 \times \rho_{bar} \tag{5.7}$$

The longitudinal wave velocity in a bar is given by $c_{bar} = \sqrt{E/\rho_{bar}}$, which can be substituted into Eq. (7) and yields

$$k_n^{ball} = \pi R \rho_{bar} c_{bar}^2 \tag{5.8}$$

For a longitudinal stress wave passing through a metal bar, the stress magnitude is provided by

$$\sigma = \rho_{bar} c_{bar} \dot{u} \tag{5.9}$$

The IB-specimen, TB-specimen, and specimen-confining tube interfaces are modeled using wall elements in *PFC3D*. The input stress wave is applied as a time-varying stress

pulse at the ‘free end’ of the IB, away from the specimen. The generated stress wave propagates through the spheres representing the IB and reaches the IB-specimen interface. The IB-specimen interface is moved using a servo control mechanism. A part of the incident pulse is reflected and a part is transmitted into the specimen at the IB-specimen interface. The sand specimen is modeled using discrete spheres with each sphere representing a single sand grain. As the stress wave propagates in the specimen and reaches the TB-specimen interface, a similar servo control mechanism is used to control the movement of the TB-specimen interface. Fig. 5.1 shows the SHPB test setup generated in *PFC3D*. The wave velocity in the IB and TB is converted into stresses using Eq. (5.9) and stress-strain response of the specimen is derived using classic SHPB equations given by

$$\varepsilon(t) = -2\frac{c_o}{L_s}\int_0^t \varepsilon_r(t)\ dt \tag{5.10}$$

$$\sigma_t(t) = \frac{A_o}{A_s}E_o\varepsilon_r(t) = E_o\varepsilon_r(t) \tag{5.11}$$

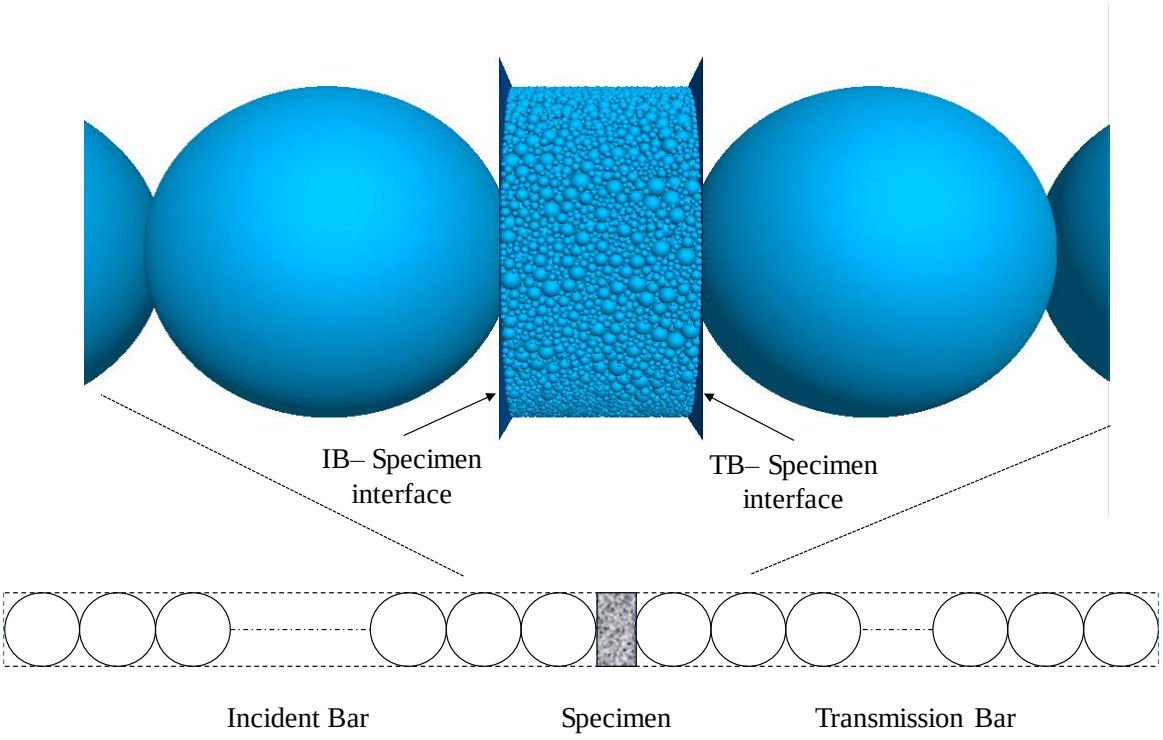

Fig. 5.1. Images of the DEM specimen, IB and TB used in the current study (not to scale)

Song et al. (2009) used steel IB and TB with lengths of 4100 mm 2400 mm, respectively, and a diameter of 19.1 mm. The properties of the bars used in the experiments and the corresponding *PFC3D* simulations are shown in Table 5.2.

Table 5.2. Properties used in experiments (Song et al. 2009) and DEM simulations

Property	Value
SHPB Bar Properties	
N_I	216
N_T	108
E	200 GPa
ρ_{bar}	8.1×10^3 kg/m^3
c_{bar}	4959 m/s
R	0.00955 m
IB and TB ball: k_n^{ball}	6×10^9 N/m
IB and TB ball: ρ_{ball}	1.251×10^4 kg/m^3
Sand Particle Properties	
G	30 GPa
v	0.3
μ_s	0.5
Wall-specimen Interface Properties	
k_n	2.6×10^6 N/m
k_s	1.6×10^6 N/m
μ_i	0: lubrication, Huang et al. (2013
	0.3: no lubrication, Wang et al. (2018) and Song et al. (2009)

5.2.2 Modeling of DEM specimen

For both methodologies adopted to model SHPB tests, sand specimens are similarly prepared in DEM with sand particles being modeled as spheres. Studies have showed that Hertzian contact model accurately captures the nonlinear sand response and therefore is used in the present study (De Bono and McDowell 2014; Hanley et al. 2015). The detailed description of the Hertzian contact model is provided by Mindlin (1949). The interaction between the interfaces and specimen spheres are modeled using the linear contact model. Two interface friction conditions, smooth and rough, are considered in the DEM simulation

for the interface-specimen interaction. For the SHPB experiments carried out without interface lubrication, an interface friction value of 0.3 is applied at the interfaces while for simulations of SHPB experiments with interface lubrication, a value of 0 is provided. Only dry silica sand is considered in this paper and each sand grain (i.e., DEM particle) is assumed to have a specific gravity (G_s) of 2.65, a shear modulus (G) of 30 GPa, and a Poison's ratio (υ) of 0.3 (Yimsiri and Soga 2010). The DEM sphere-sphere friction value is assumed to be 0.5 which is the typical value of particle-particle friction for silica sands (DeBono and McDowell 2014). The interface and DEM sand particle properties are listed in Table 5.2.

In the DEM simulations, the angular shapes of sand grains are simplified to be spheres while in reality, the sand considered in this study are sub-angular. The angularity of sand particles is implicitly accounted by applying an additional rotational resistance to the spherical particles representing sand. At each time step, the angular particle rotation of sand particles is reduced (Kermani et al. 2015; Teufelsbauer et al. 2009):

$$\omega_i{}^{t+1} = k_\lambda{}^{\xi}\, \omega_i{}^{t} \tag{5.12}$$

where $\omega_i{}^{t+1}$ is the angular velocity at a particular time, $\omega_i{}^{t}$ is the angular velocity from the previous time step, and $k_\lambda{}^{\xi}$ is a retarding coefficient. The magnitude of the retarding coefficient, $k_\lambda{}^{\xi}$, is dependent on the timestep and calibrated to be 0.99999975 in this study.

5.2.3 Particle breakage model

Ciantia et al. (2014, 2015, 2019) developed Hertizian contact (HC) breakage model in DEM and showed that HC breakage model captured the particle breakage in silica and Fontainebleau sands. The HC breakage model uses a force criterion and the limiting force, F_{Lim}, is used to determine whether a particle undergoes breakage

$$F_{Lim} \leq \sigma_{lim,0} \left(\frac{d}{d_o}\right)^{-\frac{3}{m_1}} \pi \left(\frac{3F r^{'}}{4E^{'}}\right)^{\frac{2}{3}} . var \quad (5.13)$$

where $\sigma_{lim,0}$ is the strength of sand particle with diameter d_o of 2 mm; F is the contact force on a particle with diameter d; $r^{'} = \left(\frac{1}{r_1} + \frac{1}{r_2}\right)^{-1}$; $E^{'} = \left(\frac{1-\nu_1{}^2}{E_1} + \frac{1-\nu_2{}^2}{E_2}\right)^{-1}$; ν_1, E_1, r_1, ν_2, E_2, and r_2 are the poisons ratio, elastic modulus and radius of the spheres in contact; m_1 is the Weibull modulus defining the variation of sand particle strength as a function of particle size; and var accounts for the variation of sand particle strength for a given size. Ciantia et al. (2015) showed that the value of $\sigma_{lim,0}$ is proportional to the upscaling factor. McDowell (2001) noted that for sand particles with the same diameter, the strength follows a Weibull (1951) distribution and the survival probability (P_s) of a particle is given by

$$P_s = exp\left(-\frac{\sigma}{\sigma_o}\right)^{m_2} \quad (5.14)$$

where m_2 is the Weibull modulus; σ_o is the characteristic strength for a particle size such that 37% of the particles survive; and σ is the stress applied on the particle. Studies (Nakata et al. 2001; McDowell 2002; Cheng et al. 2003) reported the values of Weibull modulus m_1 and m_2 to be 3 for silica sand and, therefore, this value is used throughout this paper. Hanley et al. (2015) approximated the Weibull function using a linear function given by

$$var = \frac{U(0,1)-b}{a} \quad (5.15)$$

where $U(0,1)$ is a random number following the uniform distribution varying from 0 to 1; a and b are constants and, for silica, are calculated to be -1.22 and 1.67, respectively. For $U(0,1)$ of 1, the P_s is 0.55 while for $U(0,1)$ of 0, the P_s value is 1.37.

Even though the HC model predicted the mechanical response of sand at quasi-static strain rates accurately, Ciantia et al. (2015) used large particle comminution limits and only allowed particles larger than $0.55\times d_{50}$ to break, which masked the PSD evolution in the simulation. The model also does not account for the confinement effect provided to the larger particles by smaller particles. High stresses on sand specimens cause significant particle breakage in the specimen leading to large number of smaller particles. The smaller particles provide confinement or 'cushioning' to larger particles, effectively preventing the breakage of these large particles (Lade et al. 1996; Nakata et al. 2001; Guerrero and Vallejo 2005). Guerrero and Vallejo (2005a)s introduced a coordination number limit in their DEM simulation to account for the confinement and only allowed particles with coordination number lower than a specified limit to break. A similar methodology is introduced in this paper and a coordination number limit (c_{lim}) is introduced. In this paper, a lower comminution limit of $0.22\times d_{50}$ is used which allows considerable particle breakage to occur in the specimen.

In the simulation, the force criterion (Eq. 5.13) and the contact limit criterion are checked on all sand particles. The particles satisfying both criteria are deemed broken and the broken parent particle is replaced with 14 daughter particles without overlap (Fig. 5.2a). The daughter particles configuration is subsequently rotated and aligned such that the center of the three largest daughter particles lie on a plane perpendicular to the direction of

maximum force (Fig. 5.2b). Table 5.3 shows the radius and coordinates of the center of the daughter particles.

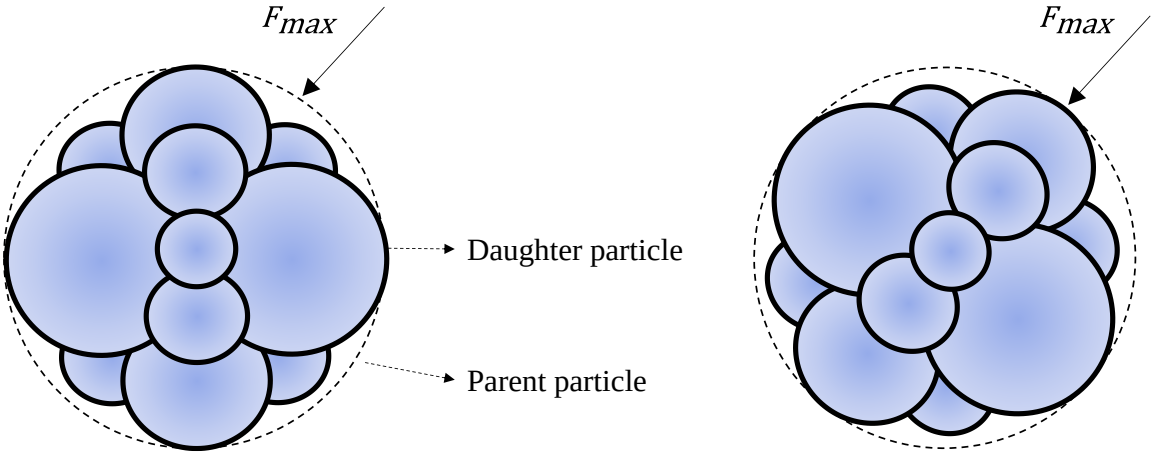

Fig. 5.2. Parent and daughter particle configurations: (a) before rotation; (b) after rotation

Table 5.3. Coordinates and Radius of fourteen ball daughter configuration

r/R	***x'/R***	***y'/R***	***z'/R***
0.4641	0	0.5359	0
0.4641	-0.4641	-0.2679	0
0.4641	0.4641	-0.2679	0
0.2240	-0.6720	0.3880	0
0.2240	0.6720	0.3880	0
0.2240	0	-0.7760	0
0.3659	0	0	0.6339
0.3659	0	0	-0.6339
0.2573	0	-0.5942	0.4456
0.2573	0.5146	0.2971	0.4456
0.2573	-0.5146	0.2971	0.4456
0.2573	0	-0.5942	-0.4456
0.2573	0.5146	0.2971	-0.4456
0.2573	-0.5146	0.2971	-0.4456

The sizes of these daughter particles follow an apollonian distribution with a fractal dimension of 2.47 and the daughter particles retain 53% of parent particle mass. Ciantia et al. (2015) showed that increasing the number of particles beyond 14 did not affect the mechanical sand response. The daughter particles are assigned the same properties and velocities as the parent particle. The daughter particles, replacing the parent particle are free to undergo further breakage if the breakage and contact limit criteria are satisfied and if the particle size is larger than the comminution limit considered.

The 47% of lost mass during each parent particle breakage is assumed to follow a fractal distribution and is re-distributed in the PSD as

$$\frac{M_{(L<d)}}{M_T} = \frac{d^{3-\alpha} - {d_{min}}^{3-\alpha}}{{d_{max}}^{3-\alpha} - {d_{min}}^{3-\alpha}} \tag{5.16}$$

where M_T is the total mass; $M_{(L<d)}$ is the mass of particles smaller than d; d_{max} is the diameter of the smallest sphere in the apollonian configuration of 14 daughter balls; d_{min} is the smallest particle size in the PSD; and α is the fractal dimension. After particle breakage, 47% of the parent particle mass is lost and this mass is added back to the PSD using a fractal distribution with a fractal dimension of 2.6 (McDowell et al. 1996; Altuhafi and Coop 2011). Detailed explanation for obtaining the PSD after particle breakage is presented in Ciantia et al. (2015).

5.3 Results and Discussions

5.3.1 Modeling of SHPB tests by Wang et al. (2018)

Wang et al. (2018) carried out SHPB tests on poorly-graded silica sand at different dry densities. The reported stress-strain response for dry sand at a porosity of 0.41 is used in this study. Fig. 5.3 shows the strain rate reported on the specimen. Fig. 5.4 shows the original and upscaled PSDs used to prepare the DEM specimens, where the upscaled PSD is obtained by shifting the original PSD to the right by an upscaling factor of 1.5. Fig. 5.5 shows the DEM specimens prepared with the original and upscaled PSDs, having 43,642 and 12,824 particles, respectively. The strain rate (Fig. 5.3) is applied on the DEM specimens by prescribing the interface wall velocities. As the SHPB tests by Wang et al. (2018) were carried out without any interface lubrication, a ball-interface friction value of 0.3 is used in the simulations Frost et al. (2002) (see Table 5.2).

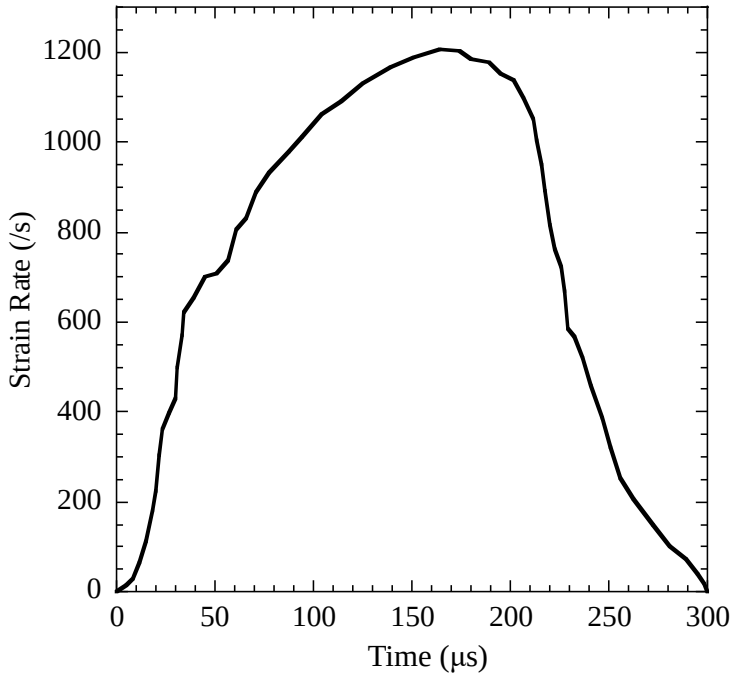

Fig. 5.3. Strain rate reported in SHPB tests (data digitized from Wang et al. 2018)

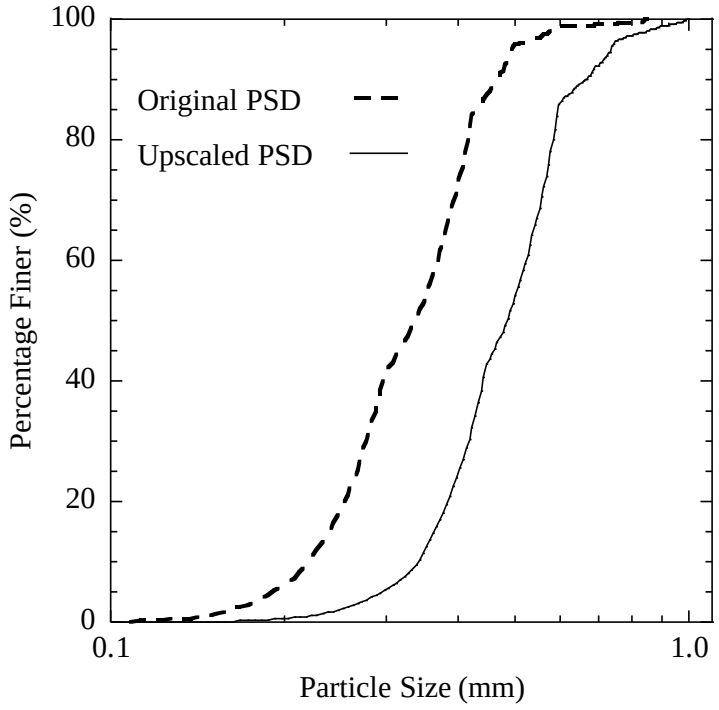

Fig. 5.4. Original and upscaled PSDs for modeling Wang et al. (2018) tests

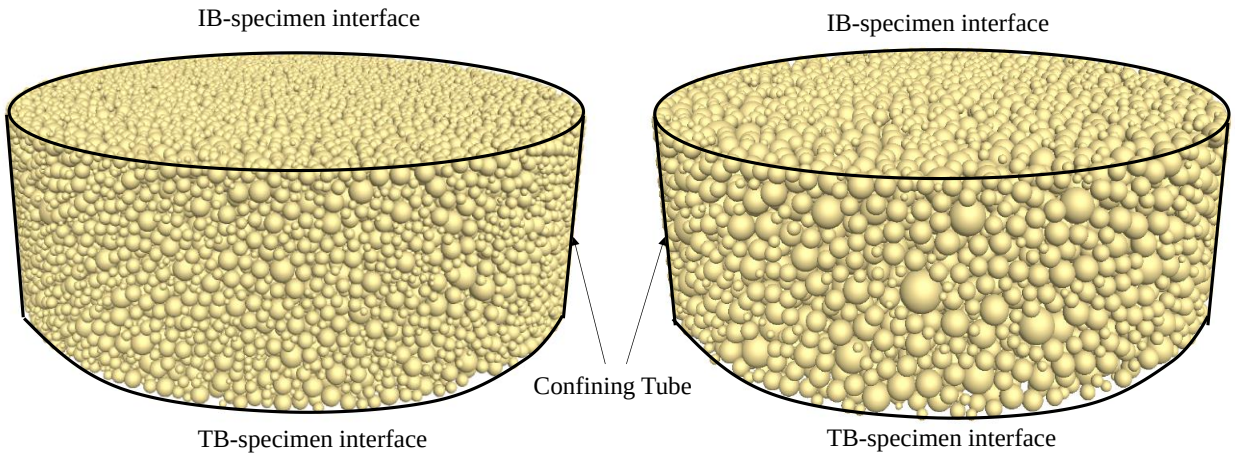

Fig. 5.5. Specimens used in DEM modeling of Wang et al. (2018) tests: (a) original PSD with 43,642 particles; (b) upscaled PSD with 12,824 particles

Fig. 5.6 shows a comparison between the simulated and experimental stress-strain responses. The values of $\sigma_{lim,0}$ and c_{lim} are calibrated as 1.53 GPa and 8, respectively, for the original PSD specimen and 2.37 GPa and 8, respectively, for the upscaled specimen. Fig. 5.6 shows that with these calibrated parameters, DEM simulations can capture the overall dynamic stress-strain behavior. At low stresses, the simulated responses for specimens prepared with the original and upscaled PSDs are similar, in accordance with the results reported by Prabhu and Qiu (2019). At high stresses, the stress-strain curve of the DEM specimens is influenced by the $\sigma_{lim,0}$ and c_{lim} values. Therefore, these parameters for particle breakage should be calibrated to yield similar responses between the specimens prepared using the original and upscaled PSDs. Due to particle breakage, the specimen with original PSD has 136,000 particles while the specimen with upscaled PSD has 40,000

particles at the end of simulation. The simulated stress-strain responses are similar to and within the error bars of the experimental responses.

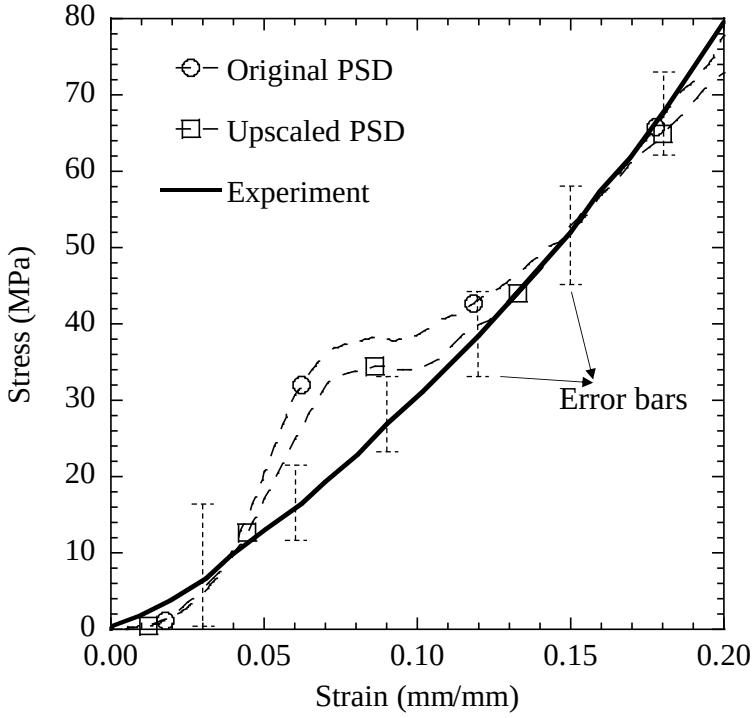

Fig. 5.6. Comparison of simulated and experimental stress–strain responses for Wang et al. (2018) test

In the simulation, d_{min}=7.5 μm is used in Eq. (5.16) to obtain the PSD evolution during the test. For the simulation based on the upscaled PSD, to enable a more direct comparison, the simulated PSD is downscaled by shifting to the left using the same scaling factor of 1.5 used for upscaling. Fig. 5.7 shows the comparison of PSDs from the simulated responses for the original and upscaled specimens at 43 MPa and 72 MPa. It is evident from Fig. 5.7 that the upscaling-downscaling procedure can accurately capture the PSD evolution similar

to that using the original PSD. Additionally, the breakage coefficient (B_r) defined by Hardin (1985) as the ratio between the area enclosing the initial and final PSD for particle sizes greater than 75 μm, to the total area above the initial PSD curve for particle sizes greater than 75 μm, is calculated. At the end of simulation, value of B_r is calculated to be 0.28 while the experimental value of B_r was reported to be in the range of 0.3-0.35 by Wang et al. (2018). Figs. 5.6 and 5.7 suggest that with properly calibrated parameters, the upscaling-downscaling procedure can efficiently reduce the computational effort for dynamic problems involving sand, while replicating the overall stress-strain response and PSD evolution.

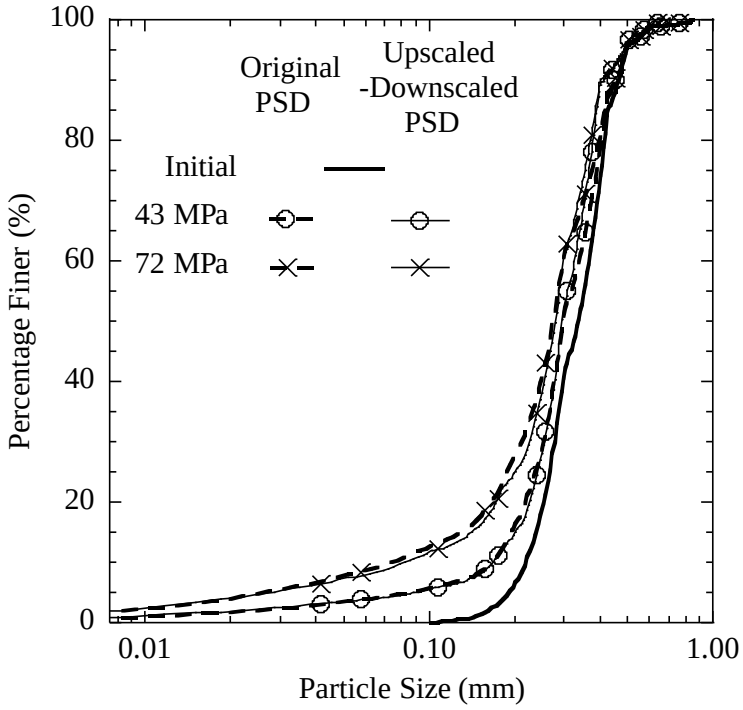

Fig. 5.7. PSD evolution in DEM simulation for the original and upscaled-downscaled PSDs for Wang et al. (2018) tests

Additionally, a parametric study is carried out to understand the significance of particle breakage on the dynamic sand response and the importance of the c_{lim} criterion in the simulation. The SHPB tests are simulated with the same input parameters and strain rate reported in the previous section. Two additional simulations are carried out on specimens with different particle breakage criterion. In the first simulation, particles are not allowed to break; in the second simulation, no contact limit criterion is provided and any particle, satisfying the force criterion, is deemed broken and replaced by daughter particles (i.e., c_{lim}=0). The methodology is similar to that used by Ciantia et al. (2015), however, a smaller comminution limit of $0.22 \times d_{50}$ is used in this study. The same value of $\sigma_{lim,0}$ as that calibrated in the previous section is used in the force criterion. Fig. 5.7 shows the stress-strain responses from these two additional simulations (i.e., no breakage and c_{lim}=0) compared with the simulated response reported in the previous section (i.e., c_{lim}=8). As observed in Fig. 5.8, at low stresses, the stress-strain responses of the simulations are similar as the particle breakage is minimal and the dynamic response is governed by the particle contact behavior. The stress-strain responses deviate after the initiation of particle breakage as the specimen without particle breakage shows stiffer response at high stresses. Fig. 5.8 also shows the importance of introducing the c_{lim} criterion for the dynamic problems as a lack of this criterion leads to excessive particle breakage, providing a much softer stress-strain response. The authors also carried out simulations with different $\sigma_{lim,0}$ values on specimens with HC particle breakage model without contact limit criterion. However, the authors were unable to capture the actual stress-strain response reported in the experiments; hence, the results are not presented herein.

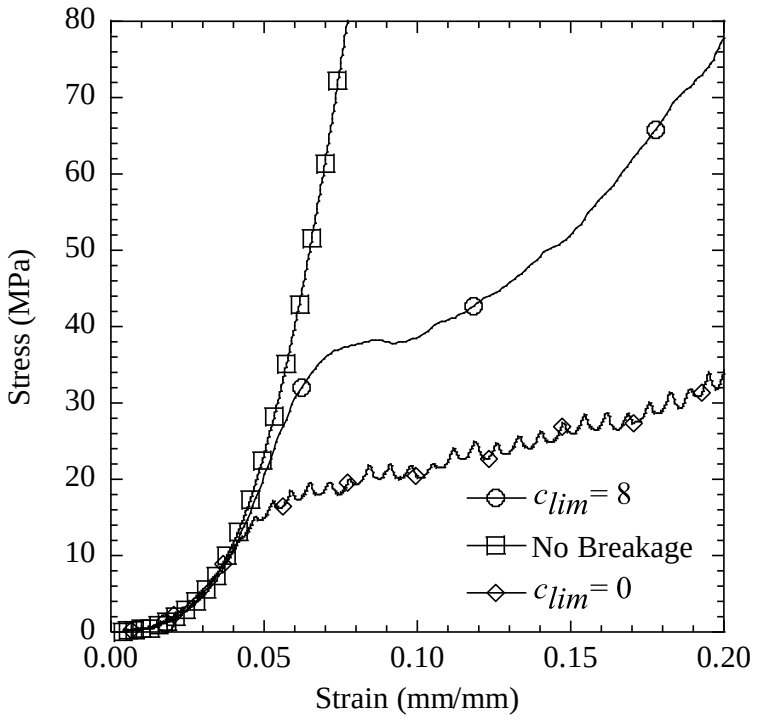

Fig. 5.8. Stress–strain response from DEM simulations for different breakage criteria

5.3.2 SHPB tests by Huang et al. (2013)

Huang et al. (2013) carried out SHPB tests on fine silica sands at different strain rates (400/s, 700/s and 1000/s) and showed that stress-strain response of sand is independent of the strain rate for the range considered. As the response is similar, only the test with a strain rate of 700/s is modeled in this study. Fig. 5.9 shows the PSD of sand used in the experiment. Researchers (Guerrero and Vallejo 2005 a,b) noted that the stress-strain response of sand is dominated by larger particles in the specimen. Therefore, in the present study, the tail portion of the original PSD is ignored in the simulation as this portion significantly increases the number of particles without any significant effect on the stress-strain response. The PSD is approximated by ignoring the tail portion and restricting the

smallest particle size to 0.1 mm. The approximated PSD is then upscaled by a scaling factor of 2.5 to obtain the upscaled PSD (Fig. 5.9), resulting in 37,595 particles for the upscaled specimen. Huang et al. (2013) used petroleum jelly to lubricate the interfaces; therefore, the interfaces in the simulation are considered to be frictionless and a zero-friction coefficient is used for ball-wall interfaces (see Table 5.2). The same value of c_{lim} as that calibrated in the previous section is used in this simulation and for the upscaling factor considered, the value of $\sigma_{lim,0}$ is calibrated to be 3.6 GPa by comparing the simulated and experimental stress-strain response.

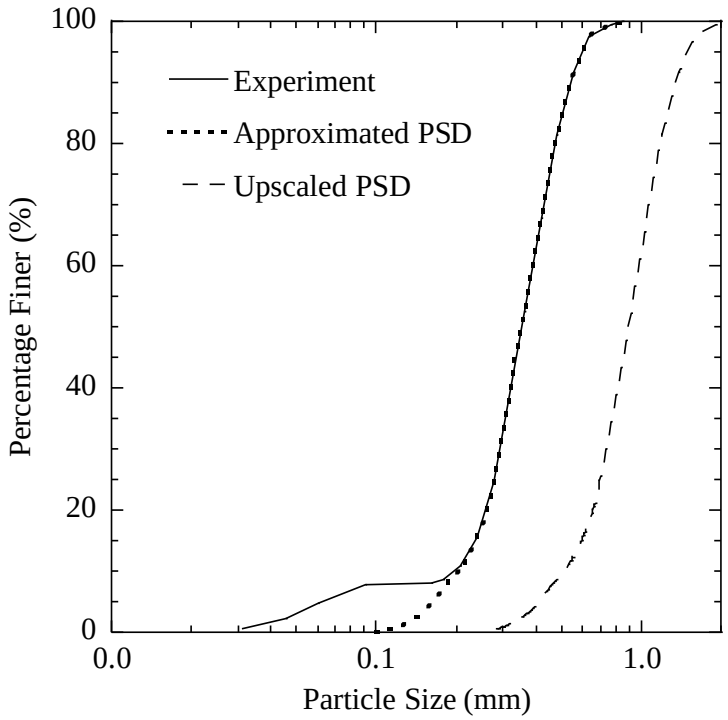

Fig. 5.9. Original PSD used by Huang et al. (2013) and approximated and upscaled PSDs used in the DEM simulations

Fig. 5.10 shows the simulated and experimental stress-strain responses and demonstrates that the DEM model accurately captures the stress-strain response. To further understand the validity of the breakage model implemented in the simulation and its effectiveness in capturing sand breakage in dynamic problems, the PSD from the model is compared with the reported PSD at different stresses. Downscaling procedure is adopted and the simulated PSD is shifted to the left by a scaling factor of 2.5 with the smallest particle size taken to be 0.01 mm. After downscaling, the tail portion ignored in the approximated PSD is added back to the downscaled PSD. Fig. 5.11 shows the comparison of the simulated and reported PSDs at 18.2 MPa and 42.5 MPa (to demonstrate the evolution of PSD for small particles, a log-log plot is used). Fig. 5.11 demonstrates that the DEM model accurately captures the PSD evolution at both stresses. At 18.2 MPa stress, the number of primary and secondary daughter particles are 14,000 and 0, respectively; at 42.5 MPa, the corresponding numbers are 42,000 and 300. Therefore, it is noted that the secondary breakage is much lower compared to the primary breakage in the model. Figs. 5.10 and 5.11 suggest that the particle breakage model is capable of accurately replicating the dynamic tests on sand as it captures both the stress-strain response and the PSD evolution.

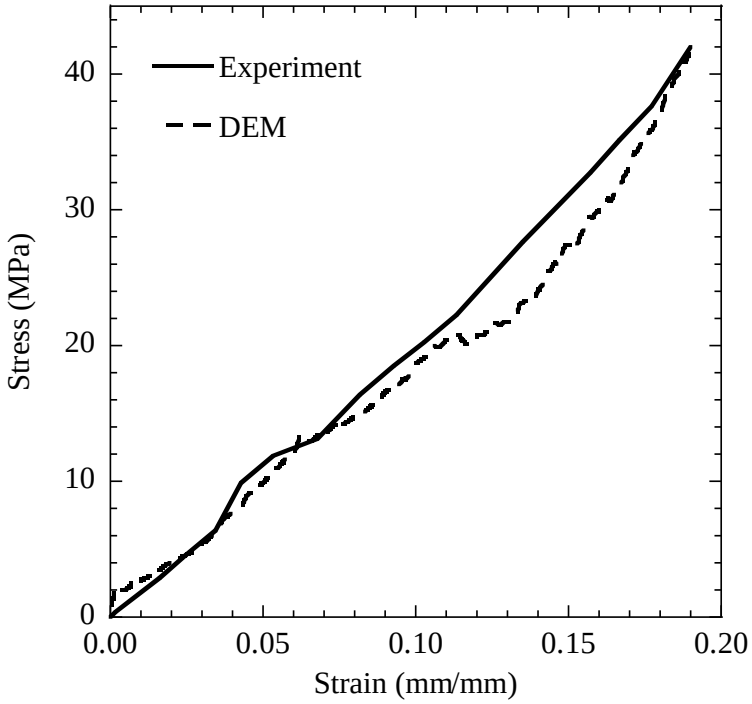

Fig. 5.10. Comparison of stress–strain responses from experiments reported by Huang et al. (2013) and simulation

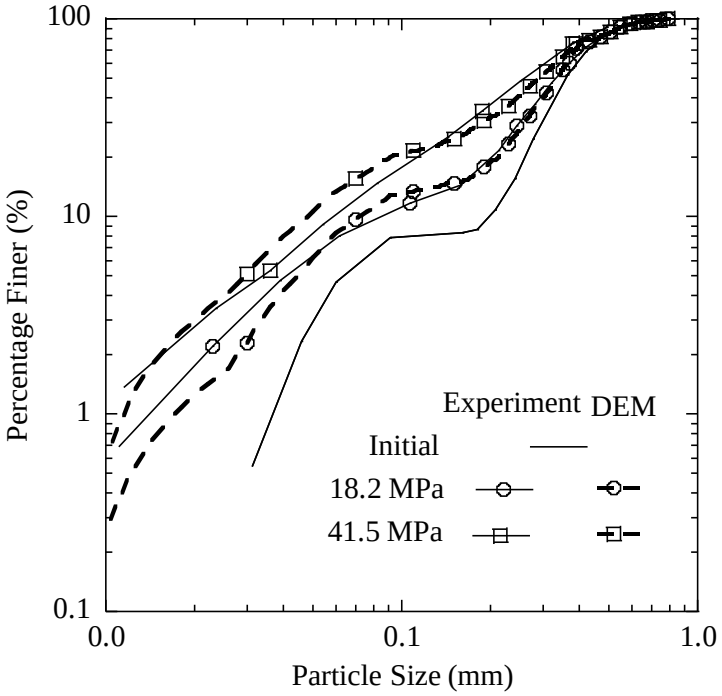

Fig. 5.11. PSD evolutions reported by Huang et al. (2013) and from DEM simulation

Fig. 5.12 shows the number of particles broken in the simulation as a function of stress in a semi-log plot. Fig. 5.12 demonstrates that only few particles are broken at low stresses (<10 MPa). However, an increase in stress beyond 10 MPa leads to a rapid increase in the particle breakage events, producing a yield point (i.e., the point of maximum curvature) in the semi-log plot. Huang et al. (2013) noted similar yield point in the dynamic stress-strain response of sand at an approximate stress of 10 MPa and attributed this to the domination of particle breakage at higher stresses. The DEM model captures the stress-strain response at both low stresses (<10 MPa), where the response is dominated by contact behavior, and high stresses (>10 MPa) where the response is dominated by particle breakage, consistent with experimental observations.

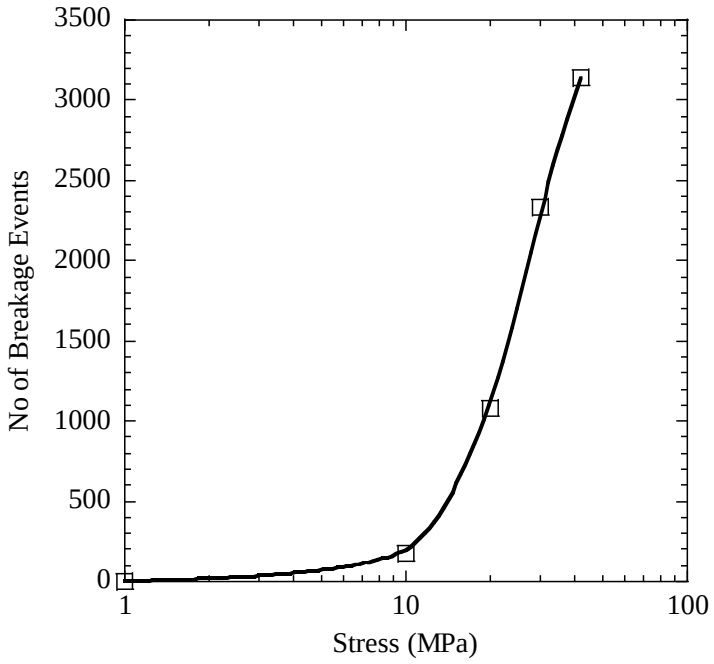

Fig. 5.12. Number of broken particles at different stresses in DEM simulation

5.3.3 SHPB tests by Song et al. (2009)

Song et al. (2009) carried out SPHB tests on poorly-graded dry silica sand at a strain rate of 480/s. The specimens were prepared at a porosity of 0.45 and the PSD is shown in Fig. 5.13. Detailed physical properties of the sand are reported in Martin (2007) and Kabir et al. (2010). Song et al. (2009) reported that the sand specimen achieved stress equilibrium and therefore, the strains measured in the IB and TB were converted into stress-strain response using Eqs. (5.10) and (5.11). The DEM specimens used in this study are prepared with an upscaling factor of 2 as shown in Fig. 5.13 with the same porosity as that reported in the experiments. The upscaled DEM specimen consists of 34,411 DEM particles. The complete SHPB test setup is modeled and the incident stress wave (Fig. 5.14) is applied at the 'free end' of the IB. Song et al. (2009) reported the incident, reflected and transmitted stress waves for tests carried out in a polycarbonate confining tube with identical sand specimen and noted that the stress waves were similar for the tests carried out in the steel confining tube. Through a continuum-scale numerical study, Prabhu and Qiu (2020) confirmed that the effect of the stiffness of the confining tube on SHPB tests on sand specimens was minor. Fig. 5.14 shows the incident, reflected and transmitted stress waves reported by Song et al. (2009) for the polycarbonate confining tube and the corresponding stress waves obtained from the DEM simulation based on the steel confining tube. The time zero on the *x* axis corresponds to the time when the incident wave is applied to the IB. The stress-strain response of the DEM model is obtained using the classic SHPB equations. In the simulation, the same c_{lim} value of 8 calibrated from the previous section is used while $\sigma_{lim,0}$ is calibrated to be 2.7 GPa.

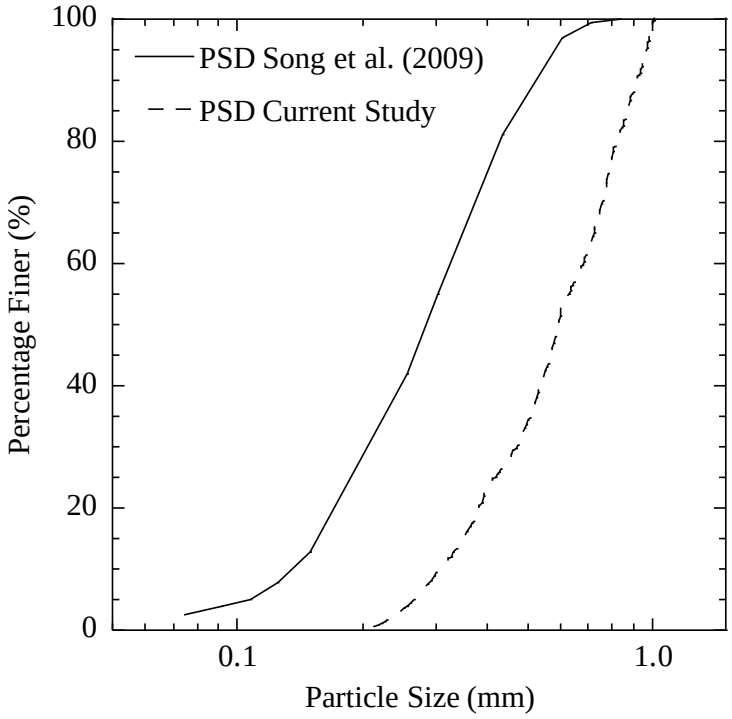

Fig. 5.13. Original and upscaled PSDs for modeling Song et al. (2009) tests

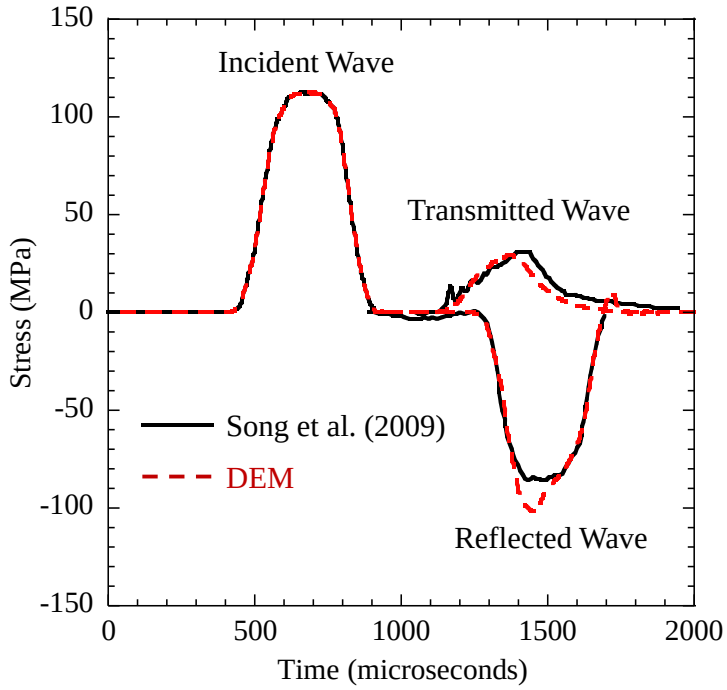

Fig. 5.14. Incident, reflected and transmitted stress waves reported by Song et al. (2009) and from DEM simulations (test data digitized from Song et al. (2009)

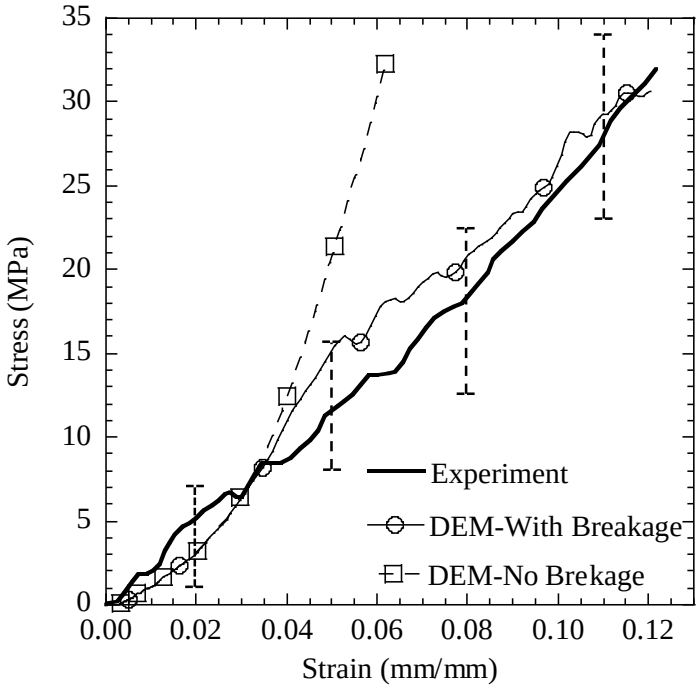

Fig. 5.15. Stress-strain response of dry sand with steel confinement reported by Song et al. (2009) and from DEM simulations

To further understand the effect of particle breakage on the dynamic stress-strain response, an additional SHPB simulation is carried out on the same test setup and input parameters without particle breakage. Fig. 5.15 shows the simulated and experimental stress-strain responses, along with the reported error bars. Fig. 5.15 demonstrates that the effect of particle breakage on the stress-strain response is evident only at stresses above 10 MPa as the stress-strain responses below 10 MPa are similar with or without particle breakage. However, at higher stresses (>10MPa), particle breakage softens the stress-strain response, highlighting the importance of simulating particle breakage at high stresses. It is evident from Fig. 5.15 that with the calibrated parameters, the DEM model can replicate the dynamic stress-strain response of the sand specimen in SHPB tests.

5.3.4 Varioation of $\sigma_{lim,0}$ as a function of upscaling factor

Ciantia et al. (2015) showed that the single particle crushing strength, $\sigma_{lim,0}$, is a function of the upscaling factor, *N*. However, none of the simulations reported in literature derived the relation between $\sigma_{lim,0}$ as a function of *N*. Ciantia et al. (2015, 2019) showed that $\sigma_{lim,0}$ increases with an increase in *N* and assumed

$$\sigma_{lim,0}\,(N) = \sigma_{lim,0}\,(N=1)\left(\frac{1}{N}\right)^{-3/m_1} \tag{5.17}$$

where $\sigma_{lim,0}\,(N)$ and $\sigma_{lim,0}\,(1)$ are the strength of 2-mm particles for specimens prepared with an upscaling factor of *N* and actual PSD, respectively. In the present study, the value of $\sigma_{lim,0}$ for any value of *N* is obtained individually from back calculation. Fig. 5.16 shows the variation of $\sigma_{lim,0}$ with *N* along with Eq. (5.17).

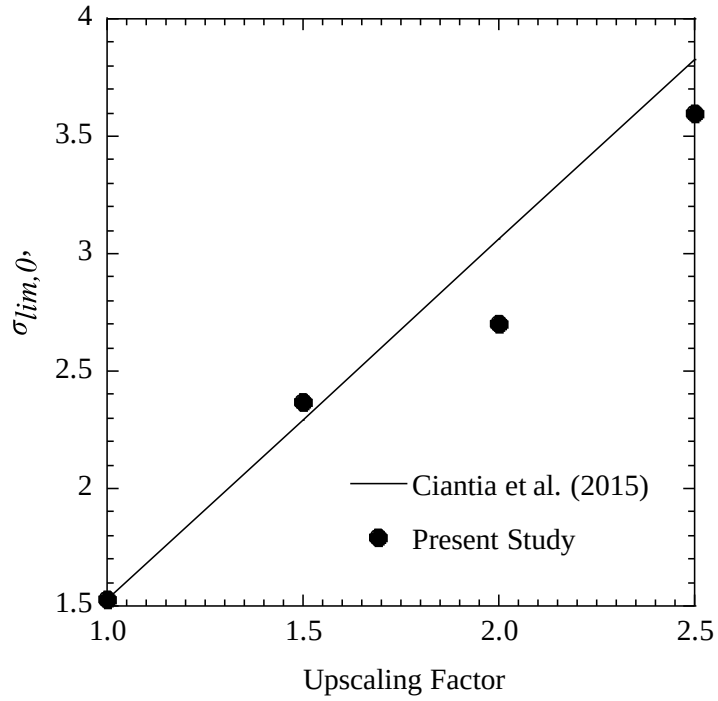

Fig. 5.16. Variation of $\sigma_{lim,0}$ as a function of upscaling factor (*N*)

5.4 Conclusion

In this study, a series of SHPB tests reported in the literature are modeled in DEM using different methodologies. The simulated stress-strain responses and evolution of PSD are compared with the reported responses. As particle breakage dominates the stress-strain response at high stresses, particle breakage is introduced in the simulation using a force criterion. Particles satisfying the force criterion is replaced by a set of daughter particles. Using these simulations, the effectiveness of grain size upscaling-downscaling procedure in reducing the computational cost in dynamic problems is discussed. The following conclusions are reached.

1. The upscaled specimens provided the same response as the original specimens. With properly-calibrated DEM parameters, the stress-strain responses reported by the original and upscaled specimens prepared at same porosity and dimensions are generally similar. At low stresses, the stress-strain response is governed by the property of the sand particles and contact behavior while at high stresses, the response is dominated by the particle breakage model properties.

2. For the particle breakage model used in this study, the PSD evolution of the original and upscaled specimens are similar after implementing the upscaling-downscaling procedure.

3. The wave propagation in the steel bars and the incident, reflected and transmitted stresses reported in literature are accurately replicated by the developed DEM model. The modeled stress-strain response is within the error bars reported; hence, the developed DEM model can be used to model the complete SHPB test setup on sand specimens.

Reference

Altuhafi, F. N. and Coop, M.R. (2011). "Changes to particle characteristics associated with the compression of sands." *Geotechnique.* 61(6): 459–471.

Barr, A. D. (2016). "Strain rate effects in quartz sand." PhD thesis, Department of Civil and Structural Engineering. The University of Sheffield.

Ben-Nun, O. and Einav, I. (2008). "A refined DEM study of grain size reduction in uniaxial compression." In: 12th International conference on international association for computer methods and advances in geomechanics (IACMAG). 1–6.

Cao S., Song, W. D. and Yilmaz, E (2018). "Influence of structural factors on uniaxial compressive strength of cemented tailings backfill." *Constr. Build. Mater.* 174: 190–201.

Cheng, Y. P., Nakata, Y. and Bolton, M. D. (2003). "Discrete element simulation of crushable soil." *Geotechnique.* 53: 633-641.

Ciantia, M., Arroyo, M., Gens, A. and Calvetti, F. (2014). "Particle failure in DEM models of crushable soil response." *In Numerical methods in geotechnical engineering*, NUMGE. (eds M. A. Hicks, R. B. J. Brinkgreve and A. Rohe), 345–350. Leiden, the Netherlands: CRC Press/Balkema 2014.

Ciantia, M. O., Arroyo, M., Calvetti, F. and Gens Solé, A. (2015). "An approach to enhance efficiency of DEM modelling of soils with crushable grains." *Géotechnique.* 65(2): 91–110.

Ciantia, M. O., Arroyo, M., O'Sullivan, C., Gens, A. and Liu, T. (2019). "Grading evolution and critical state in a discrete numerical model of Fontainebleau sand." *Géotechnique*. 69(1): 1–15.

Cil, M.B. and Alshibli, K. A. (2012). "3D assessment of fracture of sand particles using discrete element method." *Geotech. Letters.* 2(3): 161–166

Cundall, P. A., Strack, O. D. L. (1979). "A discrete numerical model for granular assemblies." *Geotechnique.* 29(1): 47–65.

DeBono, J. P., McDowell, G. R., and Wanatowski, D. (2014). "DEM of triaxial tests on crushable cemented sand." *Granular Matter.* 16: 563–572.

De Bono, J. P. and McDowell, G.R. (2014). "DEM of triaxial tests on crushable sand." *Granular Matter.* 16(4): 551–562.

DeBono, J. and Mcdowell, G. (2016). "Particle breakage criteria in discrete element modelling." *Geotechnique.* 66: 1014–1027.

Frost, J. D., DeJong, J. T. and Recalde, M (2002). "Shear failure behavior of granular–continuum interfaces." *Engineering Fracture Mechanics.* 69: 2029–2048.

Gray, G. T. and Blumenthal, W. R. (2000). "Split-Hopkinson pressure bar testing of soft materials." In: Kuhn H, Medlin D,editors. ASM handbook: mechanical testing and evaluation, vol. 8. Materials Park, OH: ASM International; 488–496.

Hanley, K. J., O'Sullivan, C. and Huang, X. (2015). "Particle-scale mechanics of sand crushing in compression and shearing using DEM." *Soils Found.* 55(5): 1100–1112.

Hardin, B. O (1985). (1985). "Crushing of soil particles." *J. Geotech. Engrg.* 111(10): 1177- 1192.

Hentz, S., Donze, F.V. and Daudeville, L. (2004). “Discrete Element modeling of concrete subjected to dynamics loading at high strain rates.” *Computers and Structures.* 82: 2509-2524.

Huang, J., Xu, S. and Hu. S. “Effects of grain size and gradation on the dynamic responses of quartz sands.” *International Journal of Impact Eng.* 59: 1–10.

Huang, J., Xu, S. and Hu, S. (2014). “Influence of particle breakage on the dynamic compression responses of brittle granular materials.” *Mechanics of Material.* 68(1): 15-28.

Itasca. (2016). “Particle Flow Code in three dimensions: Software manual.” Minnesota, MN, USA.

Kabir, M. E., Song, B., Martin, B.E. and Chen, W. (2010). “Compressive behavior of fine sand.” Technical report, Sandia National Laboratories, Albuquerque, New Mexico 87185 and Livermore, California 94550, 2010.

Kermani, E., Qiu, T. and Li, T. (2015). “Simulation of collapse of granular columns using the discrete element method.” *Int J Geomech.* 15(6):04015004.

Lade, P. V., Yamamuro, J.A. and Bopp, P. A. (1996). “Significance of particle crushing in granular materials.” *Journal of Geotechnical Engineering.* 122(4): 309–316.

Li, D.Y., Han, Z.Y., Sun, X.L., Zhou, T. and Li, X.B. “Dynamic mechanical properties and fracturing behavior of marble specimens containing single and double flaws in SHPB tests.” *Rock Mech Rock Eng*. 52(6):1623–1643

Lim, W. L. and McDowell, G. R. (2007). “The importance of coordination number in using agglomerates to simulate crushable particles in the discrete element method.” *Geotechnique*. 57(8): 701–705.

Lobo-Guerrero, S. and Vallejo, L. E. (2005a). “Discrete element method evaluation of granular crushing under direct shear test conditions.” *Journal of Geotechnical and Geoenviron. Eng.* 131: 1295–1300

Lobo-Guerrero, S. and Vallejo, L. E. (2005b). “Crushing of weak granular material: Experimental-numerical analyses.” *Geotechnique*. 553:245–249.

Luo, H., Cooper, W.L. and Lu, H. (2014). “Effects of particle size and moisture on the compressive behavior of dense Eglin sand under confinement at high strain rates.” *Int. J. Impact Eng.* 65: 40–55.

Martin, B.E., Chen, W., Song, B. and Akers, S. A. (2009). “Moisture effects on the high strain-rate behavior of sand.” *Mech Mater*. 41(6): 786-798.

McDowell, G.R., Bolton, M.D and Robertson, D. (1996). “The fractal crushing of granular materials.” *J. Mech. Phys. Solids.* 44(12), 2079–2101.

McDowell, G.R. (2001). “Statistics of soil particle strength.” *Geotechnique.* 51(10): 897-900.

McDowell, G.R. and DeBono, J.P. (2013). “On the micro mechanics of one-dimensional normal compression.” *Géotechnique.* 63(11): 895–908.

McDowell, G. R. (2002). “On the yielding and plastic compression of sand.” *Soils Found.* 42(1): 139–145.

Mun, W. and McCartney, J.S. (2017). “Roles of particle breakage and drainage in the isotropic compression of sand to high pressures.” *Journal of Geotechnical and Geoenvironmental Engineering*. 143: 04017071

Mindlin, R. D. (1949). “Compliance of elastic bodies in contact.” Trans. ASME, Ser. E, J. *Appl. Mech.* 71: 259-268.

Nakata, Y., Kato, Y., Hyodo, M., Hyde, A.F.L. and Murata, H. (2001). “One-dimensional compression behaviour of uniformly graded sand related to single particle crushing strength.” *Soils Found.* 412: 39–51.

Nguyen, H.B.K., Rahman, M.M. and Fourie, A.B. “Characteristic behaviour of drained and undrained triaxial tests: A DEM study.” *Journal of Geotech. Geoenviron. Eng.* 144(9): 04018060.

Omidvar, M., Iskander, M. and Bless, S. (2012). “Stress–strain behavior of sand at high strain rates.” *International Journal of Impact Eng.* 49: 192–213.

Prabhu, S. and Qiu, T (2019). “Effect of particle size on high-strain rate response of sand.” Geocongress Special Publication. 310: 155 – 164.

Prabhu, S. S. and Qiu, T. (2020). “Simulation of split Hopkinson pressure bar tests on sands with low water contents.” *International Journal of Engineering Mechanics*. 146 (8): 04020082

Roessler, T. and Katterfeld, A. (2018). “Scaling of the angle of repose test and its influence on the calibration of DEM parameters using upscaled particles.” *Powder Technology*. 330: 58–66.

Song, B., Chen, W. and Luk, V. (2009). “Impact compressive response of dry sand.” *Mechanics of Materials*. 41(6):777-785.

Teufelsbauer, H., Wang, Y., Chiou, M.C. and Wu, W. (2009). “Flow–obstacle interaction in rapid granular avalanches: DEM simulation and comparison with experiment.” *Granular Matter*. 11(4): 209–220.

Wang, J. and Yan, H. (2013). “On the role of particle breakage in the shear failure behavior of granular soils by DEM.” *International Journal of Numerical and Analytical Methods in Geomechanics*. 37(8): 832–854.

Wang, S., Shen, L., Maggi, F., El-Zein, A., Nguyen, G.D., Zheng, Y., Zhang, H. and Chen, Z. (2018). “Influence of dry density and confinement environment on the high strain rate response of partially saturated sand.” *International Journal of Impact Eng.* 116: 65-78.

Weibull, W. (1951). “A statistical distribution function of wide applicability.” *J. Appl. Mech.* 18: 293–297.

Widulinski, L., Kozicki, J. and Tejchman, J. “Numerical simulations of triaxial test with sand using DEM.” *Archives of Hydroengineering Environmental Mechanics.* 56(3–4): 149–172.

Xiao, Y., Yuan, Z., Chu, J., Liu, H., Huang, J., Luo, S.N., Wang, S. and Lin J. (2019). “Particle breakage and energy dissipation of carbonate sands under quasi-static and dynamic compression.” *Acta Geotechnica.* 14 (6): 1741–1755

Yimsiri, S. and Soga, K. (2010). “DEM analysis of soil fabric effects on behaviour of sand.” *Geotechnique.* 60(6): 483–495.

CHAPTER 6

CONCLUSIONS AND RECCOMENDATIONS

6.1 Conclusions

For most applications, sands in the field are subjected to quasi-static loadings. However, in problems involving blasting, projectile impact etc. sands are subjected to high strain-rate loading. SHPB tests have been extensively used by researchers to study the high strain-rate response of sands. Studies showed that: (1) the addition of water to sand softens the high strain-rate stress-strain response of sand till a transitional water content; (2) particle breakage significantly affects the stress-strain response of sands under quasi-static and high strain-rate loading conditions; and (3) PSD evolution is different under high strain rates compared to quasi-static strain rates. However, none of the models reported in literature could capture the softening-stiffening behavior of sand as a function of water content and the particle breakage under high-strain rate loading conditions.

In Chapter 2, a three-phase continnum model that could effectively capture the sand response at any given water content is calibrated. The calibrated model is validated by comparing the simulated stress-strain response of sand at two different water contents with the experimental results. Parametric studies using the calibrated model showed that the energy absorption initially decreased with an increase in water content till the transitional water content and marginally increased afterwards. It was also observed that specimens with higher aspect ratio attains stress equilibrium and stress uniformity only after

considerable strains have already occurred in the specimen while stress equilibrium is never strictly satisfyed in specimens having interface friction.

In Chapter 3, SHPB tests are simulated using a coupled FEM-DEM analysis. The specimens in the simulations are prepared with a given PSD, upscaled PSD and uniform particle size, to understand the effect of PSD on the stress-strain response at low stresses where particle breakage is insignificant. The study showed that the specimen with the upscaled PSD provided similar response as that obtained for specimen with the original PSD. However, a softer stress-strain response is noted for the specimen prepared with uniform particle size. Therefore, particle size upscaling can be effectively utilized for modeling high strain-rate loadings on sand at low stresses where particle breakage is insignificant. A parametric study using the calibrated model showed that the interface friction provided a slightly stiffer stress-strain response than the lubricated interfaces did.

In Chapter 4, a novel methodology to model SHPB tests on dry sand in DEM is calibrated and validated by comparing the simulated stress-strain response with the experimental response reported in literature. The calibrated DEM model accurately captures the reported stress-strain response of the sand specimen at low stresses where particle breakage is insignificant. The DEM specimen does not attain strict stress equilibrium; however, the stress-strain responses obtained using the transmission bar stress (assuming stress equilibrium) and the average stress between the transmission and incident bars (assuming stress non-equilibrium) are within the error bars reported in the experiment. The parametric study with different rotational resistance shows that a higher particle rotational resistance results in a stiffer stress-strain response. However, particle angularity

in sand does not significantly contribute to the sand response during SHPB tests since particle rotation is not a dominant mode of motion during these tests.

In Chapter 5, a series of SHPB tests reported in the literature are modeled in DEM using different methodologies. The simulated stress-strain responses and evolution of PSD are compared with the reported responses. As particle breakage dominates the stress-strain response at high stresses, particle breakage is introduced in the simulation using a force criterion. Particles satisfying the force criterion are replaced by a set of daughter particles. Using these simulations, the effectiveness of grain size upscaling-downscaling procedure in reducing the computational cost in dynamic problems is discussed. The study showed that with properly calibrated DEM parameters, the simulated high strain-rate stress-strain responses of specimens with the original and upscaled PSDs are generally similar. The stress-strain response at low stresses is governed by the property of the sand particles including the interparticle friction, elastic modulus of the particles and Poison's ratio while the response is dominated by the particle breakage model parameters at higher stresses. The PSD evolutions in the SHPB tests are generally similar for specimens prepared with the original PSD and upscaled PSD after implementing the upscaling-downscaling procedure. The simulated SHPB model could accurately capture the stress propagation in the IB and TB. The modeled stress-strain response is within the error bars reported; hence, the developed DEM model can be used to model the complete SHPB test setup on sand specimens.

6.2 Recommendations for Future Work

6.2.1 Extending three-phase model for usage at high stresses

In this study, a three-phase model is calibrated and validated using the experimental results on quartz sand by Song et al. (2009). The study shows that three-phase model can accurately capture the high strain-rate response of sand at any given water content under low stresses. However, as the model has only been calibrated and validated at low stresses, the model cannot be used for high-stress applications, especially for dry sands. Therefore, there is a need to improve the model such that the improved model can accurately capture the stress-strain responses under a wide range of stresses. The three-phase model is calibrated and validated for sands at a specific porosity (n=0.45). Additional parameters, taking into account the effect of sand porosity on its EOS, need to be incorporated, calibrated and validated in the model using experimental SHPB test results reported in literature.

6.2.2 Improving the coupled FEM-DEM simulations

In the present study, simulations are carried out using a coupled FEM-DEM analysis to understand the effect of PSD upscaling on the stress-strain response of sand at low stresses. However, due to the inability of LS-DYNA to compact the spheres into tighter packing, the simulations are carried out on specimens with higher porosity compared to the specimens used in actual SHPB tests. Therefore, there is a need to improve the model by packing the spheres to higher densities in the coupled FEM-DEM simulations to better

understand the micromechanics and load transfer occurring in the specimen and compare the simulated and experimental responses.

6.2.3 Coupled CFD–DEM to study the effect of water content on high strain-rate sand response

The rapid increase in computational capacities has resulted in tremendous advancements in the field of computational fluid dynamics (CFD). Coupled CFD-DEM simulations can be used to model SHPB tests on sands with different water contents. The simulations can provide further information about the influence of water on the micromechanics of sand. The study can also provide information regarding the volumetric compression of individual phases in sand during high strain-rate tests and can compare these results with those under quasi-static conditions.

6.2.4 Modeling SHPB tests using DEM to understand fracture in concrete and ceramics

Numerous studies have been carried out using SHPB tests to understand the high strain-rate response of various materials including ceramics, metals, alloys etc. Several FEM constitutive models have been developed to capture the response of these materials by modeling them as continuums. However, crack propagation and the imminent material failure, including breakage in brittle materials, for e.g., ceramics, are difficult to be captured in the laboratory and also in FEM. Bonded constitutive models in DEM can effectively capture the breakage in materials like ceramics and concrete. However, the lack

of modeling methodologies to model high strain-rate problems, including SHPB tests, has hindered the usage of DEM to capture material failure. The present study provides a novel methodology to model the SHPB tests in DEM. The parameters of DEM model representing the IB and TB have been calibrated and validated for steel. Similarly, these parameters can be calibrated for aluminum bars and can be used to model high strain-rate problems involving ceramic or concrete breakage to better understand the micromechanics of these materials subjected to high strain rates.

Reference

Song, B., Chen, W. and Luk, V. (2009). "Impact compressive response of dry sand." *Mechanics of Materials*. 41(6):777-785.

VITA

SUDHEER S PRABHU

EDUCATION

Ph.D. in Civil Eng., The Pennsylvania State University, University Park, PA

Master of Technology in Civil Eng., Indian Institute of Technology, Madras, India.

Bachelor of Technology in Civil Eng., National Institute of Technology, Calicut, India.

PROFESSIONAL EXPERIENCE

2016-present	Research / Teaching Assistant The Pennsylvania State University, University Park, PA
05/2019-08/2019	Engineering Intern Geosyntec Consultants, Columbia, MD
2015-2016	Research Assistant Indian Institute of Science, Bangalore, India

SELECTED PUBLICATIONS

1. **Prabhu, S. S.** and Qiu, T. (2020). "Simulation of Split Hopkinson Pressure Bar Tests on Sands with Low Water Contents," *International Journal of Engineering Mechanics*, 146 (8).
2. **Prabhu, S. S.,** Qiu T., Liew, M and Xiao, M. "Evaluation of Aggregate Compaction using Excavator-mounted Hydraulic Plate Compactors." *Journal of Pipeline System Engineering and Practice*, ASCE, 12 (1), 04020054.
3. **Prabhu, S. S.** and Qiu, T. (2019) "Effect of Particle Size on High-Strain Rate Response of Sand." *ASCE Geo-Congress 2019*,GSP 310, 155-164.
4. **Prabhu, S. S.** and Qiu, T. "Simulation of Split Hopkinson Pressure Bar Tests on Dry Sands using the Discrete Element Method". International Journal of Geomechanics, under review.
5. **Prabhu, S. S.** and Qiu, T. "Modeling of Sand Particle Crushing in Split Hopkinson Pressure Bar Tests using the Discrete Element Method". *International Journal of Impact Engineering*, under review.
6. **Prabhu, S. S.,** Te, P., Qiu T., and Evans, J. "Lateral and Torsional Load capacity of Fin Piles." Manuscript under preparation.